The Ph.D. Thesis

Enhancement of energy density of electrochemical capacitors using porous carbon

多孔質炭素を用いた電気化学キャパシタの高エネルギー密度化

Akita University

March, 2022

Takuya EGUCHI

江口　卓弥

Abstract

Electric double layer capacitors (EDLCs) are superior to other energy storage devices in terms of power density and lifetime. Li-ion capacitor (LIC), which combines the anode of Li ion batteries (LIBs) with the cathode of EDLC, is also a promising energy storage device. LICs can achieve higher energy densities than EDLCs, although its cycle performance is lower than EDLCs. There is a need to increase the energy density of these electrochemical capacitors because it has been one-order lower than that of LIBs. Porous carbons have been used as both the electrodes of EDLCs and as the cathode of LICs, and can be fabricated from a variety of organic materials. This thesis targets on the enhancement of energy density of electrochemical capacitors using porous carbons, as well as new anodic active material of LICs. Activated carbons (ACs) are the active material that can be produced from biomass resources, and various attempts have been made to produce ACs derived from biomass resources. However, there are still many biomass resources that have not been utilized. In Chapter 2, the fabrication of AC derived from unused biomass resources as the electrode active material for high energy density EDLC is described. Next, in Chapter 3, the potential of high-performance AC as the electrode active material of EDLC is described. Finally, in Chapter 4, enhancement of energy density of LIC using high-performance AC cathode and Si-based anode is described. Conclusively, ACs derived from organic wastes were shown to be useful as the electrode active materials. It was also exhibited that the particle size of the high specific surface area AC was an important factor affecting the performance of the EDLC, and the high specific surface area AC with optimal particle size for high energy density EDLCs was obtained. A high energy density LIC was realized by matching the operating capacity of the LIC that combines the above high specific surface area AC cathode and Si anode. Owing to the present study, electrochemical capacitors are expected to be used as energy storage devices in various fields because they can overcome the drawback of low energy density. In other words, they can contribute to the development of sustainable society.

概要

電気二重層キャパシタ（EDLC）は、他の蓄電デバイスよりも出力密度や寿命の点で優れている。また、Liイオン電池（LIB）の負極とEDLCの正極を組み合わせたリチウムイオンキャパシタ（LIC）は、有望なエネルギー貯蔵デバイスとして期待されている。LICは、EDLCよりも高いエネルギー密度を実現できるが、サイクル性能はEDLCよりも低い。これら電気化学キャパシタのエネルギー密度は、LIB に比べて一桁低いため、より高いエネルギー密度が求められている。多孔質炭素は、EDLCの電極やLICの正極として用いられており、様々な有機材料から作製することが可能である。本論文では、多孔質炭素を用いた電気化学キャパシタのエネルギー密度の向上と、LICの新しいアノード活物質を対象としている。多孔質炭素である活性炭はバイオマス資源から製造可能な活物質であり、バイオマス資源由来の活性炭の製造は様々な試みがなされている。しかし、まだ利用されていないバイオマス資源が多く存在する。第2章では、高エネルギー密度EDLCのための電極活物質としての未利用バイオマス資源由来活性炭の製造について述べる。次に第3章では，高性能活性炭のEDLCの電極活物質としての可能性について述べる。最後に第4章では、LIC の高エネルギー密度化について述べる。結論として、有機廃棄物由来の多孔質炭素は、電極活物質として有用であることが示された。また，高比表面積活性炭の粒子径がEDLCの性能に影響を与える重要な因子であることが示され，高エネルギー密度EDLCに最適な粒子径の高比表面積活性炭が得られた。その高比表面積活性炭正極とSi負極を組み合わせたLICの動作容量を一致させることで、高エネルギー密度LICを実現した。本研究により、電気化学キャパシタは、エネルギー密度が低いという欠点を克服できるため、様々な分野でのエネルギー貯蔵デバイスとしての利用が期待でき、持続可能な社会の発展に寄与する。

Contents

Introduction

1.1 Background and Objective

Mitigation of carbon dioxide emissions to combat global warming is a global challenge [1]. Energy storage technology has been recognized as one of the effective means to reduce carbon dioxide emissions. Supercapacitors are attracting much attention as promising energy storage devices because of their high power density, long cycle-life, fast charge-discharge and lower maintenance cost when compared to secondary batteries such as lead-acid and lithium ion batteries (LIBs). Despite the critical drawback of their low energy density, supercapacitors have been selected as a robust option for a diverse range of energy storage sectors (e.g., energy recovery through braking in the automobile industry, large-scale uninterrupted power supply, and power sources for industrial machines) [2]. Supercapacitors can be categorized into two main groups: electric double-layer capacitors (EDLCs) based on non-faradaic reactions, and pseudocapacitors based on faradaic reactions [3]. Pseudocapacitors employ metal oxides (e.g., NiO) [4] or conducting polymers (e.g., poly 3, 4-ethylenedioxythiophene) [5] as electrode active materials because of their high specific capacitance; however, these electrode active materials are more expensive than carbon materials which have been widely used in EDLCs [3]. Carbonaceous materials, including activated carbon (AC), carbon nanofibers, graphene nanosheets, and carbon nanotubes, are commonly used in the electrodes of EDLCs [6]. Although carbonaceous materials exhibit lower specific capacitances than the active materials of pseudocapacitors, they have some beneficial features, including high conductivity, high chemical stability, and low cost. Among carbonaceous materials, ACs are currently a main source of active materials of EDLC electrodes, mainly owing to their large-scale productivity and excellent cost-performance. LIBs and EDLCs have recently entered mainstream automotive and stationary electricity storage applications [7]. Conventional LIBs employing $LiCoO_2$ cathodes and graphite anodes can deliver high energy densities of ~220 Wh kg_{FC}^{-1}, based on the mass of the full-cell (FC) state [8, 9]. Contemporary LIBs using ternary-lithiated transition-metal-oxide anodes, such as $LiNi_xCo_yMn_{(1-x-y)}O_2$ and $LiNi_xCo_yAl_{(1-x-y)}O_2$, and graphite anodes can attain energy densities

up to 300 Wh kg_{FC}^{-1} [9, 10]. However, the power densities and cycle lives of LIBs remain limited to < 1 kW kg_{FC}^{-1} and ~1000, respectively [11]. In contrast, the charge/discharge mechanism of EDLCs is attributed to non-Faradaic physical adsorption/desorption of electrolytic ions on the cathode and anode surfaces to form electric double layers. Wider double-layers increase the storage capacity. Therefore, ACs having specific surface areas exceeding 1000 $m^2\ g^{-1}$ are preferred as the active material in EDLC electrodes [12]. Eschewing Faradaic (or redox) reactions for the charge/discharge processes, EDLCs deliver higher power densities (> 5 kW kg_{FC}^{-1}) and longer cycle lives (> 100000) than LIBs. However, the energy density of EDLCs remains low (< 10 Wh kg_{FC}^{-1}) because of the limited density of charges on the electrode surfaces [13].

Li-ion capacitors (LICs) are categorized as hybrid capacitors that accept non-Faradaic processes, which generate the electric double layer on the cathode, and Faradaic reactions, through which Li-ion insertion/extraction occurs at the anode [14]. The active material of LIC cathodes requires a high specific surface area to form a wide electric double-layer. Therefore, ACs have been widely used in LIC cathodes. Carbonaceous materials such as graphite, hard carbon, and soft carbon have been employed as active materials for LIC anodes [15-18]. Graphite is the most widely used carbonaceous anode active material. The theoretical Li-ion insertion capacity of graphite is 372 mAh g^{-1}, and its discharge plateau has the lowest known value of ~0.1 V vs. Li/Li^+ [19]. $Li_4Ti_5O_{12}$ (LTO) is used as an active material for LIC anodes because it exhibits high cycling stability [20-22]. The discharge plateau of LTO is 1.55 V vs. Li/Li^+, and it possesses a theoretical Li-ion insertion capacity of 175 mAh g^{-1} [23]. LICs combine the advantages of EDLCs and LIBs; consequently, they exhibit energy densities of ~30 Wh kg^{-1}-AC and sustainable power densities of ~10 kW kg_{FC}^{-1}-AC. These numbers lie in between the performances of EDLCs and LIBs [24].

Various biowaste-derived ACs have been applied as electrode active materials of EDLCs to enhance the utilization of bioresources [25]. Leather [26], winery waste [27], pollen grains [28], Aloe vera [29], silkworm cocoon [30], bamboo [31], ginkgo leaves [32], coffee grounds [33], kapok fibers [34], pomelo peels [35], tobacco rods [36], rice husks [37], and hemp stems [38] have been utilized as the source materials of ACs intended for EDLC applications.

Higher specific surface area is generally required for the ACs to produce a wider double-layer, thereby attaining a higher specific capacitance. Chemical activation using KOH is frequently used to obtain highly porous ACs, generating specific surface areas in the range of ~3000 m^2 g^{-1} [34]. Those provided a very high gravimetric specific capacitance of 209–575 F g^{-1} under the use of aqueous electrolytes [39-41] and that of 144–338 F g^{-1} under the use of nonaqueous electrolytes [34, 42, 43]. Textural properties of ACs, such as average pore size, pore geometry, and pore-size distribution, have a large influence on the formation and release of an electric double-layer at the interface between the AC and the electrolyte [44]. Microporous ACs with a narrow width of <2 nm can produce a wide electric double-layer and thus give the electrode a high specific capacitance [45-48].

The type of electrolyte is also important in relation to the formation of the electric double-layer and its release on the electrode surface [49]. EDLC electrolytes can be divided into three groups: aqueous electrolytes, non-aqueous electrolytes, and ionic liquids. Aqueous electrolytes are inexpensive but inferior in terms of energy density owing to their narrow potential windows (maximum 1.23 V). Ionic liquids can provide EDLC cells with a higher cell voltage (up to ~4 V) because of their wide potential window [50]. However, they have several disadvantages, including high cost and poor low-temperature performance resulting from their high viscosity. Non-aqueous electrolytes are now chiefly used in commercial EDLCs owing to their well-balanced performance and high cost-effectiveness [6]. The energy stored in EDLC cells is expressed by $\frac{1}{2}CV^2$, where C is the cell capacitance and V is the cell voltage, indicating that cell voltage enhancement is primarily responsible for greater energy storage. The maximum cell voltage of EDLCs using non-aqueous electrolytes is generally 2.5 V. The maximum cell voltage can be increased to 2.7 V [51] and further to 3.0 V [35] to enhance the energy storage of EDLC cell instead of lifetime shortening. ACs exposed to non-aqueous electrolytes also need to have sufficient electrochemical stability to withstand the maximum working cell voltage.

There is a need to increase the energy density of these electrochemical capacitors because it has been one-order lower than that of LIBs. Porous carbons having very high specific surface area have been used as both the electrodes of EDLCs and as the cathode of LICs so as to produce wider electric double-layer and thereby to increase the gravimetric and volumetric

charge-storage density. This thesis targets on the enhancement of energy density of electrochemical capacitors using porous carbons, as well as new anodic active material of LICs. ACs are the active material that can be produced from biomass resources, and various attempts have been made to produce AC derived from biomass resources. However, there are still many biomass resources that have not been utilized. In Chapter 2, the fabrication of AC derived from unused biomass resources as the electrode active material for high-energy density EDLC was described. Shochu is a major distilled liquor in Japan, and significant shochu waste (approximately one million metric tons) is discharged every year. Wheat shochu waste was precarbonized at 600 or 700 ℃ and then processed by KOH chemical activation, producing shochu waste-derived activated carbon (SWAC). The material properties and electrochemical performance of SWAC were investigated to verify its potential use as the electrode active material of EDLCs, in comparison with two types of commercially available benchmark activated carbons. Next, in Chapter 3, the potential of high-performance AC as the electrode active material of EDLC was described. AC with a very high specific surface area of >3000 m^2 g^{-1} and a number of course particles was pulverized by means of planetary ball milling under different conditions to find its greatest performances as the active material of EDLC using a nonaqueous electrolyte. The variations in textural properties and particle morphology of the AC during the ball milling were investigated. The electrochemical performance was also evaluated for the ACs milled with different particle size distributions. Finally, in Chapter 4, the high energy density LIC using high-performance AC is described. A very high energy density LIC was developed using commercially available AC having a high surface area of 3041 m^2 g^{-1} and conventional 2 μm-sized Si as the cathode and anode material, respectively, by minimizing the unused capacity of the anode.

1.2 EDLC and LIC charging and discharging mechanism [2,12,19,52-55]

1.2.1 Basic principles of EDLC

Figure 1.1 shows the behavior of ions in the cell during charging and discharging of EDLCs. Based on the Helmholts model, the behaver of ions in the electrolyte is explained as

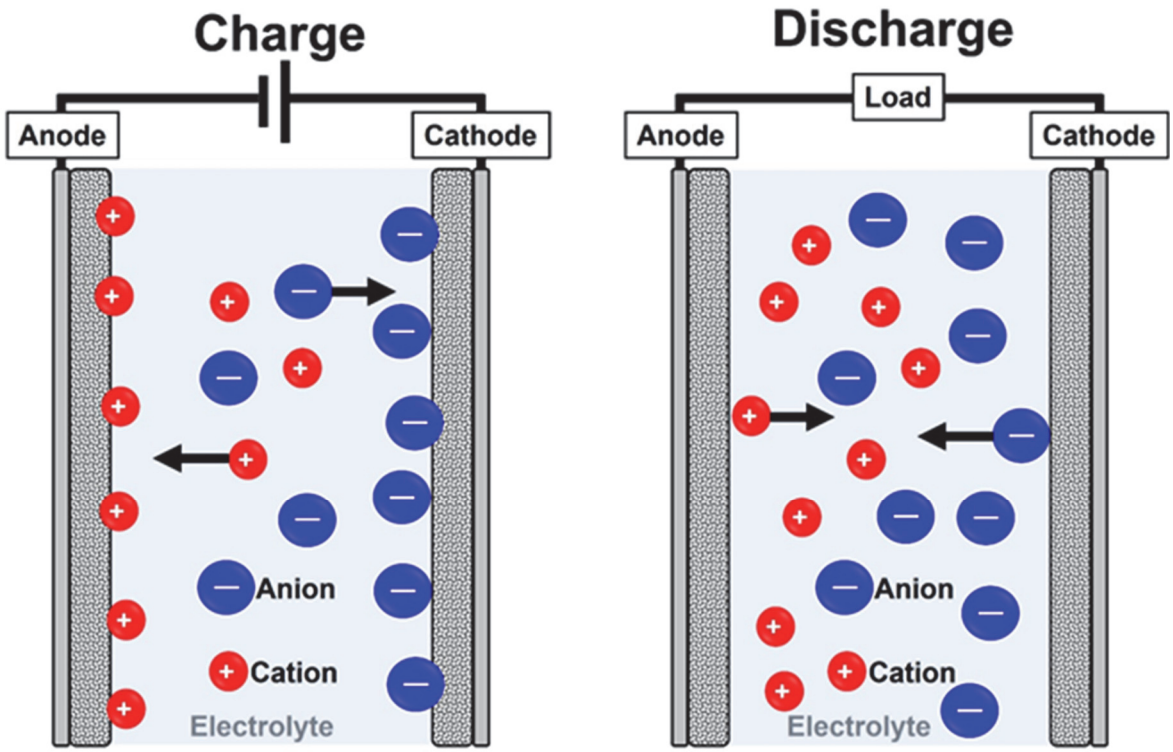

Fig. 1.1. Behavior of ions in the cell during charging and discharging of EDLC

follows: During charging, an electric double-layer is formed at the electrode//electrolyte interface. At the interface on the cathode side, a layer with electrons is formed on the electrode side and a monolayer of cations is formed on the electrolyte side. On the anode side, two layers similar to the cathode side are formed at the electrode/electrolyte interface by anions and holes. During discharge, ions are released from the layer formed at the electrode/electrolyte interface. The capacitance C_H of electric double-layer formed on one of the electrodes is expressed by the following equation (1.1);

$$C_H = \frac{\varepsilon_0 \varepsilon_r S}{d} \tag{1.1}$$

where S is the surface area with electrode//electrolyte interface, ε_0 is vacuum permittivity, ε_r is the relative permittivity of electrolyte, and d is the charge separation distance. In EDLC, since porous materials are used for the electrode, the electric double-layer is formed in the closed region within porous materials. Therefore, EDLCs can provide much larger capacitance than that of the parallel plate type. To obtain the high capacitance, the large surface area is necessary, but the structure of pores is also important. The pores in materials is distinguished into

micropore (pore width $D < 2$ nm), mesopore (D 2-50 nm), and micropore (D >50 nm). The size of pores affects the capacitance, and materials with more micropores tend to have higher capacitance because the solvated ions are partially desorbed in the pores.

The electric potential of the entire EDLC cell is shown in **Fig. 1.2** (state of charge). In the anode side, the potential is lower due to the formation of electric double-layer by the cations. Conversely, at the cathode, the potential is higher due to the formation of electric double-layer by the anions. Here, the potential difference between the cathode and anode is the cell voltage, which can be expressed by the two capacitors in series. The electrical characteristics of EDLCs during charging and discharging are similar to those of a capacitor. The electrical behavior of the EDLC during charging and discharging is shown in **Fig. 1.3**. Since the cell voltage is governed only by the adsorption and desorption of ions in the electrolyte at the electrodes, it increases linearly with charging time, and conversely, it decreases linearly with discharging. Therefore, the ideal charge/discharge shape of EDLC is the triangle. During charging, ions are adsorbed onto the cathode and anode sides, and during discharging, ions are desorbed from them. Because the charging/discharging mechanism of EDLC is based on the physical adsorption/desorption of ions, it has superior performance in terms of lifetime and power density compared to energy storage devices utilizing chemical reactions. The maximum cell voltage is related to the decomposition voltage of the electrolyte, which is 2.5 to 2.7 V for organic electrolytes. The potential variations of the cathode and anode during charging and discharging is shown in **Fig. 1.3**. The change in potential of the ideal cathode and anode is represented by a rhombus shape, which is a combination of a triangle and an inverted triangle, for the reasons described above. Based on the charge-discharge test results, the capacity of EDLCs can be measured and their energy density can be calculated. The greater the magnitude of the charge/discharge cell voltage, the higher the energy density of EDLC.

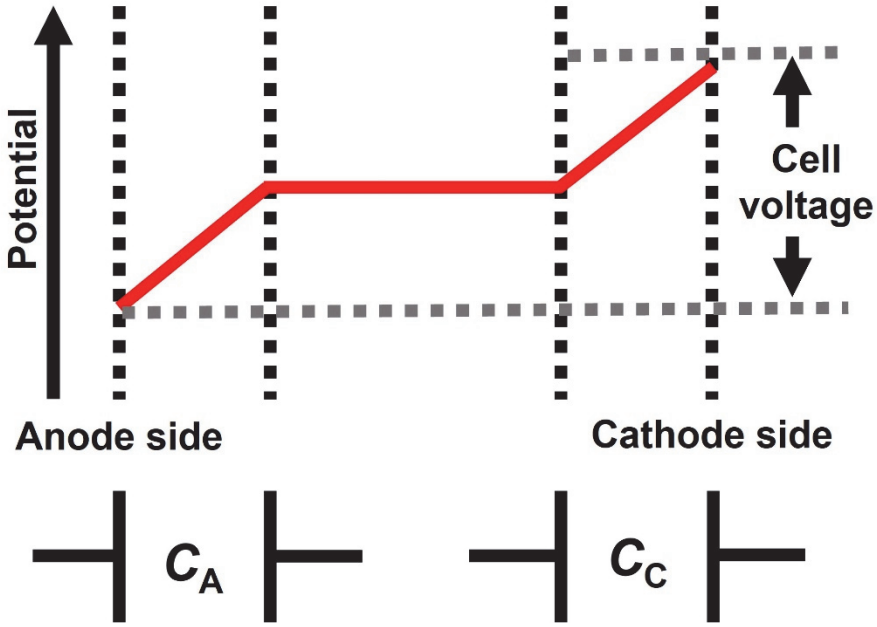

Fig. 1.2. Potential variation in the entire EDLC cell.

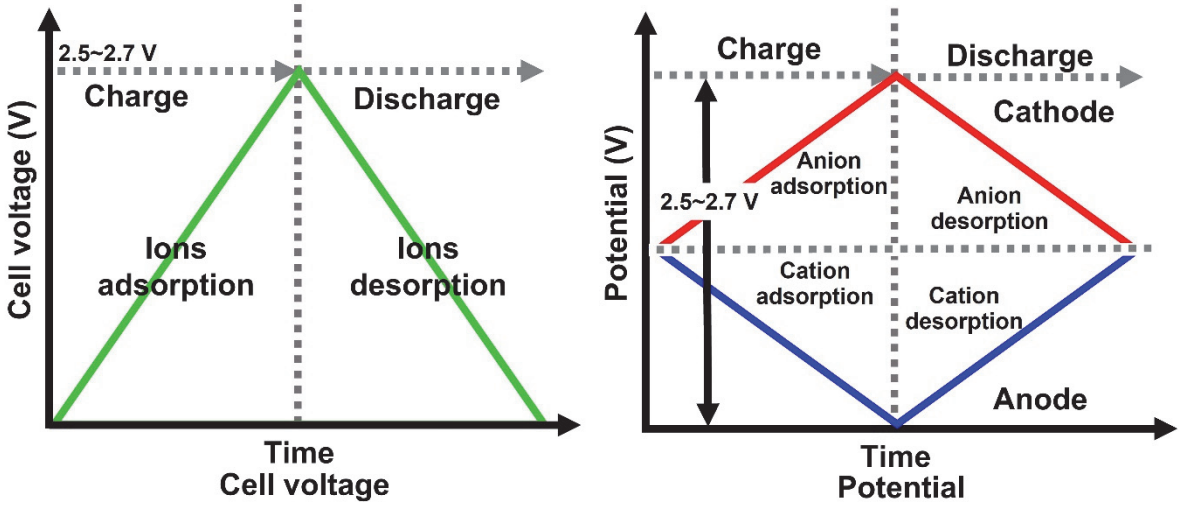

Fig. 1.3. Electrochemical behavior of symmetric EDLC during charging and discharging.

1.2.2 Basic principles of LIC

As mentioned above, the LIC is hybrid capacitors that uses EDLC-type electrodes as the cathode and battery-type electrodes as the anode. LICs operate at the wider range of cell voltages than do EDLCs by lowering the potential of the anode, achieving the higher energy density. **Figure 1.4** shows the simple behavior of ions in the cell during charging and

discharging of LIC. On the anode side during charging and discharging, Li-ions are inserted and extracted into the anode active material. The reaction process at its normal anode with the charge-discharge is shown in equation 1.2,

$$\mathrm{Li^+} + xe^- + \mathrm{M} \quad \underset{\text{discharge}}{\overset{\text{charge}}{\rightleftarrows}} \quad \mathrm{Li}_x\mathrm{M} \tag{1.2}$$

where M is the anode active material. When the anode active material is sufficiently intercalated or alloyed with Li-ions, the anode potential approaches to the potential of Li metal. The closer the potential of Li_xM intercalated or alloyed with Li-ions is to the potential of the Li metal, the wider the operating voltage of the LIC can be. Hereafter, the potential of Li metal is determined to be a reference value, and the potential against the Li metal potential is expressed in a unit of V vs. Li/Li^+. The potential of many Li-intercalated or Li-alloyed materials is ~0.3 to ~1.5 V vs. Li/Li^+. The potential of the non-lithiated cathode is usually 3 V vs. Li/Li^+ relative to the lithiated anode. The porous carbon material also takes 3 V vs. Li/Li^+ potential against the lithiated anode. Therefore, for the porous carbon material of the LIC cathode side, the ion species adsorbed and desorbed are different at the boundary of 3 V vs. Li/Li^+. The ion adsorption/desorption phenomenon on the cathode side above 3V is expressed by equation 1.3, and below 3V by equation 1.4.

$$\mathrm{AC} + \mathrm{PF_6^-} \quad \underset{\text{desorption}}{\overset{\text{adsorption (charge)}}{\rightleftarrows}} \quad \mathrm{AC//PF_6^-(electric\ \ double-layer)} \tag{1.3}$$

$$\mathrm{AC//Li^+(electric\ \ double-layer)} \quad \underset{\text{adsorption}}{\overset{\text{desorption (charge)}}{\rightleftarrows}} \quad \mathrm{AC} + \mathrm{Li^+} \tag{1.4}$$

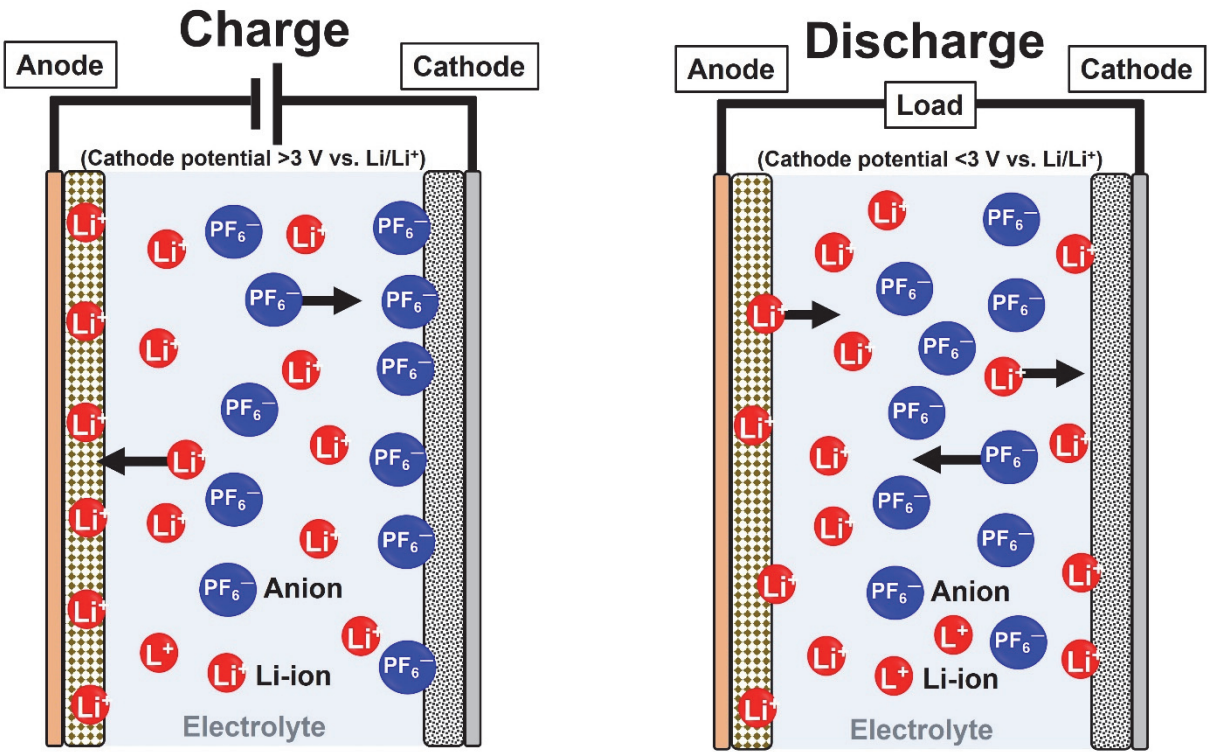

Fig. 1.4. Behavior of ions in the cell during charging and discharging of LIC.

The electrochemical behavior of the LIC during charging and discharging is shown in **Fig. 1.5**. The upper and lower cell voltages are usually set to be 3.0-4.5 V and 1.0-2.0 V, respectively, because they are related to the electrochemical properties of the lithiated active material of anode and the durability of used electrolyte against the oxidative decomposition. Since the potential difference between the cathode and anode appears in the cell voltage, the charging and discharging shape of the cell voltage is almost similar to that EDLCs. Ideally, the anode potential should remain to be 0 V vs. Li/Li^+, but in many anode active materials, the potential increases with the extraction of Li-ions. Therefore, for the high energy density LICs, active materials which can abundantly accept Li-ions are required to ensure lower and flatter potential profile. The energy storage mechanism of the LIC cathode is ion absorption and desorption on its surface, the cathode active material with the high Li-ion specific capacity is required to achieve high energy density.

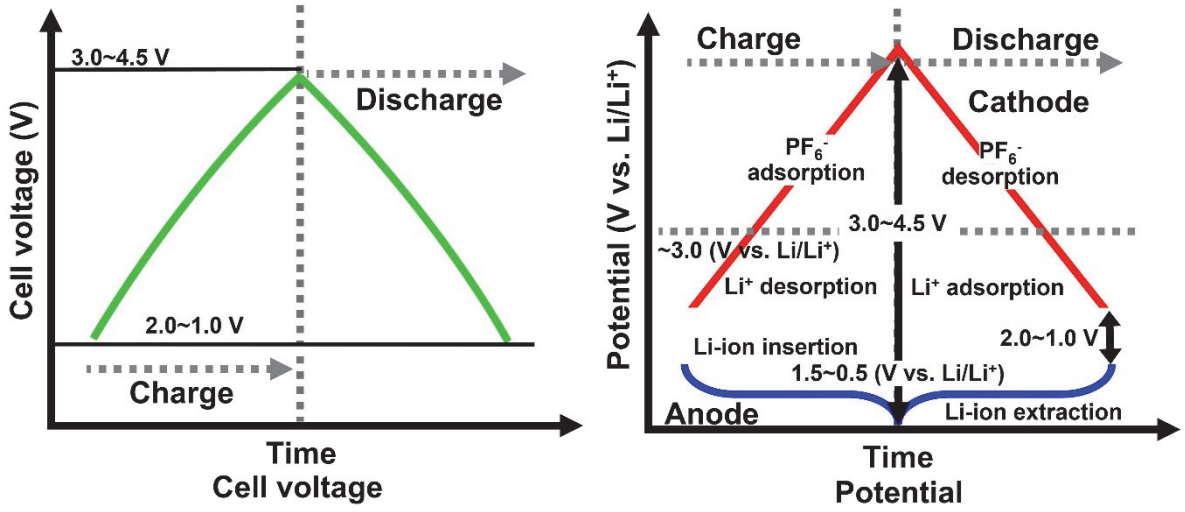

Fig. 1.5. Electrochemical behavior of the LIC during charging and discharging.

Reference

[1] M. Ma, X. Ma, W. Cai, Carbon-dioxide mitigation in the residential building sector: a household scale-based assessment. J. Energy Convers. Manag. 198 (2019) 111915.

[2] A. Muzaffar, M.B. Ahamed, K. Deshmukh, J. Thirumalai, A review on recent advances in hybrid supercapacitors: design, fabrication and applications. Renew. Sustain. Energy Rev. 101 (2019) 123−145.

[3] L. Wei, G. Yushin, Nanostructured activated carbons from natural precursors for electrical double layer capacitors. Nano Energy 1 (2012) 552−565.

[4] K.S. Lee, M.S. Park, J. Kim, Nitrogen doped activated carbon with nickel oxide for high specific capacitance as supercapacitor electrodes. Colloids Surf., A 533 (2017) 323−329.

[5] M. Rajesh, C.J. Raj, R. Manikandan, B.C. Kim, S.Y. Park, K.H. Yu, A high performance PEDOT/PEDOT symmetric supercapacitor by facile in-situ hydrothermal polymerization of PEDOT nanostructures on flexible carbon fibre cloth electrodes. Mater. Today Energy 6 (2017) 96−104.

[6] W. Raza, F. Ali, N. Raza, Y. Luo, K. Kim, J. Yang, S. Kumar, A. Mehmood, E.E. Kwon, Recent advancements in supercapacitor technology. Nano Energy 52 (2018) 441−473.

[7] S. Koohi-Fayegh, M.A. Rosen, A review of energy storage types, applications and recent developments, J. Energy Storage 27 (2020) 101047.

[8] W. Xue, L. Miao, L. Qie, C. Wang, S. Li, J. Wang, J. Li, Gravimetric and volumetric energy densities of lithium-sulfur batteries, Curr. Opin. Electrochem. 6 (2017) 92–99.

[9] W. Cao, J. Zhang, H. Li, Batteries with high theoretical energy densities, Energy Storage Mater. 26 (2020) 46–55.

[10] Y. Lu, X. Rong, Y.S. Hu, L. Chen, H. Li, Research and development of advanced battery materials in China, Energy Storage Mater. 23 (2019) 144–153.

[11] K. Zou, P. Cai, X. Cao, G. Zou, H. Hou, X. Ji, Carbon materials for high- performance lithium-ion capacitor, Curr. Opin. Electrochem. 21 (2020) 31–39.

[12] A. Jagadale, X. Zhou, R. Xiong, D.P. Dubal, J. Xu, S. Yang, Lithium ion capacitors (LICs): Development of the materials, Energy Storage Mater. 19 (2019) 314–329.

[13] P. Han, G. Xu, X. Han, J. Zhao, X. Zhou, G. Cui, Lithium ion capacitors in organic electrolyte system: Scientific problems, material development, and key tech- nologies, Adv. Energy Mater. 8 (2018) 1801243.

[14] S. Kumagai, Y. Abe, T. Saito, T. Eguchi, M. Tomioka, M. Kabir, D. Tashima, Lithium-ion capacitor using rice husk-derived cathode and anode active ma- terials adapted to uncontrolled full-pre-lithiation, J. Power Sources 437 (2019) 226924.

[15] T. Rauhala, J. Leis, T. Kallio, K. Vuorilehto, Lithium-ion capacitors using carbide-derived carbon as the positive electrode –a comparison of cells with graphite and $Li_4Ti_5O_{12}$ as the negative electrode, J. Power Sources 331 (2016) 156–166.

[16] S.R. Sivakkumar, J.Y. Nerkar, A.G. Pandolfo, Rate capability of graphite materials as

negative electrodes in lithium-ion capacitors, Electrochim. Acta 55 (2010) 3330–3335.

[17] X. Sun, X. Zhang, W. Liu, K. Wang, C. Li, Z. Li, Y. Ma, Electrochemical perfor- mances and capacity fading behaviors of activated carbon/hard carbon lithium ion capacitor, Electrochim. Acta 235 (2017) 158–166.

[18] M. Schroeder, M. Winter, S. Passerini, A. Balducci, On the cycling stability of lithium-ion capacitors containing soft carbon as anodic material, J. Power Sources 238 (2013) 388–394.

[19] M. Winter , J.O. Besenhard , M.E. Spahr , P. Novák , Insertion electrode materials for rechargeable lithium batteries, Adv. Mater. 10 (1998) 725–763.

[20] C. Lu, X. Wang, X. Zhang, H. Peng, Y. Zhang, G. Wang, Z. Wang, G. Cao, N. Umirov, Z. Bakenov, Effect of graphene nanosheets on electrochemical per-formance of $Li_4Ti_5O_{12}$ in lithium-ion capacitors, Ceram. Int. 43 (2017) 6554–6562.

[21] M. Uceda, H.C. Chiu, R. Gauvin, K. Zaghib, G.P. Demopoulos, Electrophoretically co-deposited $Li_4Ti_5O_{12}$/reduced graphene oxide nano-layered composites for high-performance battery application, Energy Storage Mater. 26 (2020) 560–569.

[22] C. Liu, S. Wang, C. Zhang, H. Fu, X. Nan, Y. Yang, G. Cao, High power high safety battery with electrospun $Li_3V_2(PO_4)_3$ cathode and $Li_4Ti_5O_{12}$ anode with 95% energy efficiency, Energy Storage Mater. 5 (2016) 93–102.

[23] K. Naoi, S. Ishimoto, Y. Isobe, S. Aoyagi, High-rate nano-crystalline $Li_4Ti_5O_{12}$ attached on carbon nano-fibers for hybrid super capacitors, J. Power Sources 195 (2010) 6250–6254.

[24] S.H. Lee, C. Huang, P.S. Grant, High energy lithium ion capacitors using hybrid cathodes comprising electrical double layer and intercalation host multi-layers, Energy Storage Mater. 33 (2020) 408–415.

[25] R.T. Ayinla, J.O. Dennis, H.M. Zaid, Y.K. Sanusi, F. Usman, L.L. Adebayo, A review of technical advances of recent palm bio-waste conversion to activated carbon for energy storage. J. Clean. Prod. 229 (2019) 1427–1442.

[26] L.J. Kennedy, T. Ratnaji, N. Konikkara, J.J. Vijaya, Value added porous carbon from leather wastes as potential supercapacitor electrode using neutral electrolyte. J. Clean. Prod. 197 (2018) 930–936.

[27] L. Guardia, L. Suárez, N. Querejeta, C. Pevida, T.A. Centeno, Winery wastes as precursors of sustainable porous carbons for environmental applications. J. Clean. Prod. 193 (2018) 614–624.

[28] L. Wei, K. Tian, X. Zhang, Y. Jin, T. Shi, X. Guo, 3D porous hierarchical microspheres of activated carbon from nature through nanotechnology for electrochemical double-layer capacitors. Sustain. Chem. Eng. 4 (2016) 6463–6472.

[29] M. Karnan, K. Subramani, N. Sudhan, N. Ilayaraja, M. Sathish, Aloe vera derived activated high-surface-area carbon for flexible and high-energy supercapacitors. Appl. Mater. Interfaces 8 (2016) 35191–35202.

[30] J. Sun, J. Niu, M. Liu, J. Ji, M. Dou, F. Wang, Biomass-derived nitrogendoped porous carbons with tailored hierarchical porosity and high specific surface area for high energy and power density supercapacitors. Appl. Surf. Sci. 427 (2018) 807–813.

[31] G. Zhang, Y. Chen, Y. Chen, H. Guo, Activated biomass carbon made from bamboo as electrode material for supercapacitors. Mater. Res. Bull. 102 (2018) 391–398.

[32] X. Zhu, S. Yu, K. Xu, Y. Zhang, L. Zhang, G. Lou, Y. Wu, E. Zhu, H. Chen, Z. Shen, B. Bao, S. Fu, Sustainable activated carbons from dead ginkgo leaves for supercapacitor electrode active materials. Chem. Eng. Sci. 181 (2018) 36–45.

[33] D. Tashima, Y. Hamasuna, D. Mishima, S. Kumagai, J.D.W. Madden, Microporous activated carbons from used coffee grounds for application to electric double layer capacitors. IEEJ Trans. Electr. Electron. Eng. 9 (2014) 343–350.

[34] Z. Zou, T. Liu, C. Jiang, Highly mesoporous carbon flakes derived from a tubular biomass for high power electrochemical energy storage in organic electrolyte. Mater. Chem. Phys. 223 (2019) 16–23.

[35] F. Sun, L. Wang, Y. Peng, J. Gao, X. Pi, Z. Qu, G. Zhao, Y. Qin, Converting biomass waste into microporous carbon with simultaneously high surface area and carbon purity as advanced electrochemical energy storage materials. Appl. Surf. Sci. 436 (2018) 486–494.

[36] Y.Q. Zhao, M. Lu, P. Tao, Y. Zhang, X. Gong, Z. Yang, G. Zhang, H. Li, Hierarchically porous and heteroatom doped carbon derived from tobacco rods for supercapacitors. J. Power Sources 307 (2016) 391–400.

[37] S. Kumagai, D. Tashima, Electrochemical performance of activated carbons prepared from rice husk in different types of non-aqueous electrolytes. Biomass Bioenergy 83 (2015) 216–223.

[38] W. Sun, S.M. Lipka, C. Swartz, D. Williams, F. Yang, Hemp-derived activated carbons for supercapacitors. Carbon 103 (2016) 181–192.

[39] G. Huang, Y. Wang, T. Zhang, X. Wu, J. Cai, High-performance hierarchical N doped porous carbons from hydrothermally carbonized bamboo shoot shells for symmetric supercapacitors. J. Taiwan Inst. Chem. Eng. 96 (2019) 672–680.

[40] L. Peng, Y. Liang, H. Dong, H. Hu, X. Zhao, Y. Cai, Y. Xiao, Y. Liu, M. Zheng, Super-hierarchical porous carbons derived from mixed biomass wastes by a stepwise removal strategy for high-performance supercapacitors. J. Power Sources 377 (2018) 151–160.

[41] D. Pontiroli, S. Scaravonati, G. Magnani, L. Fornasini, D. Bersani, G. Bertoni, C. Milanese, A. Girella, F. Ridi, R. Verucchi, et al. Super-activated biochar from poultry litter for high-performance supercapacitors. Microporous Mesoporous Mater. 285 (2019) 161–169.

[42] T. Mori, S. Iwamura, I. Ogino, S.R. Mukai, Cost-effective synthesis of activated carbons with high surface areas for electrodes of non-aqueous electric double layer capacitors. Sep. Purif. Technol. 214 (2019) 174–180.

[43] Y. Gao, L. Li, Y. Jin, Y. Wang, C. Yuan, Y. Wei, G. Chen, J. Ge, H. Lu, Porous carbon made from rice husk as electrode material for electrochemical double layer capacitor. Appl. Energy 153 (2015) 41–47.

[44] D.T.L. Galhena, B.C. Bayer, S. Hofmann, G.A,J. Amaratunga, Understanding capacitance variation in subnanometer pores by in situ tuning of interlayer constrictions. Nano 10 (2016) 747–754.

[45] E. Raymundo-Pinero, K. Kierzek, J. Machnikowski, F. Béguin, Relationship between the nanoporous texture of activated carbons and their capacitance properties in different electrolytes. Carbon 44 (2006) 2498–2507.

[46] I. Yang, S.G. Kim, S.H. Kwon, M.S. Kim, J.C. Jung, Relationships between pore size and charge transfer resistance of carbon aerogels for organic electric double-layer capacitor electrodes. Electrochim. Acta 223 (2017) 21–30.

[47] X.L. Dong, A.H. Lu, W.C. Li, Highly microporous carbons derived from a complex of glutamic acid and zinc chloride for use in supercapacitors. J. Power Sources 327 (2016) 535–542.

[48] J. Chmiola, G. Yushin, Y. Gogotsi, C. Portet, P. Simon, P.L. Taberna, Anomalous increase in carbon capacitance at pore sizes less than 1 nanometer. Science 313 (2006) 1760–1763.

[49] E. Redondo, J. Segalini, J. Carretero-Gonzalez, E. Goikolea, R. Mysyk, Relation between texture and high-rate capacitance of oppositely charged microporous carbons from biomass waste in acetonitrile-based supercapacitors. Electrochim. Acta 293 (2019) 496–503.

[50] C. Liu, Y. Liu, T. Yi, C. Hu, Carbon materials for high-voltage supercapacitors. Carbon 145 (2019) 529–548.

[51] X. Lin, H. Lou, W. Lu, F. Xu, R. Fu, D. Wu, High-performance organic electrolyte supercapacitors based on intrinsically powdery carbon aerogels. Chin. Chem. Lett. 29 (2018) 633–636.

[52] J.J. Lamb, O. S. Burheim, Lithium-Ion Capacitors: A Review of Design and Active Materials. Energies 14 (2021) 979.

[53] L. Jin, X. Guo, C. Shen, N. Qin, J. Zheng, Q. Wu, C. Zhang, J. P. Zheng, A universal matching approach for high power-density and high cycling-stability lithium ion capacitor. J. Power Sources 441 (2019) 227211.

[54] P. Ratajczak, M. E. Suss, F. Kaasik, F. Bèguin, Carbon electrodes for capacitive technologies. Energy Storage Materials 16 (2019) 126-145.

[55] F. Holtstiege, P. Bärmann, R. Nölle, M. Winter, T. Placke, Pre-Lithiation Strategies for Rechargeable Energy Storage Technologies: Concepts, Promises and Challenges. Batteries 4 (2018) 4.

Application of organic waste to porous carbon for electrode active materials of EDLCs

2.1 Introduction

Various alcoholic beverages produced by fermenting grains and other plant organs are available in the Japanese market. Shochu is a major distilled liquor in Japan, utilizing several types of plant organs, (e.g., wheat, potato, rice). Japanese shochu production annually produces approximately one million metric tons of marc, also called shochu waste (SW) [1]. The effective utilization of SW has garnered increasing attention. SW is generally produced as a slurry during shochu production. Because the supernatant of SW slurry contains organic matter such as proteins and amino acids [2], it has been applied as a feedstuff or as a fertilizer. Abundant microorganisms are also contained in SW slurry. Therefore, SW has been utilized for methane gas generation [3] and microbial fuel cells [4]. However, because the cost-effectiveness of these applications is much lower than those of existing methods or technologies, their rate of utilization is not high [5]. Very few studies have focused on utilization of the solid components of SW slurry, primarily comprising grain residues. Highly functional and cost-effective materials converted from SW solid components are now emerging, which could enhance SW utilization.

Biowaste-derived ACs produced by KOH activation have been a recent focus of research because they exhibit significant potential for enhanced EDLC-related performance. The process of chemical activation using KOH generally involves the following steps: precarbonization of the source material, impregnation of KOH into the precursor carbon, heat treatment under inert conditions at a constant temperature exceeding the precarbonization temperature, and final washing for neutralization. A high surface area AC was readily produced from multiple biowastes by means of KOH activation: 2167 m^2 g^{-1} for pomelo peels [6], 2864 m^2 g^{-1} for lotus seedpods [7], and 3263 m^2 g^{-1} for rice husk [8]. The influence of KOH impregnation content, activation temperature, and activation time on the textural properties of ACs has been intensively studied [9]. Such studies have demonstrated that the KOH impregnation content and activation temperature greatly affect the textural properties of AC.

The mass of KOH impregnated into the precursor carbon is two to five times the mass of the precursor carbon. The amount of KOH sufficient to produce a specific surface area of >2500 m^2 g^{-1} was reported to be more than twice the mass of the precursor carbon [10]. In terms of economics and productivity, the impregnation of smaller amounts of KOH into the precursor carbon is desirable. The textural properties of KOH-based ACs are known to be influenced by the precarbonization temperature of the source materials [11]. It was reported that, for the fabrication of polyaniline-based ACs by means of KOH activation, higher specific surface area was obtainable from low precarbonization temperatures (400–650 ℃) than from a high precarbonization temperature of 800 ℃ [12]. Few studies have reported on producing and characterizing SWACs derived from the solid components of wheat-based SW. Hence, the aim of the present study is to establish a new SW utilization method which is socially acceptable, cost-effective, and technologically advanced. We attempted to convert wheat-based SW into high-performance AC intended as the active material of an EDLC electrode by means of KOH activation. SWACs were prepared using different precarbonization temperatures to seek better energy storage and release characteristics in EDLC cells. Specific capacitance, rate and cyclic stability, and Ragone plots of the SWACs were evaluated in comparison with those of commercially available benchmark ACs under normal (maximum 2.5 V) and extended (maximum 3.0 V) cell voltage ranges. In addition to carrying out material characterizations of precarbonized SWs and SWACs, we verified the potential of SWACs as the active material of EDLC electrodes, which is the specific aim of this research.

2.2 Materials and methods

2.2.1 Preparation of ACs

Wheat-based SW was provided in a marc state by the Japanese Shochu Company in Kyushu district of Japan. The SW was separated into solid and liquid phases by a centrifuge. The solid-state SW was dried at 70 ℃ for >24 h and used as the source material for ACs. The preparation procedure of the dried SW is shown in **Fig. 2.1**. The dried SW was precarbonized in a tube furnace (ARF-50KC, Asahi Rika Factory Co., Ltd., Japan) under a N_2 gas flow (600 mL min^{-1}). It was heated to the precarbonization temperature (600 or 700 ℃) at a heating rate

of 5 ℃ min^{-1}. The final temperature was maintained for 1 h, followed by cooling to room temperature, thereby producing precarbonized SW. SWs precarbonized at 600 or 700 ℃ are referred to as SW600C and SW700C, respectively. KOH activation required immersion of the precarbonized SWs into an aqueous solution of 8 mol L^{-1} KOH for 24 h. The mixture of the precarbonized SW and KOH solutionwas placed in a nickel container. For KOH activation, the mass ratio of impregnated KOH solid (not KOH solution) to precarbonized SW was 2. The container was heated in a tube furnace (TMF-700N, Az One Corp., Japan) under a N_2 gas flow (600 mL min^{-1}). The furnace temperature was increased to 900 ℃ at a heating rate of 5 ℃ min^{-1} and the final temperature was maintained for 1 h. After cooling the furnace to room temperature, the resultant SWAC was purified by washing in 1 mol L^{-1} HCl solution and then neutralized by rinsing using distilled water until the pH of the neutralization drainage stream reached a value of 7. Finally, the SWAC was dried at 100 ℃ for 24 h. The mass yield of KOH activation for the precarbonized SW was evaluated. The ACs produced from SWs precarbonized at 600 or 700 ℃ are referred to as SW600AC and SW700AC, respectively. SWAC was pulverized using a planetary ball mill (P-6, Fritch Japan Co., Ltd., Japan), and zirconia balls and a zirconia bowl. The median diameter of the SWAC powder was 3 μm, as determined using a laser diffraction particle size analyzer (SALD-200V, Shimadzu Corp., Japan).

RP25 (Kuraray Co., Ltd., Japan) and YP50F (Kuraray Co., Ltd., Japan) were employed as AC benchmarks intended for use in commercial EDLCs. ACs of RP25 and YP50F are produced from phenolic resin and coconut-shell, respectively. Using the aforementioned article size analyzer, the median diameters of RP25 and YP50F were determined to be 5 and 6 μm, respectively. These reference ACs were subjected to the same analyses as the SWACs.

2.2.2 Material characterization

Thermogravimetric analysis (TGA) was performed on the dried SW, and weight loss and weight loss derivative curves were obtained. Approximately 10 mg of the dried SW were heated from room temperature to 700 ℃ at a rate of 5 ℃ min^{-1} under an argon gas flow of 200 mL min^{-1} using a TGA system (TG8120, Rigaku Co., Ltd., Japan). Pore structure of the

precarbonized SWs and the SWACs was evaluated based on their N_2 adsorption-desorption isotherms at –196 ℃. The isotherms were obtained using a gas adsorption analyzer (Autosorb-3B, Quantachrome Instruments Inc., USA). Approximately 30 mg of powdered sample were degassed under vacuum at 200 ℃ for >8 h prior to the isotherm measurement. The Brunauer-Emmett-Teller (BET) theory [13] was used to calculate the specific surface area (S_{BET}) of the samples. The total pore volume (V_{total}) of the sample was determined by measuring the volume of nitrogen absorbed at a relative pressure of 0.99. The pore size distribution was obtained by meansof the quenched solid density functional theory (QSDFT) [14], using proprietary software (ASiQwin, version Quantachrome Instruments Inc., USA). The volumes of the micropores (V_{micro}) and mesopores (V_{meso}) were also calculated from the pore size distribution. The degree of graphitization of the precarbonized SWs was evaluated by means of Raman spectroscopy (DRX Raman Microscope, Thermo Fisher Scientific Inc., USA), in order to determine the optimal precarbonization temperature. The Raman spectra were acquired using a 532 nm laser,

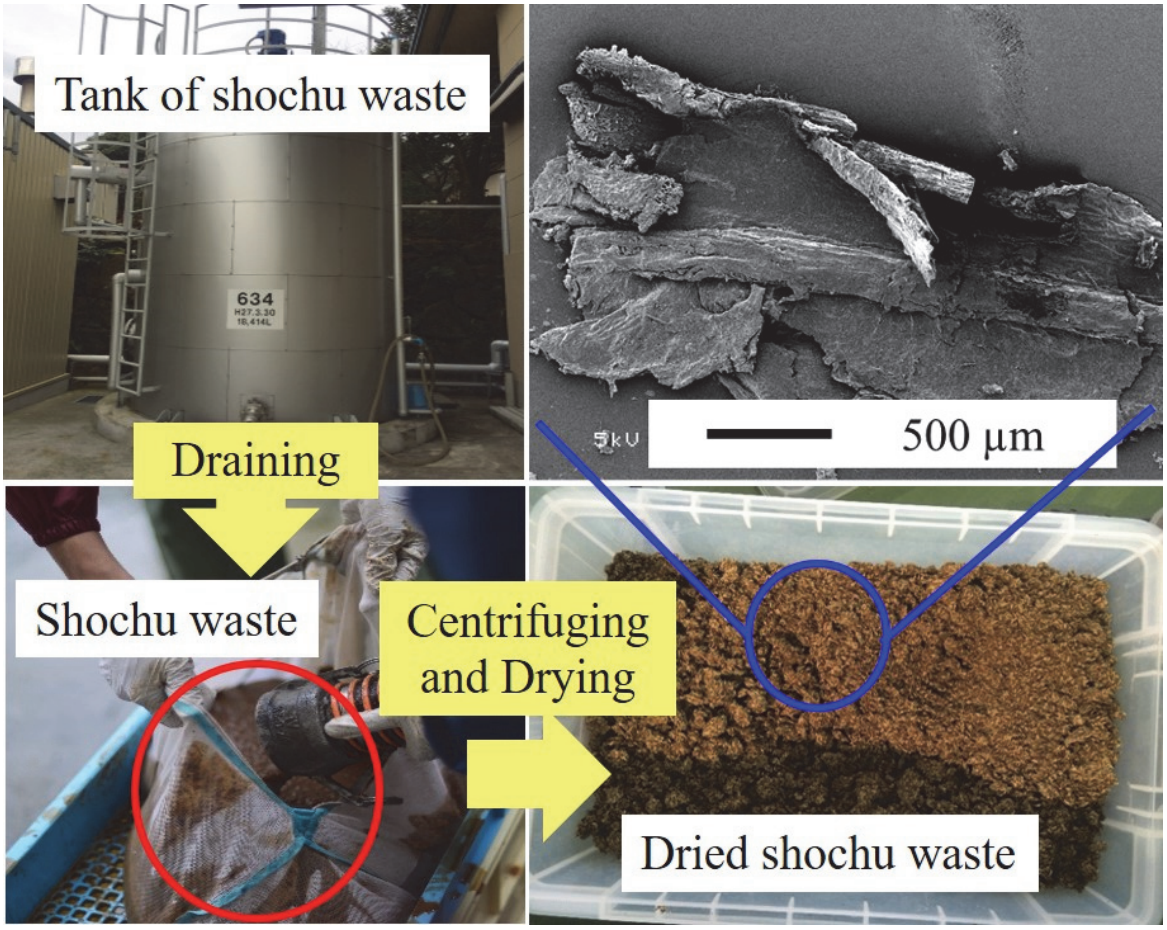

Fig. 2.1. Preparation procedure of wheat-origin shochu waste for the source material of ACs.

and the degree of graphitizationwas quantified by the peak intensity ratio of G-band (ca.1580 cm^{-1}) and D-band (ca.1360 cm^{-1}), defined as I_D/I_G. The G-band is attributed to the graphitic structure, and the D-band is due to defects and disorder in the structure [15]. Consequently, a higher I_D/I_G reflects a more disordered graphitic structure [16].

2.2.3 Electrochemical characterization

EDLC electrodes were prepared by mixing the AC, acetylene black (Denka Black, Denka Co., Ltd., Japan) and polytetrafluoroethylene (Polyflon D210-C, Daikin Industries, Ltd., Japan) in a mass ratio of 8:1:1 with a mortar and pestle. Ethanol was added and the mixture was pressed into a sheet. The sheet was punched out into 12.0 mm diameter disks of 0.30–0.33 mm thickness. The bulk density of the AC in the disk was also evaluated. The disk was pressed onto a circular piece of Al mesh (15.0 mm diameter) that was used as the current collector at a pressure of 0.5 MPa using a perpendicular press. The resultant EDLC electrodes were degassed at 140 ℃ for >4 h prior to cell assembly. Two-electrode cells made from Al (HS cell, Hohsen Corp., Japan) and 1 mL of non-aqueous electrolyte of tetraethylammonium tetrafluoroborate dispersed in 1 mol L^{-1} propylene carbonate ($TEA \cdot BF_4$/PC, Kishida Chemical Co., Ltd., Japan) was used. The cell was assembled in an argon-filled glove box (GBJF080R, Glovebox Japan Inc., Japan). The chargedischarge performance of the cells was evaluated by mean of cyclic voltammetry (CV) and galvanostatic charge-discharge (GCD) tests.

CV was carried out at scan rates of 1,10, and 100 mV s^{-1} using an electrochemical measurement system (HZ5000, Hokuto Denko Corp., Japan) and cell voltages in the range 0–2.5 V. The specific capacitance of the AC during the CV measurement (C_{CV}) was calculated from Eq. 2.1:

$$C_{GCD}(\mathrm{F\ g^{-1}}) = \frac{4Q}{mV} \tag{2.1}$$

where m (g) is the total mass of the AC incorporated both in the positive and negative electrodes of the EDLC cell, I_{CV} (A) is the current measured at various applied voltages, and Vs (V s^{-1}) is the voltage scan rate.

The rate and cycling stability of the AC were evaluated using GCD tests. Initially, to evaluate the rate stability, the GCD test was performed at current densities of 0.1–500 mA cm^{-2} using a battery charge-discharge system (HJ1005SD8, Hokuto Denko Corp., Japan), during which the cell voltage increased to 2.5 V for the charge process and decreased to 0 V for the discharge process. The detailed conditions in the GCD rate tests are shown in **Table 2.1**. The performance was evaluated at the specified cycle numbers. The specific capacitance of the AC in the GCD tests (C_{GCD}) was calculated using Eq. 2.2.

$$C_{GCD}(\mathrm{F\ g^{-1}}) = \frac{4Q}{mV} \tag{2.2}$$

Where, Q (C) is the charge released during the discharge process and V (V) is the maximum cell voltage. The volumetric specific capacitance (F cm^{-3}) was also calculated based on the bulk density of the AC in the EDLC electrode. In addition, a Ragone plot was created by calculating the energy density of the cell, E (Wh kg^{-1}), and power density of the cell, P (W kg^{-1}), from the GCD test results using Eqs. 2.3 and 2.4, respectively.

$$E\ (\mathrm{Wh\ kg^{-1}}) = \frac{1000W}{m} \tag{2.3}$$

$$P\ (\mathrm{W\ kg^{-1}}) = \frac{1000V'I}{m} \tag{2.4}$$

Where, W (Wh) is the energy released from the cell during the discharge process, V' (V) is the maximum cell voltage subtracted by the IR drop observed at the switching from charge to discharge processes, and I (A) is the discharge current. The volumetric energy density and volumetric power density, in respective units of Wh L^{-1} and W L^{-1}, were also calculated based on the electrode bulk density.

Table 2.1. Detailed conditions in GCD rate tests.

Sequence	Current density (mA cm^{-2})	Number of cycles	Cycle selected for the performance evaluation
1	0.1	2	Second
2	0.2	2	Second
3	0.5	2	Second
4	1.0	5	Third
5	2.0	5	Third
6	5.0	5	Third
7	10	11	Sixth
8	20	11	Sixth
9	50	11	Sixth
10	100	25	Thirteenth
11	200	25	Thirteenth
12	500	25	Thirteenth

Following the rate tests, the cycling stabilities of the specific capacitance of the ACs were evaluated. The EDLC cells were charged and discharged 2000 times at the constant current density of 10 mA cm^{-2}, during which the cell voltage range was set to 0–2.5 V. After the cycle tests, CV and the rate test were performed again under the extended cell voltage range of 0–3.0 V in order to verify the electrochemical stability of the AC experiencing a high cell voltage. The test conditions of CV and the rate tests were similar to those under the normal cell voltage range of 0–2.5 V. Ragone plots under the extended cell voltage range were also created. All measurements and analyses were carried out at 25 °C.

2.3 Results and discussion

2.3.1 Material characterization of precarbonized SWs and SWACs

The SWs were precarbonized at 600 or 700 °C and then chemically activated using KOH at 900 °C for 1 h. Material characterizations were first performed for the precarbonized SWs. TGA suggested that most of the weight loss of the dried SW occurred up to 500 °C, and the weight loss difference between 600 and 700 °C was slight (**Fig. 2.2**a). The largest weight loss was observed at 200–400 °C, and two peaks appeared on the weight loss derivative curve

at 280 and 320 °C (**Fig. 2.2**a). The weight loss at 200–400 °C and that at 340–550 °C were associated with the pyrolytic behaviors of hemicellulose and cellulose, and lignin, respectively [17-19].

The quantity of nitrogen adsorbed in SW600C and SW700C at –196 °C gradually increased with increasing relative pressure (**Fig. 2.2**b). The nitrogen uptake was larger on SW600C than SW700C, implying that the lower temperature allowed for a better development of the pore structure. Small hysteresis loops and rapid increases in the nitrogen uptake at the high relative pressure exceeding 0.95 on both isotherms proved the existence of mesopores and macropores, respectively. The Raman spectra of the precarbonized SWs displayed two distinct peaks at Raman shifts of 1360 and 1580 cm^{-1}, which were attributed to the D-band and G-band respectively, resulting from their carbonaceous structures (**Fig. 2.2**c). The D-band peak is associated with disordered graphitic structures produced in the precarbonized SWs. The precarbonization mass yields, textural properties, and I_D/I_G values representing the degree of graphitic disorder are shown in **Table 2.2**. The mass yield of SW700C was slightly lower than that of SW600C. However, lower S_{BET} and V_{total} and, higher I_D/I_G were observed on SW700C than on SW600C. The increase in the precarbonization temperature from 600 to 700 °C led to pore degeneration associated with disordering of the carbonaceous structure. The increase in I_D/I_G induced by raising the treatment temperature has been also reported for biowaste-derived carbons [20,21]. The material characterizations for the precarbonized SWs indicated that the porosity and carbon structure of SW600C were clearly different from those of SW700C.

Table 2.2. Material properties of the precarbonized SWs.

Precarbonizaton temperature (°C)	Precarbonization mass yield (%)	S_{BET} ($m^2\ g^{-1}$)	V_{total} ($cm^3\ g^{-1}$)	I_D/I_G
600	30.5	10.6	0.04	0.76
700	27.7	8.5	0.01	0.85

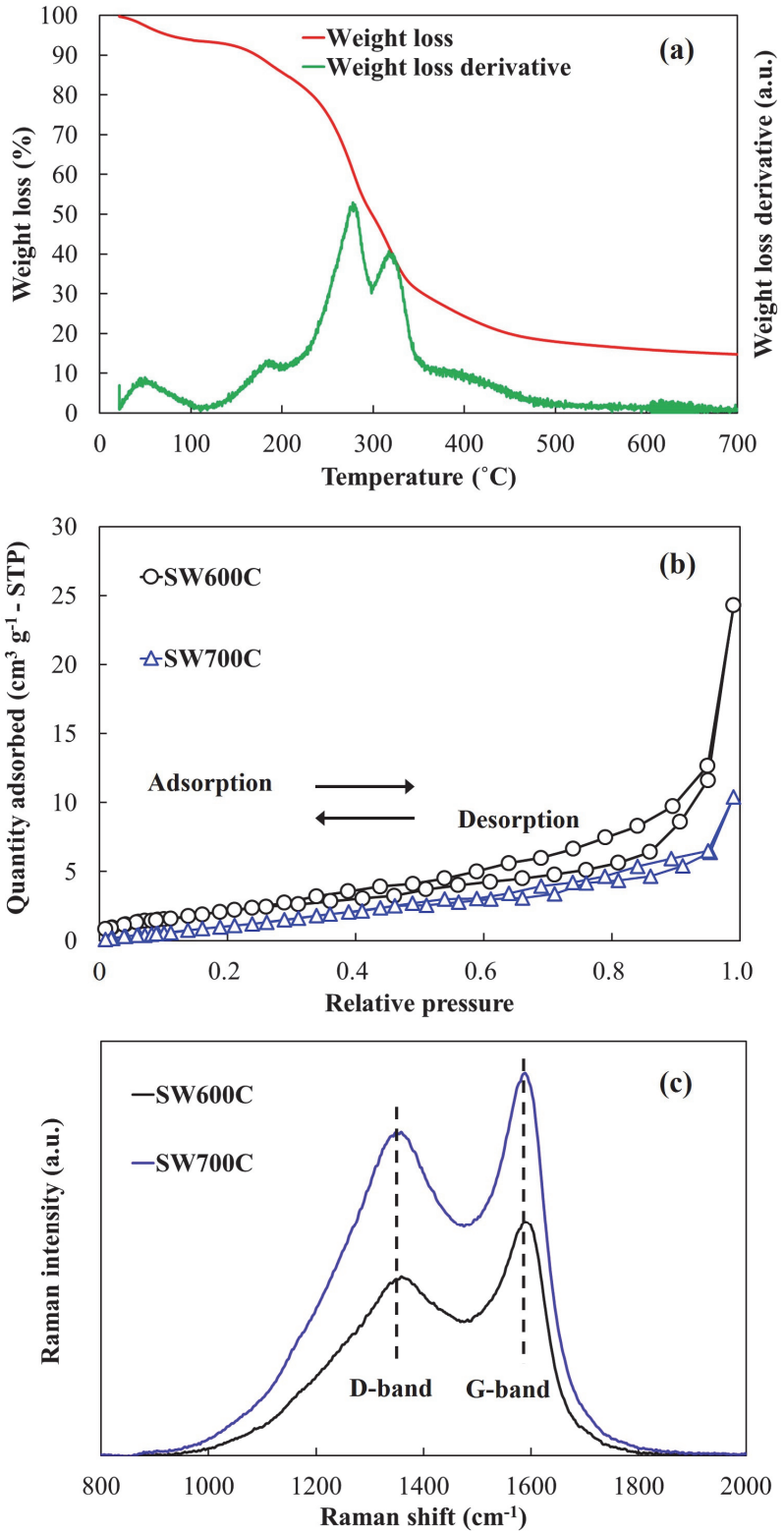

Fig. 2.2. Material characterization results of the precarbonized SWs. (a) TGA results of the dried SW; (b) nitrogen adsorption-desorption isotherms of the precarbonized SWs at –196 °C; (c) Raman spectra of the precarbonized SWs.

Figure 2.3 shows the nitrogen adsorption-desorption isotherms of the SWACs and the benchmark ACs at −196 °C, and their pore size distributions calculated by means of QSDFT. All the isotherms were basically classified into the IUPAC type-I, suggesting the dominant existence of micropores [22]. However, the isotherms of SW700AC and RP25 indicate a small IUPAC type-IV contribution, which is evidence of the formation of mesopore [22]. The nitrogen uptake for all samples greatly increased up to the relative pressure of 0.1. Gradual nitrogen uptake up to the relative pressure of 0.3 was observed for SW700AC and RP25. Nitrogen uptakes at the lower relative pressure of <0.4 and that at the relative pressure of 0.4−0.8 are generally associated with micropores and mesopores, respectively [23]. The pore size distributions calculated by QSDFT indicated that all the ACs had a variety of micropores and mesopores. The pore size distribution of YP50F was relatively similar to that of SW600AC, but small micropores (0.7−0.9 nm width) were less commonly observed in SW600AC. SW700AC exhibited a larger proportion of micropores of width 1−2 nm than did SW600AC. The peak pore width for SWACs increased (from 0.79 to 0.85 nm) because of the increased precarbonization temperature. Micropores of RP25 were predominantly 1−2 nm in width and mesopores were predominantly 2−3 nm in width, which differed from those of the SWACs and YP50F. The mass yield of KOH activation and textural parameters (S_{BET}, V_{total}, V_{micro}, and V_{meso}) for all the ACs and their bulk densities of the prepared electrodes are presented in **Table 2.3**. The mass yield of KOH activation for the SWACs indicated that a higher precarbonization temperature (700 °C) led to lower mass yield and higher textural parameters. All the ACs were dominated by micropores and supplementary mesopores. RP25 showed the highest textural parameters in all the ACs. The mesopore volume fractions in V_{total} for all the ACs ranged between 9.4 and 16.7 %. The highest mesopore fraction (16.7 %) and the second highest mesopore fraction (15.0 %) were observed in SW700AC and RP25, respectively. The bulk density of the AC in the prepared electrodes should be closely related to its volumetric electrochemical performance. The highest bulk density was observed in SW600AC, which also exhibited the lowest textural parameters. The higher textural parameters tended to lead to a lower bulk density. However, the textural parameters were not entirely consistent with the bulk density, which seems to be related to the size and shape of the AC particles.

Table 2.3. Material properties of the SWACs and benchmark ACs.

Sample	KOH activation mass yield (%)	S_{BET} ($m^2\ g^{-1}$)	V_{total} ($cm^3\ g^{-1}$)	V_{micro} ($cm^3\ g^{-1}$)	V_{meso} ($cm^3\ g^{-1}$)	Bulk density in the electrode ($g\ cm^{-3}$)
SW600AC	44.4	1787	0.85	0.70	0.08	0.70
SW700AC	29.0	2434	1.26	0.93	0.21	0.50
RP25	—	2680	1.40	1.08	0.21	0.52
YP50F	—	1713	0.84	0.67	0.10	0.60

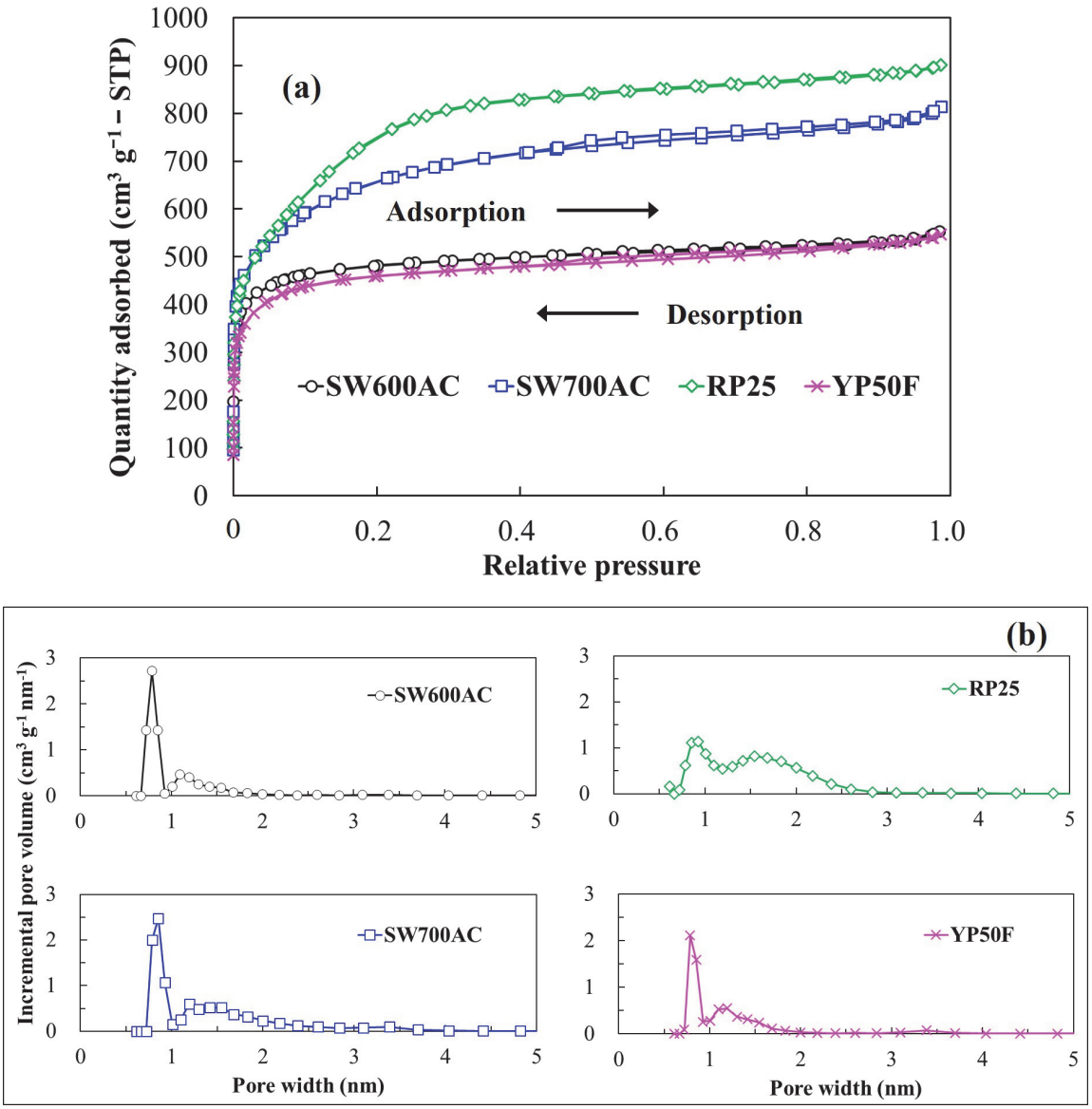

Fig. 2.3. Nitrogen adsorption-desorption isotherms of the SWACs and benchmark ACs at –196 °C, and their pore size distributions calculated by means of QSDFT. (a) Nitrogen adsorption-desorption isotherms; (b) QSDFT pore size distributions.

2.3.2 Electrochemical characterization

CV was carried out for the AC samples, and representative cyclic voltammograms at scan rates of 1, 10, and 100 mV s^{-1} are shown in **Fig. 2.4**. At the lowest scan rate, approximately symmetric rectangular curves were observed for all the ACs, implying that a double layer was formed at the interface between the AC surface and the electrolyte without any redox reactions.

With increasing scan rate, all the ACs exhibited more distorted and depressed curves, and lower specific capacitance. SW700AC showed the highest specific capacitance of all the ACs, regardless of the charge-discharge process and scan rate. The specific capacitance of SW600AC at a scan rate of 1 mV s^{-1} was larger than those of the benchmark ACs RP25 and YP50F. At the lower scan rate, the mass transfer time-rate of electrolytic ions within pores is more limited, facilitating the formation of an electric double-layer along the pore walls. This result indicates that, with limited ionic migration, the pores within SW600C can produce a wider double-layer than that of the benchmark ACs. However, with an increase in scan rate, SW600AC exhibited the most intensive distortion and depression of the CV curves. Generally, the distortion and depression are more enhanced when the EDLC cell includes higher electrical resistance in series connection with the double-layer capacitance. This is because the voltage applied to the EDLC cell is allocated to both capacitive and resistive components. The latter restricts the current response within the EDLC cell, resulting in distortion and depression. An increase in the scan rate can increase the amount of current passing between the opposing electrodes, promoting distortion and depression of the CV curves. Thus, SW600AC had the greatest resistive component of all the AC samples and allowed the largest decrement in specific capacitance when the scan rate increased.

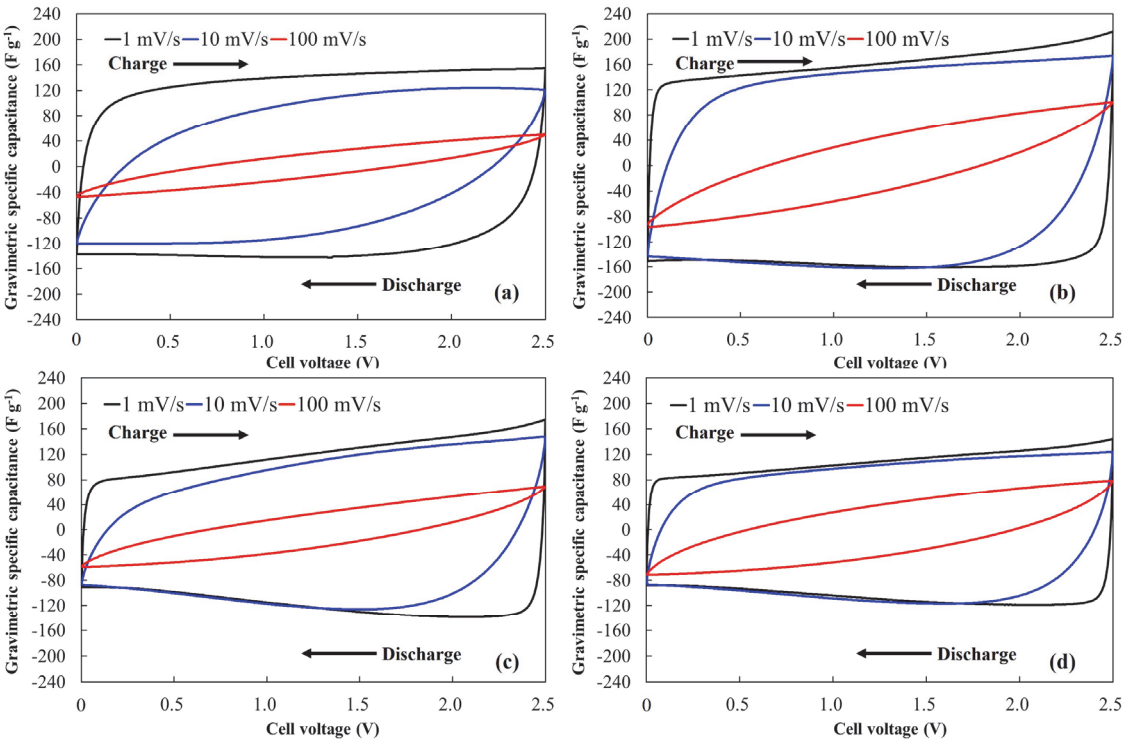

Fig. 2.4. CV curves of the SWACs and benchmark ACs at scan rates of 1, 10, and 100 mV s^{-1}. (a) SW600AC; (b) SW700AC; (c) RP25; (d) YP50F.

The gravimetric and volumetric specific capacitances as a function of current density are shown in **Fig. 2.5**. All the ACs exhibit a decrease in gravimetric and volumetric specific capacitances with increasing current density. Within the cell voltage range 0–2.5 V, the maximum gravimetric specific capacitances of SW600AC, SW700AC, RP25, and YP50F were 134, 152, 116, and 104 F g^{-1}, respectively, at the lowest current density of 0.1 mA cm^{-2}. The maximum volumetric specific capacitances of SW600AC, SW700AC, RP25, and YP50F were 75, 61, 48, and 50 F cm^{-3}, respectively. The gravimetric and volumetric specific capacitances of all the ACs tested under the extended cell voltage range 0–3.0 V demonstrated that the cell voltage extension was responsible for the lower gravimetric and volumetric specific capacitances of the SWACs. No changes were observed for RP25 and YP50F. SW700AC exhibited the highest gravimetric specific capacitance of all the ACs. The gravimetric specific capacitance of SW600AC was higher than that of the benchmark ACs within the current density range 0.1–2 mA cm^{-2}.

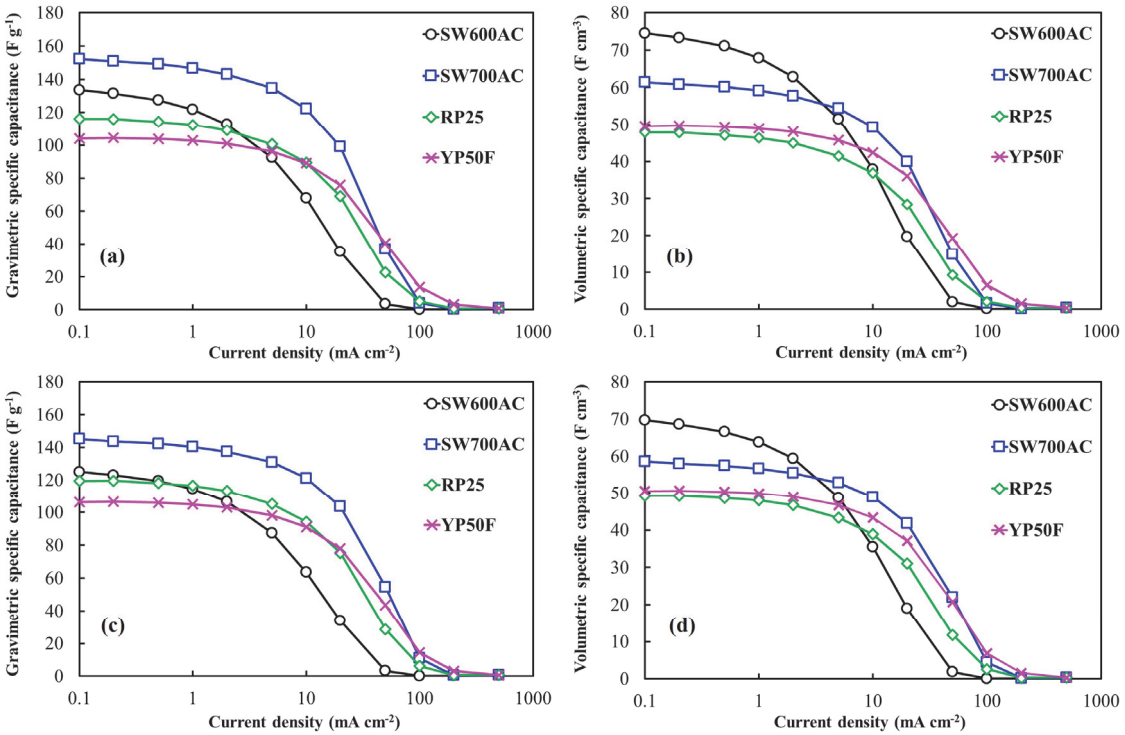

Fig. 2.5. Gravimetric and volumetric specific capacitances for the SWACs and benchmark ACs under cell voltage ranges of 0–2.5 V and 0–3.0 V. (a) Gravimetric specific capacitance, 0–2.5 V; (b) volumetric specific capacitance, 0–2.5 V; (c) gravimetric specific capacitance, 0–3.0 V; (d) volumetric specific capacitance, 0–3.0 V.

Figure 2.6 shows the relationship between the specific capacity and cell voltage for all the ACs during the GCD rate tests. Specific capacity is a time integral of the current that has passed through the EDLC cell per total mass of the AC in its positive and negative electrodes. An IR drop was observed when switching from both discharge to charge and charge to discharge. A higher current density led to a larger IR drop and a higher gradient of cell voltage variation. All the AC samples exhibited noticeable IR drops at a current density exceeding 5 mA cm^{-2}. The largest IR drops were observed for SW600AC, while YP50F exhibited the smallest IR drops. The second lowest IR drops were observed for SW700AC, indicating that SW700AC has not only a high gravimetric specific capacitance but also low internal resistance.

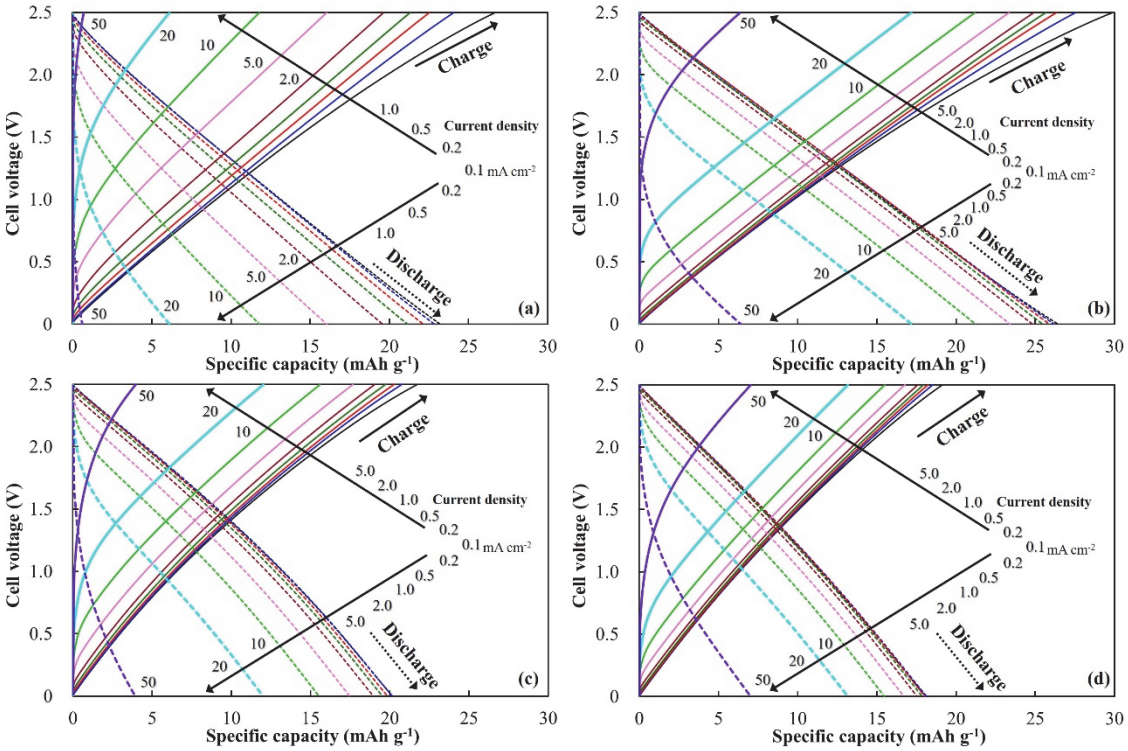

Fig. 2.6. Specific capacity vs. cell voltage in the GCD test under different current densities. (a) SW600AC; (b) SW700AC; (c) RP25; (d) YP50F.

Ragone plots, which show the relationship between power and energy density for sample ACs, were calculated using the GCD test data at current densities of 0.1−20 mA cm^{-2}. The gravimetric and volumetric Ragone plots of all the ACs tested under the cell voltage ranges 0−2.5 V and 0−3.0 V are shown in **Fig. 2.7**. Within the cell voltage range 0−2.5 V, SW700AC maintained a gravimetric energy density of >30 Wh kg^{-1} (maximum value 32 Wh kg^{-1}) up to a gravimetric power density of 200 W kg^{-1}. The maximum gravimetric energy densities of SW600AC, RP25, and YP50F were 27, 27, and 24 Wh kg^{-1}, respectively. It is worth noting that only SW600AC exhibited a significant reduction of gravimetric energy density at a power density exceeding 200 W kg^{-1}. In contrast, SW600AC exhibited the highest volumetric energy density of 15 Wh L^{-1} at the lower power density of <30 W L^{-1}. High (maximum 13 Wh L^{-1}) and stable (>10 Wh L^{-1} up to 300 W L^{-1}) volumetric energy density was achieved by SW700AC. The maximum volumetric energy densities of RP25 and YP50F were both 11 Wh L^{-1}, and the volumetric energy density of YP50F was maintained at a high level even at a high power density.

The extended range of cell voltage (0–3.0 V) contributed to a remarkable improvement in energy and power densities. The maximum gravimetric and volumetric energy densities of SW700AC were 44 Wh kg^{-1} and 18 Wh L^{-1}, respectively. For SW700AC, a high gravimetric energy density exceeding 30 Wh kg^{-1} was maintained up to 1000 W kg^{-1}, while a high volumetric energy density of >10 Wh L^{-1} was maintained up to 1000 W L^{-1}. The Ragone plots suggest that SW700AC has superior energy and power performance to those of the benchmark ACs. SW600AC displayed the highest volumetric energy density; however, this could not be maintained at the higher volumetric power density of >100 W L^{-1}.

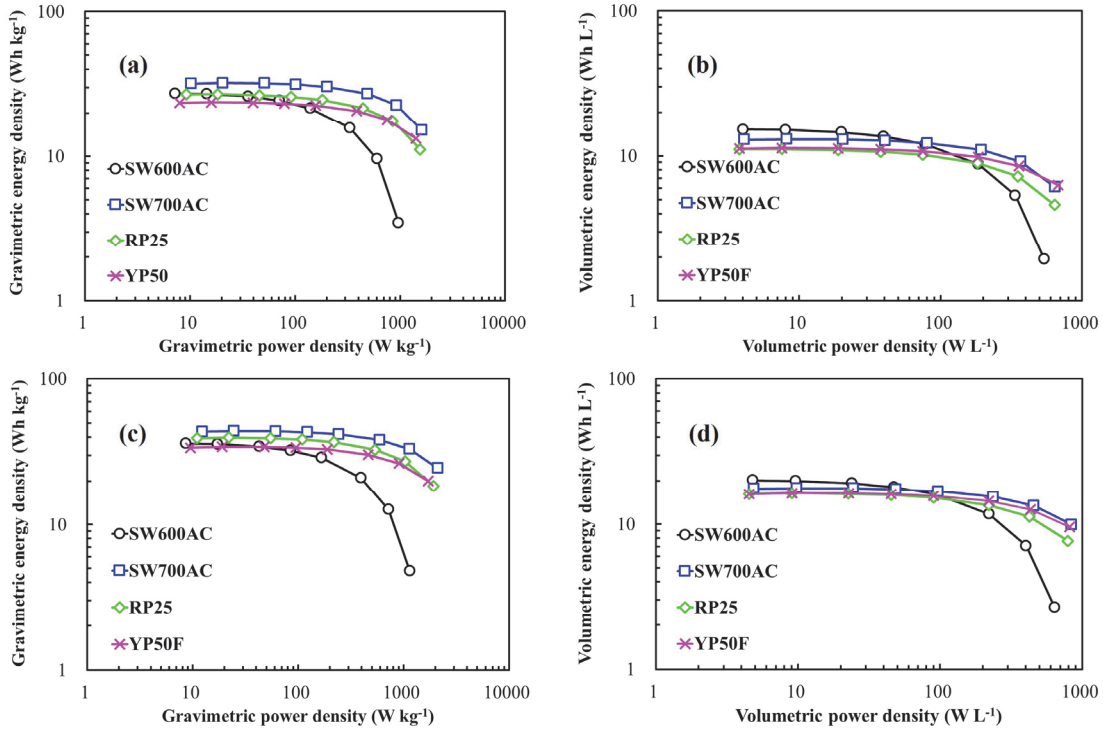

Fig. 2.7. Gravimetric and volumetric Ragone plots for the SWACs and benchmark ACs under cell voltage ranges of 0–2.5 V and 0–3.0 V. (a) Gravimetric plot, 0–2.5 V; (b) volumetric plot, 0–2.5 V; (c) gravimetric plot, 0–3.0 V; (d) volumetric plot, 0–3.0 V.

The specific capacitances of the ACs during the cyclic GCD test at a current density of 10 mA cm^{-2} are shown in **Fig. 2.8**. All the ACs retained their specific capacitances even after 2000 cycles of charge-discharge, during which SW700AC exhibited the highest gravimetric specific capacitance of >120 F g^{-1}. The specific capacitance retentions of SW600AC,

SW700AC, RP25, and YP50F were 98, 96, 96, and 96 %, respectively, which guaranteed the initial cycling stability of the SWACs. However, their long-term stability was not verified.

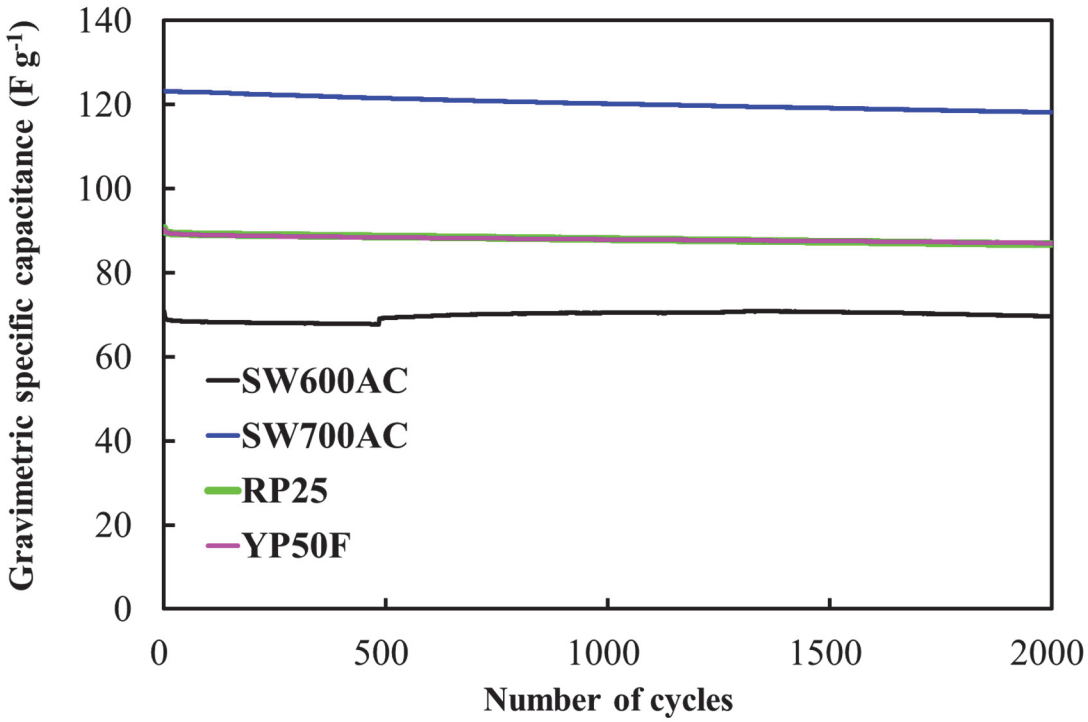

Fig. 2.8. Cyclic stability of the specific capacitance of the SWACs and benchmark ACs at the current density of 10 mA cm^{-2} under the cell voltage range of 0–2.5 V.

Table 2.4 shows the specific surface area and specific capacitance of biowaste-derived ACs reported in the literature. Although the S_{BET} of SW700AC was not markedly higher than those of other ACs, it displayed both excellent gravimetric and volumetric specific capacitance, revealing that Japanese distilled liquor-derived biowaste of SW can be used as a promising source material for ACs intended for EDLC electrodes.

Table 2.4. Specific surface area and specific capacitances of biowaste-derived ACs reported in the literature.

Source material of AC	Chemical activation agent	S_{BET} ($m^2\ g^{-1}$)	Gravimetric specific capacitance ($F\ g^{-1}$)	Volumetric specific capacitance ($F\ cm^{-3}$)	Type of electrolyte (Concentration)	Ref.
Coffee ground	$ZnCl_2$	1020	134	—	TEA·BF_4/AN (1 mol L^{-1})	[24]
Cherry stone	KOH	1300	120	45	TEA·BF_4/AN (1 mol L^{-1})	[25]
Cow dung	KOH	1984	121	—	TEA·BF_4/AN (1 mol L^{-1})	[26]
Tobacco rods	KOH	2115	146	—	TEA·BF_4/AN (1 mol L^{-1})	[27]
Carton box	KOH & NaOH	2731	178	—	TEA·BF_4/AN (1 mol L^{-1})	[28]
Hemp stem	KOH	2801	167	24	TEA·BF_4/PC (1.8 mol L^{-1})	[29]
Distillers dried grains	KOH	2959	150	—	TEA·BF_4/AN (1 mol L^{-1})	[30]
Rice husk	KOH	3097	174	—	TEA·BF_4/AN (1.5 mol L^{-1})	[31]
Shochu waste (SW700AC)	KOH	2434	152	61	TEA·BF_4/PC (1 mol L^{-1})	This work

AN: acetonitrile

2.3.3 Electrochemical performance of SWACs as the active material of EDLC electrode

SW700AC displayed excellent gravimetric and volumetric energy and power performance. The highest energy density was observed on SW600AC which was precarbonized at 600 °C, but its energy density considerably decreased at power densities exceeding 200 W kg^{-1}. The textural properties of SWACs were highly influenced by the precarbonization temperature, demonstrating that the precarbonization temperature had a decisive effect in determining the electrochemical performance of SWACs.

When the activation temperature reaches the boiling point of K (759 °C), vaporized K diffuses into the carbon layer in a carbonized carbon. Firstly, KOH reacts with elemental carbon as in Reaction 2.5. Then, K_2CO_3 and K_2O react with elemental carbon to form gaseous K and C-O-K as in Reactions 2.6 and 2.7. Aided by the high reactivity of K, KOH activation can result in selective carbon stripping, which leads to greater development of nano-scale pores and higher activation yield when compared with conventional gas (steam or CO_2) activation [32].

$$4KOH + C \rightarrow K_2O + K_2CO_3 + 2H_2 \quad (2.5)$$

$$K_2CO_3 + 2C \rightarrow 2K + 3CO \quad (2.6)$$

$$K_2O + C \rightarrow C\text{-}O\text{-}K + K \quad (2.7)$$

Based on the above reactions, SW700C was judged to be more sensitive to KOH activation and allowed greater development of micropores and mesopores with a lower activation mass yield compared with SW600C. Fewer pores and disordering of the carbonaceous structure occurred in the precursor when the precarbonization temperature was increased from 600 to 700 °C. It was reported that carbon elimination in KOH activation is more inhibited within crystalline regions than within disordered (amorphous) regions [33]. Therefore, in the present study, micropores and mesopores were more effectively produced in SW700C than in SW600C, with a corresponding lower KOH activation yield. The evaluation of pore size distribution demonstrated that pores larger than 1 nm are abundant within SW700AC; there were fewer such small pores observed on SW600AC and YP50F. The high volumetric energy density of SW600AC is attributed to the high AC bulk density of the electrode. The preponderance of narrow pores <1 nm is responsible for the low power performance of SW600AC. Hence, SW700AC, which contains a larger fraction of pores exceeding 1 nm, is able to maintain specific energy up to a power of 1000 W kg^{-1} or 1000 W L^{-1}. This circumstantial evidence suggests that SW700AC is best able to facilitate access of TEA^+ or BF_4^- ions into pores, relative to all other samples. The sizes of the TEA^+ and BF_4^- ions are 0.68 nm and 0.48 nm, respectively [34]. The adsorption of TEA^+ and BF_4^- ions into narrow pores (<1 nm) contributes to higher double-layer capacitance at low power densities. For rapid

charging and discharging, the occurrence of a proportion of pores 1−2 nm in width results in rapid and efficient ion transport, which contributes to high energy density that is maintained even during periods of high power density.

2.4 Conclusions

SWAC was produced by precarbonizing SW at 600 or 700 °C and then chemically activating the precarbonized SW using KOH. Material properties and electrochemical performance of the prepared SWACs were evaluated for their application as EDLC electrodes in comparison with two types of commercially available benchmark ACs. The highest gravimetric specific capacitance and highest gravimetric energy density were 152 F g^{-1} and 44 Wh kg^{-1}, respectively, for SW700AC with a specific surface area of 2434 m^2 g^{-1}. SW600AC, with a specific surface area of 1787 m^2 g^{-1}, exhibited the highest volumetric specific capacitance of 75 F cm^{-3} and a volumetric energy density of 18 Wh L^{-1}. We can make the following conclusions about SW utilization:

1. The precarbonization temperature has a decisive effect in determining the charge-discharge characteristics of SWACs.
2. SW700AC displays excellent gravimetric and volumetric energy and power performance, which is attributed to a well-balanced distribution of micropore sizes.
3. The highest volumetric energy density was obtainable from SW600AC, but its energy density considerably decreased at higher power densities, which was related to low accessibility of TEA^+ and BF_4^- ions to the surface of narrow micropores of width <1 nm.
4. SWACs are promising active materials for EDLC electrodes, which can display better energy-power performance than commercial benchmark ACs.

References

[1] K. Hayashi, Shochu distillery by-products as effective feed. J. Warm Regional Soc. Animal Sci., 55 (2012), 101–107 (in Japanese).

[2] T. Yamasaki, T. Aki, M. Shinozaki, M. Taguchi, S. Kawamoto, K. Ono, Utilization of shochu distillery wastewater for production of polyunsaturated fatty acids and xanthophylls. J. Biosci. Bioeng. 102 (2006) 323–327.

[3] T. Kobayashi, Y. Tang, T. Urakami, S. Morimura, K. Kida, Digestion performance and microbial community in full-scale methane fermentation of stillage from sweet potato-shochu production. J. Environ. Sci. 26 (2014) 423–431.

[4] R. Iigatani, T. Ito, F. Watanabe, M. Nagamine, Y. Suzuki, K. Inoue, Electricity generation from sweet potato-shochu waste using microbial fuel cells. J. Biosci. Bioeng. 128 (2019) 56–63.

[5] T. Suzuki, Y. Kamiya, M. Tanaka, I. Hattori K. Sato, The effects of feeding condensed rice distillers solubles as a substitute for soybean meal on milk production by dairy cows. Nihon Chikusan Gakkaiho, 81 (2010), 443–448 (in Japanese).

[6] F. Sun, L. Wang, Y. Peng, J. Gao, X. Pi, Z. Qu, G. Zhao, Y. Qin, Converting biomass waste into microporous carbon with simultaneously high surface area and carbon purity as advanced electrochemical energy storage materials. Appl. Surf. Sci. 436 (2018) 486–494.

[7] B. Liu, X. Zhou, H. Chen, Y. Liu, H. Li, Promising porous carbons derived from lotus seedpods with outstanding supercapacitance performance. Electrochim. Acta 208 (2016) 55–63.

[8] D. Liu, W. Zhang, H. Lin, Y. Li, H. Lu, Y. Wang, A green technology for the preparation of high capacitance rice husk-based activated carbon. J. Clean. Prod. 112 (2016) 1190–1198.

[9] M. Zhang, C. He, E. Liu, S. Zhu, C. Shi, J. Li, Q. Li, Activated carbon nanochains with tailored micro-meso pore structures and their application for supercapacitors. J. Phys. Chem. C 119 (2015) 21810–21817.

[10] Z. Zou, T. Liu, C. Jiang, Highly mesoporous carbon flakes derived from a tubular biomass for high power electrochemical energy storage in organic electrolyte. Mater. Chem. Phys. 223 (2019) 16–23.

[11] Z. Hao, J. Cao, Y. Wu, X. Zhao, L. Zhou, X. Fan, Y. Zhao, X. Wei, Preparation of porous carbons from waste sugar residue for high performance electric double-layer capacitor. Fuel Process. Technol. 162 (2017) 45–54.

[12] A. Silvestre-Albero, J. Silvestre-Albero, M. Martínez-Escandell, F. Rodríguez-Reinoso, Micro/mesoporous activated carbons derived from polyaniline: Promising candidates for CO_2 adsorption. Ind. Chem. Res. 53 (2014) 15398–15405.

[13] R.C. Bansal, M. Goyal, Activated carbon adsorption, CRC Press Inc., 2005 Boca Raton FL.

[14] A.V. Neimark, Y. Lin, P.I. Ravikovitch, M. Thommes, Quenched solid density functional theory and pore size analysis of micro-mesoporous carbons. Carbon 47 (2009) 1617–1628.

[15] A. Eckmann, A. Felten, A. Mishchenko, L. Britnell, R. Krupke, K.S. Novoselov, C. Casiraghi, Probing the nature of defects in graphene by Raman spectroscopy. Nano Lett. 12 (2012) 3925–3930.

[16] C. Guizani, K. Haddad, L. Limousy, M. Jeguirim, New insights on the structural evolution of biomass char upon pyrolysis as revealed by the Raman spectroscopy and elemental analysis. Carbon 119 (2017) 519–521.

[17] H. Yang, R. Yan, H. Chen, C. Zheng, D.H. Lee, D.T. Liang, In-depth investigation of biomass pyrolysis based on three major components: hemicellulose, cellulose and lignin. Energy Fuels 20 (2006) 388–393.

[18] H.C. Yoon, P. Pozivil, A. Steinfeld, Thermogravimetric pyrolysis and gasification of lignocellulosic biomass and kinetic summative law for parallel reactions with cellulose, xylan, and lignin, Energy Fuels 26 (2012) 357–364.

[19] A. Zheng, L. Jiang, Z. Zhao, Z. Huang, K. Zhao, G. Wei, X. Wang, F. He, H. Li, Impact of torrefaction on the chemical structure and catalytic fast pyrolysis behavior of hemicellulose, lignin, and cellulose. Energy Fuels 29 (2015) 8027–8034.

[20] M. Asadullah, S. Zhang, C. Li, Evaluation of structural features of chars from pyrolysis of biomass of different particle sizes. Fuel Process. Technol. 91 (2010) 877–881.

[21] J. Han, J.H. Kwon, J. Lee, J.H. Lee, K.C. Roh, An effective approach to preparing partially graphitic activated carbon derived from structurally separated pitch pine biomass. Carbon 118 (2017) 431–437.

[22] M. Thommes, K. Kaneko, A.V. Neimark, J.P. Olivier, F. Rodriguez-Reinoso, J. Rouquerol K.S.W. Sing, Physisorption of gases, with special reference to the evaluation of surface area and pore size distribution (IUPAC Technical Report). Pure Appl. Chem. 87 (2015) 1051–1069.

[23] F. Wu, J. Gao, X. Zhai, M. Xie, Y. Sun, H. Kang, Q. Tian, H. Qiu, Hierarchical porous carbon microrods derived from albizia flowers for high performance supercapacitors. Carbon 147 (2019) 242–251.

[24] T.E. Rufford, D. Hulicova-Jurcakova, E. Fiset, Z. Zhu, G.Q. Lu, Double-layer capacitance of waste coffee ground activated carbons in an organic electrolyte. Electrochem. Commun. 11 (2009) 974–977.

[25] O. Olivares-Marin, J.A. Fernandez, M.J. Lazaro, C. Fernandez-Gonzalez, A. Macias-Garcia, V. Gomez-Serrano, F. Stoeckli, T.A. Centeno, Cherry stones as precursor of activated carbons for supercapacitors. Mater. Chem. Phys. 114 (2009) 323–327.

[26] D. Bhattacharjya, J. Yu, Activated carbon made from cow dung as electrode material for electrochemical double layer capacitor. J. Power Sources 262 (2014) 224–231.

[27] Y. Q. Zhao, M. Lu, P. Tao, Y. Zhang, X. Gong, Z. Yang, G. Zhang, H. Li, Hierarchically porous and heteroatom doped carbon derived from tobacco rods for supercapacitors. J. Power Sources 307 (2016) 391–400.

[28] D. Wang, G. Fang, T. Xue, J. Ma, G. Geng, A melt route for the synthesis of activated carbon derived from carton box for high performance symmetric supercapacitor applications. J. Power Sources 307 (2016) 401–409.

[29] W. Sun, S.M. Lipka, C. Swartz, D. Williams, F. Yang, Hemp-derived activated carbons for supercapacitors. Carbon 103 (2016) 181–192.

[30] H. Jin, X. Wang, Z. Gu, G. Anderson, K. Muthukumarappan, Distillers dried grains with soluble (DDGS) bio-char based activated carbon for supercapacitors with organic electrolyte tetraethylammonium tetrafluoroborate. J. Environ. Chem. Eng. 2 (2014) 1404–1409.

[31] Y. Gao, L. Li, Y. Jin, Y. Wang, C. Yuan, Y. Wei, G. Chen, J. Ge, Porous carbon made from rice husk as electrode material for electrochemical double layer capacitor. Appl. Energy

153 (2015) 41–47.

[32] Y. Kan, Q. Yue, B. Gao, Q. Li, Comparison of activated carbons from epoxy resin of waste printed circuit boards with KOH activation by conventional and microwave heating methods. J. Taiwan Inst. Chem. Eng. 68 (2016) 440–445.

[33] P.R. Choi, E. Lee, S.H. Kwon, J.C. Jung, M. Kim, Characterization and organic electric-double-layer-capacitor application of KOH activated coal-tar-pitch-based carbons: Effect of carbonization temperature. J. Phys. Chem. Solids 87 (2015) 72–79.

[34] E. Redondo, J. Segalini, J. Carretero-Gonzalez, E. Goikolea, R. Mysyk, Relation between texture and high-rate capacitance of oppositely charged microporous carbons from biomass waste in acetonitrile-based supercapacitors. Electrochim. Acta 293 (2019) 496–503.

Effect of ball milling on EDLC performance of AC with very high specific surface area

3.1 Introduction

EDLC electrodes have been chiefly prepared in two ways. One is to coat a slurry comprising active material, conductive agent and binder onto an Al foil used as the current collector [1-3]. The other is to knead the mixture composed of active materials, conductive agent and binder, and then to mold it into a sheet. The sheet is pressed and attached with the mesh-like current collector or is adhered with a foil-like current collector [4-6]. The particle size of AC used as the active material can be industrially recommended to be in the range of 4−8 μm [7]. A correlation between the particle size of the AC active material and the charge–discharge performance of EDLC has been explored. It was demonstrated that, for the EDLC electrodes, an increase in the AC particle size led to a decrease in the specific capacitance and an increase in the equivalent series resistance (ESR) [2]. The ESR of the electrode is chiefly attributed to the electrolyte, the contact and the intrinsic resistance. The contact resistance is related to the contact degree between the AC particles, and that between the particles and the current collector. The intrinsic resistance is dependent on the conductivity of AC particles, which have a relation with their graphitization degree and their porosity. The specific surface area of the used AC, and the exposure degree of pore-walls that allow access of the electrolytic ions so as to form an electric double-layer, are decisive factors of the specific capacitance of EDLC electrode. The exposure degree of pore-walls is affected by the affinity of AC particles with the binder, and the level of binder added in the electrode. AC particle size and its size uniformity have been known to participate in the ESR [4-6, 8]. The role of AC particle size on the diffusivity of ions in the EDLC electrodes has been also investigated, suggesting that smaller AC particles facilitated ion-transportation in the EDLC electrodes [9].

In order to obtain the desired particle size, or desired particle size distribution of ACs, a ball milling technique has been well employed. It has been shown that the porous structure and surface morphology of ACs can vary during the balling milling process [10-17]. The electrodes using nanoscale carbide-derived AC powders displayed excellent electrical contact

between the particles across the electrode and facilitated ion-movement within the pores, maintaining the specific capacitance of the electrode even at high current densities [18]. The AC processed by the prolonged ball milling decreased the specific capacitance due to particle agglomeration [17]. The presence of submicron sized particles in discrete AC particle clusters led to performance and cycle stability degradation of the electrodes [4]. In the above-mentioned studies, the specific surface areas of the used ACs were in the range of 880−2200 m^2 g^{-1}. Increasing the gravimetric energy and power densities of the EDLC electrode requires highly porous ACs. However, there are few reports on the optimization of the particle size of ACs with a very high specific surface area (~3000 m^2 g^{-1}), which are intended for use in the fabrication of high-performance EDLC electrodes. The effects of the pulverization degree of ACs with such high specific surface area on their EDLC performances have not been explored so far.

In the present study, the EDLC performances of ACs with specific surface areas of around 3000 m^2 g^{-1} were examined under the use of a non-aqueous electrolyte, which has been a mainstream electrolyte for high-performance commercial EDLCs. We investigated the variation in the textural properties and the particle morphology of the highly porous ACs during planetary ball milling. The charge–discharge performances (specific capacitance, rate and cyclic stabilities, and Ragone plot, from the viewpoints of both the gravimetric and volumetric performances) of EDLCs using AC active materials of various particle sizes were evaluated. In order to achieve the greatest gravimetric or volumetric EDLC performance, the ball milling process was optimized for the highly porous ACs.

3.2 Materials and methods

3.2.1 Ball milling and materials characterization

Maxsorb (Kansai coke and chemicals Co., Ltd., Amagasaki, Japan), which was manufactured from petroleum coke by means of KOH activation, was used as the AC active material. For the ball milling process, planetary ball milling equipment (P-6, Fritch Japan Co., Ltd., Yokohama, Japan), a zirconia bowl with a 80 mL-milling space, and two types of zirconia balls (ϕ10.0 mm or ϕ19.5 mm) were employed. In air atmosphere, one gram of the sample AC was pulverized for 10, 90, and 120 min using the five ϕ19.5 mm balls at a rotation speed of 400

rpm. The ACs, pulverized for 10, 90, and 120 min, were termed AC10, AC90, and AC120, respectively. The AC milled for 10 min using the thirteen ϕ10.0 mm balls (ϕ19.5 mm balls were not mixed) at the similar rotation speed was also prepared to realize the particle size between those of AC0 and AC10, which was termed ACS10. The AC sample which was not milled was termed AC0.

Crystalline structures of the ACs was analyzed using an X-ray diffractometer (RINT-2020V, Rigaku Corp., Askishima, Japan) with Cu-Kα radiation (wavelength: 0.15418 nm), providing X-ray diffraction (XRD) patterns of the ACs. The disorder degree of graphene structures of the ACs was also evaluated using a microscopic Raman spectrometer (LabRAM HR Evolution, Horiba Ltd., Kyoto, Japan). The Raman spectra were acquired using a laser of 633 nm-wave length. The degree of graphene disorder of ACs was quantified by the peak intensity ratio of the G-band (ca. 1580 cm^{-1}) and D-band (ca. 1360 cm^{-1}), which was defined as I_d/I_g. The D-band and G-band corresponded to the in-plane vibrations of sp^2 bonded carbon structures with structural defects and the in-plane vibrations of sp^2 bonded graphene carbon structures, respectively [19-21]. Thus, I_d/I_g is an indication of disorder degree of graphene sheets.

The N_2 adsorption–desorption isotherms of the ACs were measured using a gas adsorption analyzer (Autosorb-3B, Quantachrome Instruments Inc., Florida, USA) at −196 °C. Approximately 30 mg of powdered AC was degassed under vacuum at 200 °C for >8 h prior to the isotherm measurement. The Brunauer–Emmett–Teller (BET) theory was used to calculate the specific surface area (S_{BET}) of the AC samples using the adsorption isotherm at a relative pressure of 0.05−0.10. The total pore volume (V_{total}) of the sample was determined by measuring the volume of nitrogen absorbed at the relative pressure of 0.99. The quenched solid density functional theory (QSDFT) was used to obtain the pore size distribution [22, 23], with aid from the proprietary software (ASiQwin, version 1.11, Quantachrome Instruments Inc., Florida, USA). Based on the pore size distributions, the volumes of the micropores (V_{micro}) and mesopores (V_{meso}) were calculated.

The particle size distribution of the produced AC powder was analyzed using a laser diffraction particle size analyzer (SALD-200V, Shimadzu Corp., Kyoto, Japan). The average

particle diameter, and the cumulative 25 %, 50 % (median value), and 75 % particle diameters, were acquired and were defined as D_{ave}, D_{25}, D_{50}, and D_{75}, respectively.

3.2.2 Electrochemical characterization

AC as the active material, acetylene black (Denka Black, Denka Kagaku Co., Ltd., Tokyo, Japan) as the conductive agent, and polytetrafluoroethylene (Polyflon D210-C, Daikin Industries, Ltd., Osaka, Japan) as the binder were mixed in a mass ratio of 8:1:1 by a mortar and pestle, with added ethanol. The mixture was pressed into a sheet, then it was punched out into disks of ϕ12 mm. The mass of AC in the electrode and the electrode thickness were measured, providing the AC bulk density. The morphology of electrodes was microscopically observed using a scanning electron microscope (VE-8800, Keyence Corp., Osaka, Japan).

Meso- and microporosity, and interparticle porosity of the prepared EDLC electrodes were evaluated using a mercury porosimeter (PASCAL 140 and 240, Thermo Fisher Scientific K.K., Tokyo, Japan). For each AC sample, 4 pieces of the same type electrode which were previously degassed in vacuum at 140 °C for >6 h were subjected to a mercury intrusion and extrusion sequence. This sequence was performed in the low pressure range (0.2–400 kPa) using PASCAL 140 and in the high pressure range (up to 200 MPa) using PASCAL 240, providing the mercury intrusion volume at different equilibrated mercury pressures. The pore size distributions of EDLC electrodes were calculated using the Washburn equation [24] with aid from a software installed in the above mercury porosimeter, where the shape of pores were assumed to be a cylinder.

The disk was pressed onto a ϕ15 mm Al mesh at a pressure of 0.5 MPa using a perpendicular press. The disk attached with an Al mesh was employed as the electrode. The electrodes were dried under a vacuum at 140 °C for >6 h prior to cell assembly. A two-electrode cell made from Al (HS cell, Hohsen Corp., Osaka, Japan) was assembled in a glove box (GBJF080R, Glovebox Japan Inc., Inagi, Japan) filled with argon gas. The cell was constituted from two identical electrodes, a ϕ23 mm paper-based separator (TF4050, Nippon Kodoshi Corp., Kochi, Japan), and 1 mL-electrolyte. The electrolyte was tetraethylammonium

tetrafluoroborate at 1 mol L^{-1} dispersed in propylene carbonate (TEA·BF_4/PC, Kishida Chemical Co., Ltd., Osaka, Japan).

The current passing through the electrodes under voltage application across the cell terminals was evaluated by cyclic voltammetry (CV). CV was performed at the scan rates of 1, 10, and 100 mV s^{-1} using an electrochemical measurement system (HZ5000, Hokuto Denko Corp., Tokyo, Japan) at the cell voltage range of 0–2.5 V. The specific capacitance of the AC during the CV measurement (C_{cv}) was calculated from Eq. 3.1.

$$C_{cv}(\mathrm{F\ g^{-1}}) = \frac{4I_{cv}}{mV_s} \tag{3.1}$$

where m (g) is the total mass of AC incorporated in both the positive and negative electrodes, I_{cv} (A) is the current measured at different applied voltage, and V_s (V s^{-1}) is the voltage scan rate.

A battery charge–discharge system (HJ1005SD8, Hokuto Denko Corp., Tokyo, Japan) was used to perform the galvanostatic charge–discharge (GCD) tests for the EDLC cells, during which the cell voltage was increased to 2.5 V for the charge process and was decreased to 0 V for the discharge process at different current densities of 0.1–100 mA cm^{-2}. **Table 3.1** shows the detailed conditions in the GCD rate tests. The charge–discharge performances at different current densities were evaluated at the specified cycle numbers. The gravimetric specific capacitance of the AC in the GCD tests (C_{GCD}) was calculated using Eq. 3.2.

$$C_{GCD}(\mathrm{F\ g^{-1}}) = \frac{4Q}{mV'} \tag{3.2}$$

where Q (C) is the charge released during the discharge process and V' (V) is the maximum cell voltage (2.5 V) subtracted by the IR drop observed at the switching from charge to discharge processes. The IR drop is the voltage drop caused by the internal resistance, which can be represented by ESR. The relationship between the current density and the ESR at the switching of charge to discharge was also obtained for all types of ACs. The volumetric specific

capacitance (F cm^{-3}) was also calculated based on the AC bulk density in the electrode. The charge or discharge specific capacity of the AC was also defined to be a time-integral of current divided by *m*, providing the specific capacity−cell voltage profile of the AC. The Ragone plot was created by calculating the energy density of the electrode, *E* (Wh kg^{-1}), and power density of the electrode, *P* (W kg^{-1}), from the GCD test results using Eqs. 3.3 and 3.4, respectively.

$$E\ (\mathrm{Wh\ kg^{-1}}) = \frac{1000W}{m} \tag{3.3}$$

$$P\ (\mathrm{W\ kg^{-1}}) = \frac{1000V'I}{m} \tag{3.4}$$

where *W* (Wh) is the energy released from the cell during the discharge process, and *I* (A) is the discharge current. Using the AC bulk density in the electrode, the volumetric energy density and volumetric power density, in respective units of Wh L^{-1} and W L^{-1}, were also calculated.

Table 3.1. Conditions for the GCD rate tests.

Sequence	Current density [1] (mA cm^{-2})	Number of cycles	Cycle selected for the performance evaluation
1	0.1	2	Second
2	0.2	2	Second
3	0.5	2	Second
4	1.0	5	Third
5	2.0	5	Third
6	5.0	5	Third
7	10	11	Sixth
8	20	11	Sixth
9	50	11	Sixth
10	100	25	Thirteenth

[1] Electrode area is 1.13 cm^2 (ϕ12 mm)

For the evaluation of electrode cycle stability, following the GCD rate test, the EDLC cell was charged and discharged 2000 times at the constant current density of 10 mA cm^{-2} under the similar cell voltage range. The gravimetric specific capacitance of the electrode was measured as a function of the number of cycles. All measurements and analyses were performed at 25 °C.

3.3 Results and discussion

3.3.1 Material properties of the milled ACs

The ACs with different particle sizes were produced by changing the ball milling process. XRD patterns and Raman spectra for the milled ACs were obtained and are shown in **Fig. 3.1**. In the XRD patterns, all ACs exhibited two gentle humps, attributable to the graphitic (002) and (100) planes at the 2θ values of ca. 23° and 43°, respectively. Only a tiny peak (marked by an inverted triangle) was observed in the XRD pattern of AC120 at 30°, which was confirmed to be caused by debris of zirconia balls and bowl used for the AC milling [25]. It was clearly indicated that crystalline structures of all the ACs were amorphous, and the milling process had little impact on the graphitization degree. Raman spectra of all the ACs displayed the D-band and G-band peaks resulting from carbonaceous structures. The I_d/I_g values of AC0, AC10, ACS10, and AC90 were similar; while that of AC120 was slightly lower than the others. The lowering of I_d/I_g indicates that AC120 alleviated the disorder of graphene sheets. From both the results of X-ray diffractometry and Raman spectroscopy, it was shown that, when the ball-milling time was limited to within 120 min, the structural changes of the AC during the ball-milling were minor.

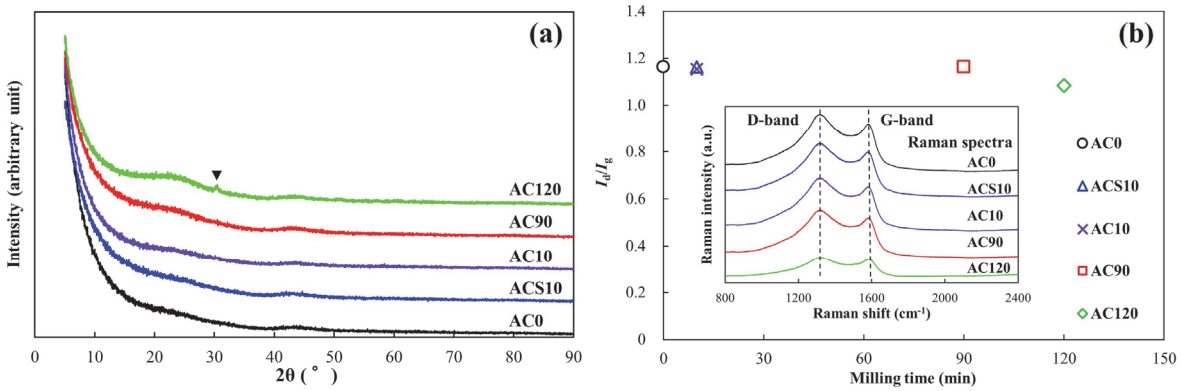

Fig. 3.1. XRD patterns, and a relationship between the milling time and I_d/I_g value for the milled ACs. (a) XRD patterns, (b) I_d/I_g value with their Raman spectra.

Table 3.2. Textural properties of the milled ACs.

Sample name	S_{BET} ($m^2\ g^{-1}$)	V_{total} ($cm^3\ g^{-1}$)	V_{micro} ($cm^3\ g^{-1}$)	V_{meso} ($cm^3\ g^{-1}$)
AC0	3198	1.78	1.27	0.38
ACS10	3073	1.73	1.23	0.37
AC10	3041	1.72	1.22	0.37
AC90	2755	1.56	1.09	0.34
AC120	2448	1.36	0.96	0.28

Figure 3.2 shows the nitrogen adsorption-desorption isotherm at the temperature of –196 °C. All of the nitrogen adsorption isotherms exhibited a slightly hysteretic behavior at the relative pressure of 0.2−0.8. These can be categorized into an IUPAC type I (b) isotherm, suggesting pore size distributions over a broader range including wider micropores and possibly narrow mesopores (<~2.5 nm) [26]. It was clearly found that, over the entire range of relative pressures, the adsorption quantity decreased with the milling time. All of the ACs allowed a development of pores that were 0.6−1.0 nm and 1.2−3.0 nm. The peaks of pore width for the ACs subjected to the ball milling shifted to the smaller side. **Table 3.2** shows the textural properties of the ACs based on the above isotherms and pore size distributions. All of the textural parameters decreased with the milling time. The S_{BET} and V_{total} of the non-milled AC (AC0) were measured to be 3198 $m^2\ g^{-1}$, and 1.78 $cm^3\ g^{-1}$, respectively. The S_{BET} of AC90 and AC120 were respectively 2755 and 2448 $m^2\ g^{-1}$, indicating that the ball milling for 90 or 120

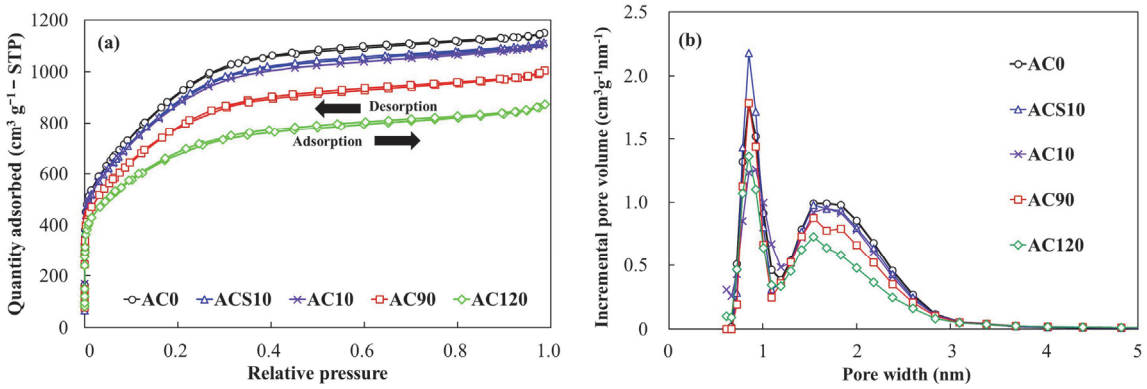

Fig. 3.2. Nitrogen adsorption–desorption isotherms of the milled ACs at –196 °C, and their pore size distributions. (a) Nitrogen adsorption–desorption isotherms; (b) pore size distributions.

min induced surface area decrements of 13.9% and 23.5%, respectively. The ratio of V_{micro} to V_{tatal} and that of V_{meso} to V_{tatal} were respectively ~70% and ~20%, which were similar in all ACs.

Figure 3.3 shows the surface morphology of the electrodes using the milled ACs, and their particle size distributions. With increasing the milling time, the size of AC particles decreased, and the gap between the AC particles at the electrode surfaces decreased. It was observed that dense surface structures were produced for the electrodes comprising ACs that were subjected to a long milling time (AC90 and AC120). The particle size distributions suggested that the mode (most frequent) particle size of AC decreased with the milling time. AC0 was composed of course particles, and allowed a dominant existence of particles at >50 μm in diameter, while AC120 comprised only fine particles with diameters of <6 μm. It should be noticed that AC90 exhibited two peaks on its particle size distribution, which were attributed to milled fine particles at <8 μm and residual large particles at 20−30 μm. Particle properties of the milled ACs calculated based on the above distributions are shown in **Table 3.3**. AC0 and ACS10, which were composed of large-size particles, did not show coincident D_{ave} and D_{50}. It was also confirmed that 75% of their particles were within $2\times D_{50}$ for AC10, AC90, and AC120, indicating that those were sufficiently pulverized rather than AC0 and ACS10. The ACs pulverized for 150 min using the five ϕ19.5 mm balls were also prepared, and its D_{ave} was measured to be 3.4 μm. It was suggested that excessive milling induced a particle agglomeration, and the milling for 120 min attained the greatest pulverization.

Table 3.3. Particle properties of the milled ACs.

Sample name	D_{ave} (μm)	D_{25} (μm)	D_{50} (μm)	D_{75} (μm)
AC0	74.9	42.5	70.7	135.1
ACS10	20.0	10.6	26.1	37.5
AC10	11.6	6.8	11.7	19.7
AC90	3.0	1.9	2.8	4.2
AC120	2.2	1.6	2.4	3.3

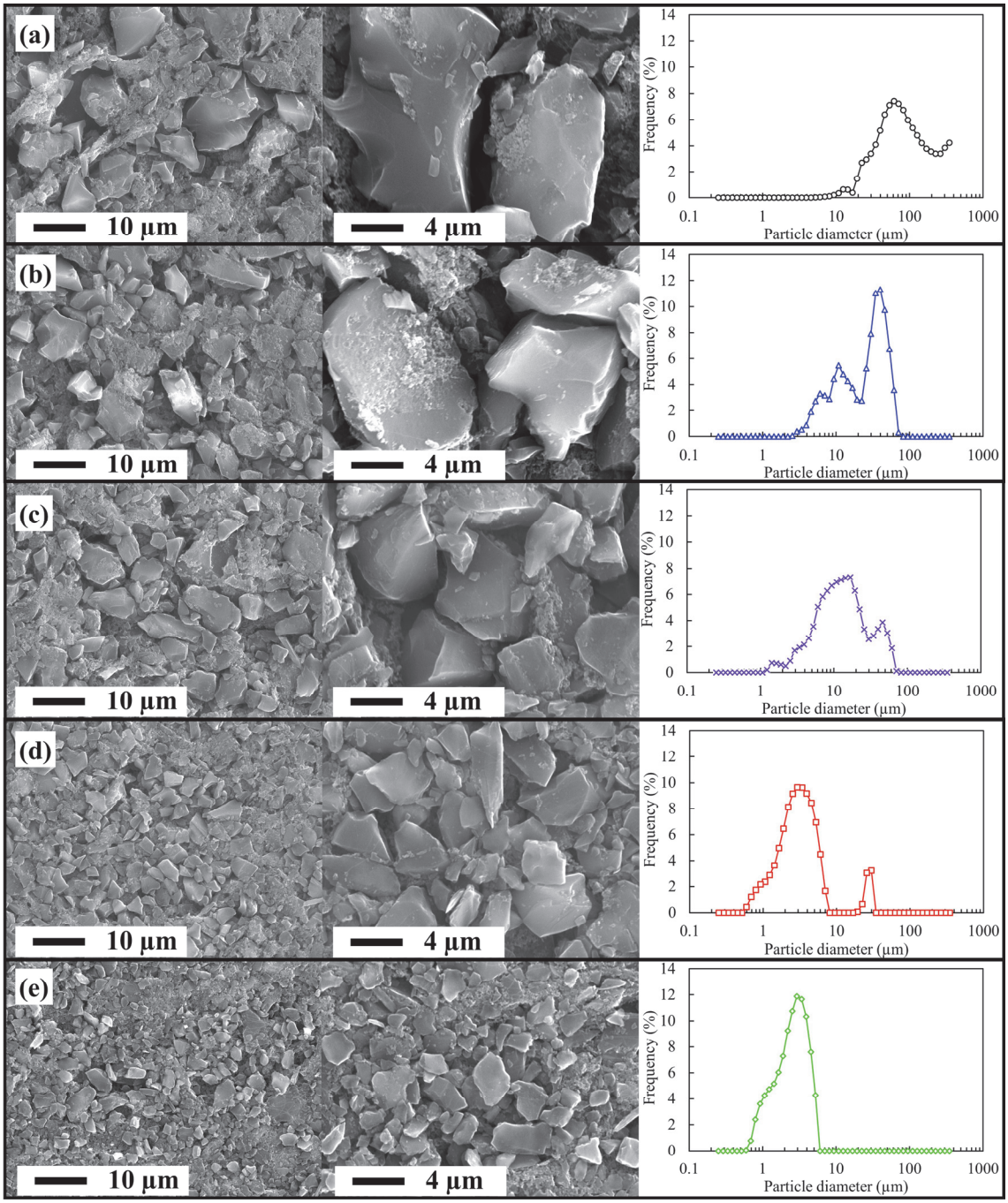

Fig. 3.3. Surface morphology of the EDLC electrodes using the milled ACs, and their particle size distributions. (a) AC0; (b) ACS10; (c) AC10; (d) AC90; (e) AC120.

3.3.2 Electrochemical properties of the milled ACs

Details of the fabricated electrodes used for EDLC cells are shown in **Table 3.4**. The electrodes were ϕ12 mm-disks incorporating the milled ACs of 10−13 mg, and their thickness ranged from 0.29 to 0.32 mm. The bulk density of AC in the electrode was dependent on the milling time. The higher AC bulk density was obtainable from the ACs pulverized for a longer time. Markedly high AC bulk density (0.39 g cm^{-3}) was apparent for the electrode using AC120.

Table 3.4. Details of the fabricated electrodes (ϕ12 mm).

Used AC	Mass of AC in the electrode (mg)	Thickness of the electrode (mm)	AC bulk density in the electrode (g cm^{-3})
AC0	11.7	0.32	0.32
ACS10	10.8	0.30	0.32
AC10	10.6	0.30	0.31
AC90	12.1	0.31	0.34
AC120	12.9	0.29	0.39

Meso- and macroporosity, and interparticle porosity of the prepared EDLC electrodes were evaluated by means of mercury porosimetry. **Figure 3.4** shows pore size distributions of the electrodes using the milled ACs. With decreasing the pore diameter, in other words, with increasing the mercury intrusion pressure, cumulative volume of mercury intruded into the EDLC electrodes increased. All the electrodes allowed a linear increase in the cumulative intruded volume up to ~0.4 cm^3 g^{-1}. Above ~0.4 cm^3 g^{-1}, the cumulative intruded volume steeply increased with decreasing the pore diameter. Judging from the surface morphology of the EDLC electrodes, shown in Fig. 3, the pore diameter corresponding to the end of linear volume increase coincided with the interparticle distance (gap between AC particles), for instance, 1.5 μm for AC10, 0.7 μm for AC90, and 0.3 μm for AC120. Thus, it is reasonable to interpret that the variations in the cumulative intruded volume above 0.4 cm^3 g^{-1} indicates the meso- and macroprosity of the electrodes which were produced within AC particles. It was observed that the electrodes using ACS10 and AC10 allowed greater development of macrpores, while that using AC90 possessed a largest volume of mesopores of 7−50 nm. The electrodes using AC0 and AC120 exhibited poorest macro-and mesoporosity. The electrodes using ACS10 and AC10 had similar meso- and macroporosity, although their average particle sizes had a twofold difference.

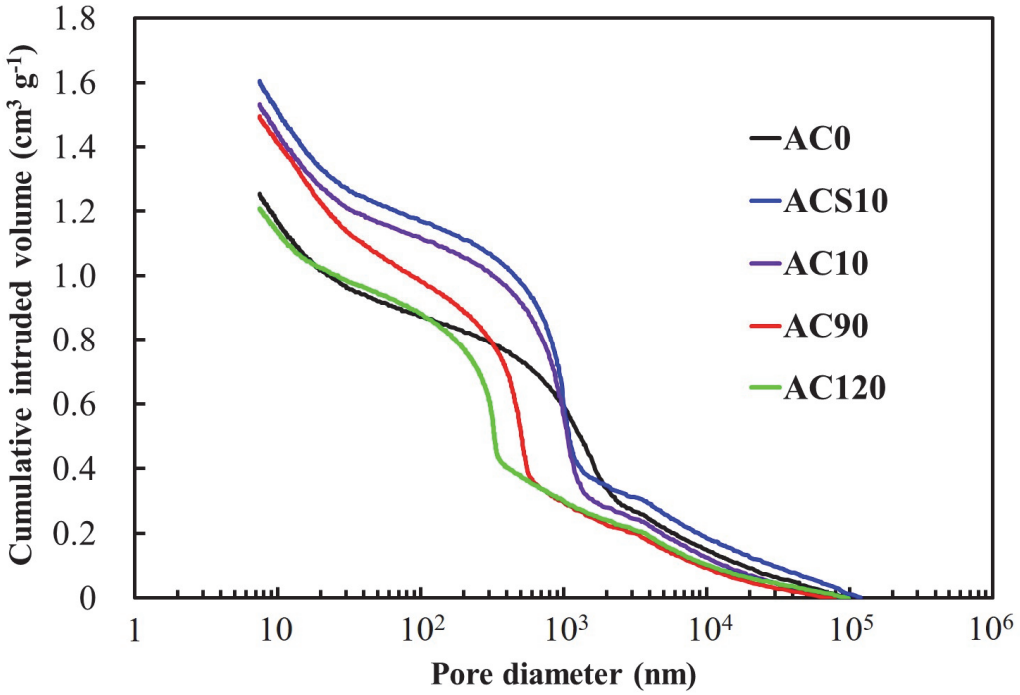

Fig. 3.4. Pore size distributions of the disk EDLC electrodes using the milled ACs, obtained by mercury intrusion porosimety.

The cyclic voltammograms converted from the current response during the CV at the scan rates of 1, 10, and 100 mV s^{-1} are shown in **Fig. 3.5**, providing the specific capacitance at the varying voltage cell. The symmetrical curves appeared in all the ACs at the scan rate of 1 mV s^{-1}, meaning that an electric double layer without a redox reaction was soundly formed on the electrode. At the scan rate of 1 mV s^{-1}, AC0 showed the highest gravimetric specific capacitance, and the gravimetric specific capacitance of the ACs decreased with the milling time. As the voltage scan rate increased, the CV curves allowed a depressive distortion. The curve distortion of AC90 was found to be most suppressed at the scan rates of 10 and 100 mV s^{-1}, indicating that the lowest internal resistance was produced in the AC90 electrode. It should be noticed that, at all the scan rates, the gravimetric specific capacitance of AC120 was lowest in all the ACs. The highest gravimetric specific capacitance did not appear for the non-milled

and the most milled ACs at the increased scan rates, suggesting that the degree of milling had a definite influence on the charge–discharge rate performance of AC.

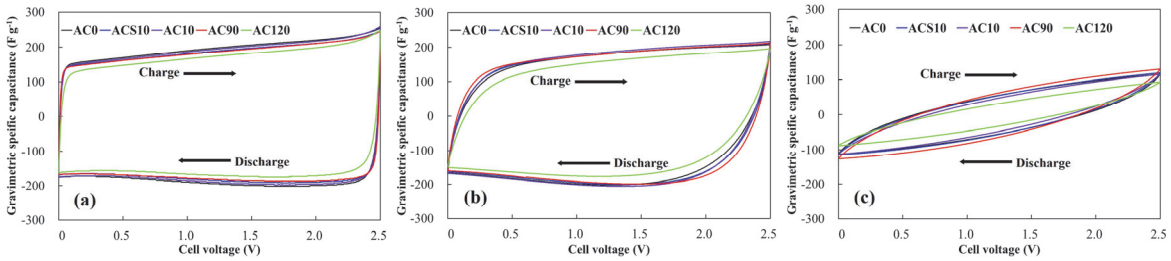

Fig. 3.5. CV curves of EDLC cells using the milled ACs at the scan rates of (a) 1 mV s^{-1}, (b) 10 mV s^{-1}, and (c) 100 mV s^{-1}.

Figure 3.6 shows the specific capacity–cell voltage profiles of the ACs under different current densities during the GCD rate test. The IR drops were observed at the start of charging and discharging. The IR drops appeared distinctly above the current density of >10 mA cm^{-2} in all of the samples. AC120 allowed the largest IR drop, while the other ACs allowed similar levels of IR drops, indicating that noticeable ESR was produced within the AC120 electrode. At the lower current density of <1 mA cm^{-2}, where the IR drop was negligible, a longer milling time led to a decrease in the specific capacity at the end of the discharge process. Representative ESR values of the milled ACs at the switching of charge to discharge during the rate GCD tests were calculated and are shown in **Table 3.5**. ESRs of the milled ACs tended to decrease with the current density. The ESR of AC120 was found to be considerably high, while those of the other ACs were comparable regardless of the current density. The comparable ESR values mean that the charge-storage or charge-release performance of ACs was mainly governed by their dynamics of double-layer formation and release, and was hardly related to the electrolyte, contact and intrinsic resistances.

Table 3.5. Equivalent series resistances (ESRs) of the milled ACs at the switching of charge to discharge during the GCD rate tests. Unit: Ω.

Current density (mA cm^{-2})	AC0	ACS10	AC10	AC90	AC120
0.1	46.4	47.8	46.1	46.7	141.7
1	19.1	15.3	19.6	15.2	108.0
5	16.4	16.2	16.8	12.7	96.8
10	13.8	14.3	14.1	11.9	73.9
50	13.3	14.0	13.7	12.5	NM[1]
100	12.5	13.8	13.5	12.6	NM[1]

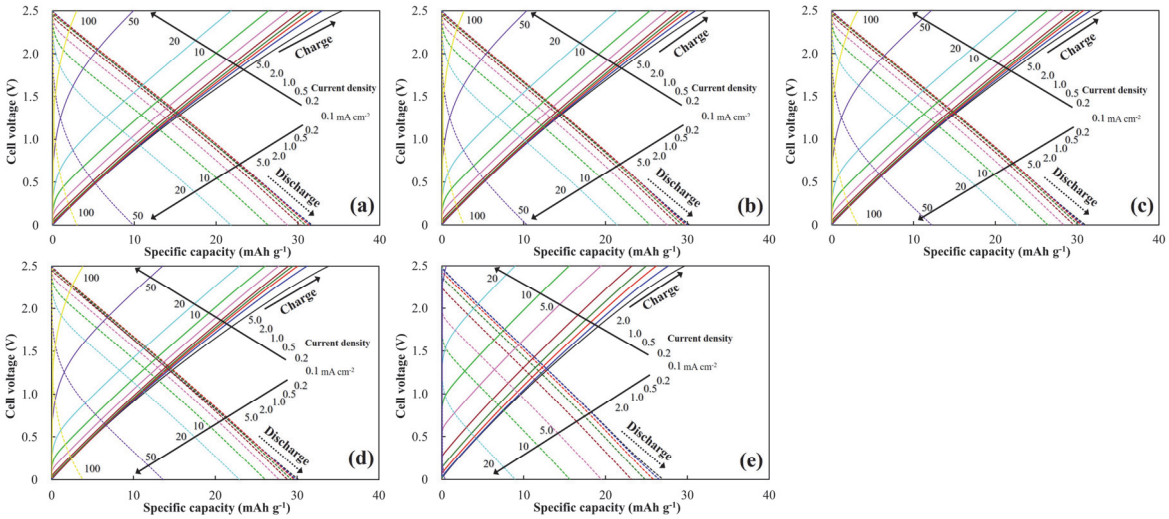

Fig. 3.6. Specific capacity of milled ACs vs. cell voltage in the GCD rate tests at different current densities. The specific capacity is a time-integral of current divided by the total mass of AC active material both in the positive and negative electrode. (a) AC0; (b) ACS10; (c) AC10; (d) AC90; (e) AC120.

The gravimetric and volumetric specific capacitances, and the gravimetric and volumetric Ragone plots for all the ACs are shown in **Fig. 3.7**. The gravimetric specific capacitances of all the ACs were maintained up to the current density of 5 mA cm^{-2}. The non-milled AC (AC0) displayed the highest gravimetric specific capacitance of 183 F g^{-1}, while the AC subjected to the longest milling (AC120) had the lowest value (<160 F g^{-1}). At the higher

current density (>10 mA cm^{-2}), the ACs allowed a decline of the gravimetric specific capacitance, where the degree was dependent on the milling time. AC10 and AC90, which had middle levels of D_{ave}, could retain a high gravimetric specific capacitance. Under very high current density (>20 mA cm^{-2}), the gravimetric specific capacitance of AC120 was measured to be negligible. From the gravimetric Ragone plots, the highest gravimetric energy density of 39.3 Wh kg^{-1} was observed on AC0 at the gravimetric power density of 12.0 W kg^{-1}. Except for AC120, very little difference in gravimetric energy density among the type of ACs was observed at the lower gravimetric power density (< 1000 W kg^{-1}). Under the very high gravimetric power density (>2000 W kg^{-1}), AC90 displayed the highest gravimetric energy density of all the ACs.

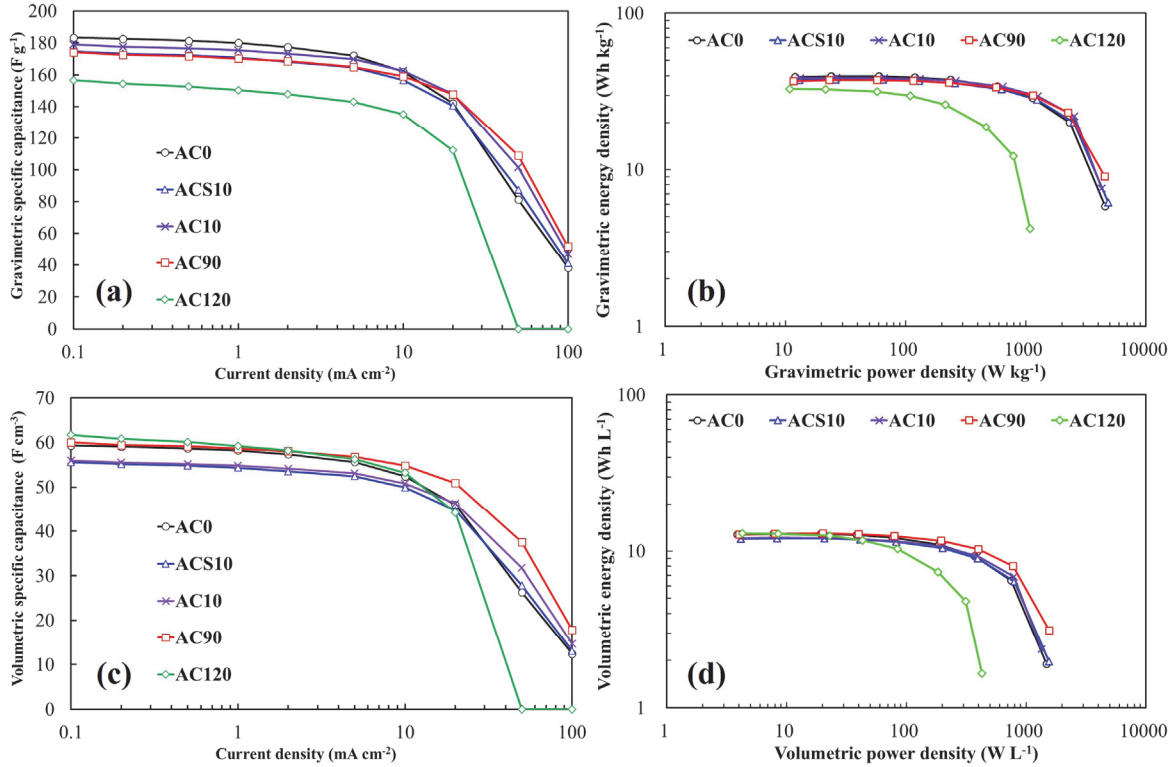

Fig. 3.7. Gravimetric and volumetric specific capacitances of the milled ACs at different current densities, and their Ragone plots. (a) Gravimetric specific capacitance; (b) gravimetric Ragone plot; (c) volumetric specific capacitance; (d) volumetric Ragone plot.

The volumetric specific capacitances of all the ACs were different from the gravimetric ones. At the lower current density (< 10 mA cm^{-2}), AC120 showed the highest volumetric

specific capacitance of 61.7 F cm^{-3}. Sufficiently milled ACs (AC90 and AC120) could also attain a similar level of the high volumetric specific capacitance. However, under the higher current density (>10 mA cm^{-2}), AC0 and AC120 allowed the volumetric specific capacitance to lower. Only AC90 could largely retain the volumetric specific capacitance. The volumetric Ragone plots indicated that all the ACs showed comparable volumetric energy density at the lower volumetric power density (< 100 Wh L^{-1}). Among them, the highest volumetric energy density of 13.0 Wh L^{-1} was observed for AC120 at the volumetric power density of 4.3 W L^{-1}. AC90 had the highest ability to keep the volumetric energy density, even under the higher volumetric power density (>100 W L^{-1}). The appropriate milling process enabled us to enhance the volumetric energy density from 4.9 Wh L^{-1} (AC0) to 6.6 Wh L^{-1} (AC90) even under the high volumetric power density of 1 kW L^{-1}, while the most milled AC (AC120) did not operate at 1 kW L^{-1}. It is true that the differences between the particle properties of AC90 and AC120 were not as large (D_{ave} = 3.0 μm for AC90 and D_{ave} = 2.2 μm for AC120). The results regarding the GCD rate tests revealed that the ball milling process had a large influence on the volumetric performance, rather than on the gravimetric performance. It was also revealed that excessive milling of the AC active material can degrade the high-power performance of the EDLC cell.

Figure 3.8 shows the cyclic stability of the specific capacitance of the milled ACs at the current density of 10 mA cm^{-2} under the cell voltage range of 0−2.5 V. The specific capacitance retentions of AC0, ACS10, AC10, AC90, and AC120 were 96, 93, 96, 95, and 93%, respectively, which guaranteed the initial cycling stability of ACs. Although their long-term stability could not be verified, the effect of the milling process on the cyclic charge–discharge performance was shown to be minor.

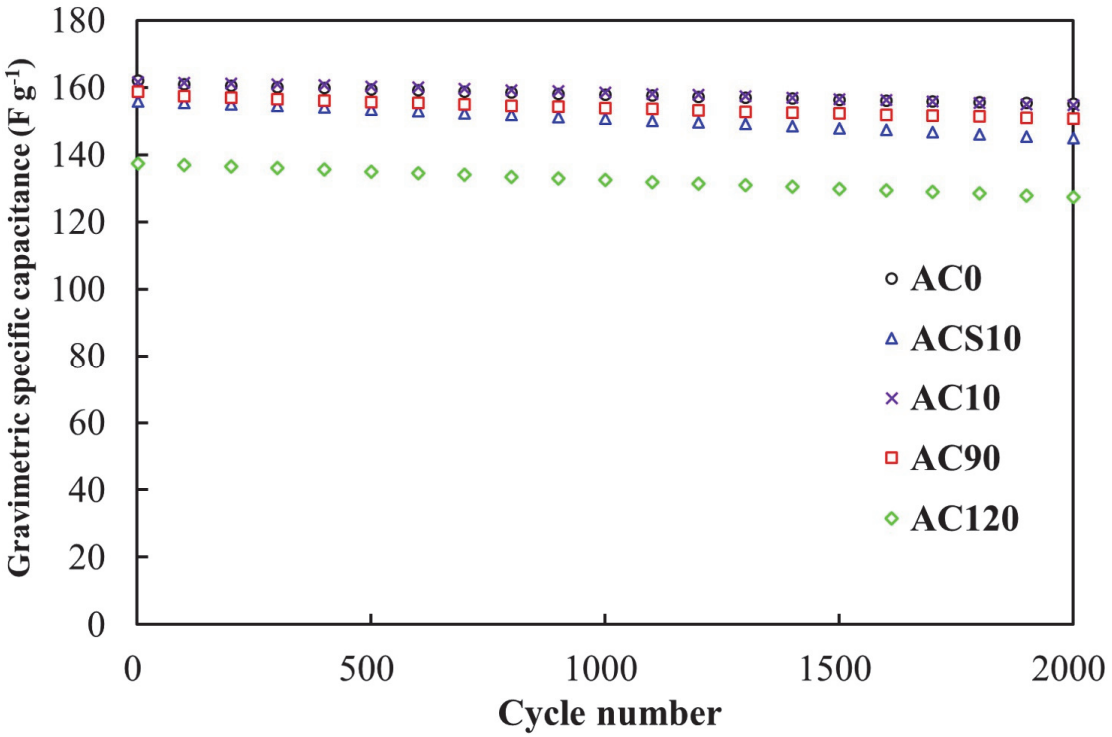

Fig. 3.8. Cyclic stability of the specific capacitance of the milled ACs at the current density of 10 mA cm^{-2} under the cell voltage range of 0–2.5 V.

3.3.3 Material and electrochemical properties of the ACs with different particle sizes

The petroleum coke-based AC with a very high specific surface area (S_{BET}= 3198 m^2 g^{-1}) and with a number of course particles (D_{ave} = 74.9 μm) was pulverized to find its greatest gravimetric or volumetric EDLC performance. The pulverization was executed by means of planetary ball milling under different milling times and different types of zirconia balls. Using five ϕ19.5 mm zirconia balls at a rotation speed of 400 rpm, finely and uniformly pulverized ACs were produced; D_{ave} = 11.6 μm for 10 min (AC10), 3.0 μm for 90 min (AC90), and 2.2 μm for 120 min (AC120). Instead of gaining fine and uniform particles, the AC allowed a decrease in S_{BET} because of the cumulative collisions between the balls and the particles. X-ray diffractometry and Raman spectroscopy revealed that structural changes of the AC hardly occurred during the ball-milling. Despite the difference in D_{ave} between the AC90 and AC120 being slight, AC120 displayed a much lower S_{BET} (2448 m^2 g^{-1}) than did AC90 (2775 m^2 g^{-1}). The pore size distribution analysis verified that pores within the AC degenerated during the

ball-milling. A trade-off between the pulverization and the porosity maintenance was apparent up to the milling time of 90 min. However, this relation was invalid for the longer milling time (120 min). Under the present ball milling mechanism, the pulverization of particles became saturated, while the pore degeneration subsequently proceeded with the milling time.

The performances of milled ACs as the active materials of EDLC electrodes was explored by means of GCD rate tests. AC0 and AC120 exhibited the maximum gravimetric and volumetric specific capacitance, respectively. However, at the higher current density (>10 mA cm^{-2}), both the ACs allowed noticeable decreases in the specific capacitance. The greatest maintenance of both the gravimetric and volumetric specific capacitance, as well as the high volumetric specific capacitance, which was comparable to that of AC120, was observed on AC90. At the high power density of 1 kW L^{-1}, the volumetric energy density of the electrode increased from 4.9 (AC0) to 6.6 Wh L^{-1} (AC90, 35% increment) by the milling process optimization. It was advocated that the smaller size of AC particles was responsible for the decrease in the diffusion resistance of ion-transport within the particles [9]. Even if AC90 allowed the decrease in surface area to form an electric double-layer because of the long-term milling, the electrode densification and the enhanced ion-transportation within the AC pores led to the excellent rate performances. AC120, which was most finely and uniformly pulverized, displayed the poorest rate performances out of all the ACs. The difference in statistic parameters of D_{ave} or D_{50} between AC90 and AC120 was slight. Based on the percolation theory for carbon particles in an insulating media, the particle size can have an influence on the electric conductivity of the composite [27]. However, judging from the slight difference in D_{ave} between AC90 and AC120, and the low fraction of insulating polytetrafluoroethylene binder in the electrode (10 mass%), the greater rate performance of AC90 was not explainable from percolation theory. It was revealed that AC90 included milled fine particles and residual large particles at 20−30 μm, while AC120 comprised only fine particles of <6 μm. The much higher electrode bulk density for AC120 (0.39 g cm^{-3}) was clearly attributed to the more finely and uniformly pulverized particles. For highly filled EDLC electrodes, a wide interparticle gap, which is necessary to assist the impregnation of electrolyte into discrete AC particles, and thus into micro- and mesopores within the ACs [6, 8], was not realized. It was also demonstrated

that the electrode using AC90 attained greatest mesoporosity of 7−50 nm, which could offer fluent ion-transportation connected to the higher rate performance.

The results obtained here indicated that, for ACs with a very high specific surface area (~3000 m^2 g^{-1}), particle pulverization was still effective for enhancing the volumetric EDLC performances and the stability against the high current or power density. However, excessive pulverization can rather degrade the EDLC performances of ACs because of excessive electrode densification, which restricts the ion-transportation within pores. Besides the statistic particle size parameters (D_{ave} or D_{50}), the particle size distribution of AC was also found to be an important factor to determine the EDLC performances.

3.4 Conclusions

The ball milling process was optimized for AC with a very high surface area and course particles, as the active material of EDLC cells using a non-aqueous electrolyte, so as to attain the greatest electrochemical performance. The carbonaceous structure, micro- and mesoporosity, and particle size distribution of the AC were evaluated as a time function of the planetary ball milling. The EDLC electrodes comprising the ACs milled under different conditions were evaluated in the GCD rate and cycle tests, providing their gravimetric and volumetric specific capacitances, Ragone plots, and cyclic charge–discharge stability. Meso- and macroporosity, and interparticle porosity of the EDLC electrodes produced from the milled ACs were also evaluated.

With the development of pulverization, the AC allowed the decrease in S_{BET}, which was closely related to the area of double-layer formation. The AC milled at 400 rpm for 90 min (AC90) allowed a decrease in S_{BET} from 3198 to 2775 m^2 g^{-1}, and thereby a decrease in the gravimetric specific capacitance at the lower current density of <10 mA cm^{-2}. However, it exhibited the greatest maintenance of both the gravimetric and volumetric specific capacitance at the higher current density of >10 mA cm^{-2}. Even at the high volumetric power density of 1 kW L^{-1}, it showed a noticeable volumetric energy density of 6.6 Wh L^{-1}, which was 35% higher than that of the untreated AC. A combination of milled fine particles at <8 μm and residual

large particles at 20−30 μm led to the electrode densification (decreased interparticle gap), and the enhanced ion-transportation within the AC pores.

It was also revealed that excessive pulverization did not enhance either the gravimetric or the volumetric performances of the AC, in particular at the higher power density. A much higher electrode bulk density (0.39 g cm^{-3}) was attained by the AC milled for 120 min (AC120), which comprised only fine particles of <6 μm. However, the lowered micro- and mesoporosity and the excessive electrode densification restricted the ion-transportation within the pores, leading to degradation of the high-power performance. Judging from a minor difference in the particle size parameter (D_{ave} or D_{50}) between AC90 and AC120, the particle size distribution of AC was found to be more important in tuning the EDLC performances of highly porous ACs. It was confirmed that the appropriate pulverization of AC particles had potential to enhance the high-power performance of EDLC cells, both from the gravimetric and volumetric viewpoints.

References

[1] P. Simon, A. Burke, Nanostructured carbons: Double-layer capacitance and more. Electrochem. Soc. Interface 17 (2008) 38–43.

[2] A. Yoshida, S. Nonaka, I. Aoki, A. Nishino, Electric double-layer capacitors with sheet-type polarizable electrodes and application of the capacitors. J. Power Sources 60 (1996) 213–218.

[3] A.G. Pandolfo, G.J. Wilison, T.D. Huynh, A.F. Hollenkamp, The influence of conductive additives and inter-particle voids in carbon EDLC electrodes. Fuel cells 5 (2010) 856–864.

[4] A.J.R. Rennine, V.L. Martins, R.M. Smith, P.J. Hall, Influence of particle size distribution on the performance of ionic liquid-based electrochemical double layer capacitors. Sci. Rep. 6 (2016) 22062.

[5] B, Dyatkin, O. Gogotsi, B. Malinovskiy, Y. Zozulya, P. Simon, Y. Gogotsi, High capacitance of coarse-grained carbide derived carbon electrodes. J. Power Sources 306 (2016) 32–41.

[6] Y. Kado, K. Imoto Y. Soneda, N. Yoshizawa, Correlation between the pore structure and electrode density of MgO-templated carbons for electric double layer capacitor applications. J. Power Sources 305 (2016) 128–133.

[7] P. Azaïs, Manufacturing of industrial supercapacitor. Supercapacitor materials, systems, and applications; Béguin, F., Frackowiak, E.; Wiley-VCH Verlag GmbH & Co. KGaA, Weinheim, Germany, (2013) p. 320.

[8] Y. Kado, Y. Soneda, Void-bearing electrodes with microporous activated carbon for electric double-layer capacitors. J. Electroanal. Chem. 833 (2019) 33–38.

[9] S. Tanaka, H. Nakao, T. Mukai, Y. Katayama, Y. Miyake, An experimental investigation of the ion storage/transfer behavior in an electrical double-layer capacitor by using monodisperse carbon spheres with microporous structure. J. Phys. Chem. C 116 (2012) 26791–26799.

[10] R. Nandhini, P.A. Mini, B. Avinash, S.V. Nair, Subramanian, K.R.V. Supercapacitor electrodes using nanoscale activated carbon from graphite by ball milling. Mater. Lett. 87 (2012) 165–168.

[11] J. Xu, R. Zhang, J. Wang, S. Ge, H. Zhou, Y. Liu, P. Chen, Effective control of the microstructure of carbide-derived carbon by ball-milling the carbide precursor. Carbon 52 (2013) 499–508.

[12] N.J. Welham, V. Berbenni, P.G. Chapman, Increased chemisorption onto activated carbon after ball-milling. Carbon 40 (2002) 2307–2315.

[13] W.S. Choi, W.G. Shim, D.W. Ryu, M.J. Hwang, H. Moon, Effect of ball milling on electrochemical characteristics of walnut shell-based carbon electrodes for EDLCs. Microporous Mesoporous Mater. 155 (2012) 274–280.

[14] B.R. Müller, Effect of particle size and surface area on the adsorption of albumin-bonded bilirubin on activated carbon. Carbon 48 (2010) 3607–3615.

[15] T.S. Ong, H. Yang, Effect of atmosphere on the mechanical milling of natural graphite. Carbon 38 (2000) 2077–2085.

[16] E. Partlan, K. Davis, Y. Ren, O.G. Aqul, O.T. Mefford, T. Karanfil, D.A. Ladner, Effect of bead milling on chemical and physical characteristics of activated carbons pulverized to superfine sizes. Water Res. 89 (2016) 161–170.

[17] A. Macías-García, D. Torrejón-Martín, M.A. Díaz-Díez, J..P. Carrasco-Amador, Study of the influence of particle size of activate carbon for the manufacture of electrodes for supercapacitors. J. Energy Storage 25 (2019) 100829.

[18] C. Portet, G. Yushin, Y. Gogotsi, Effect of carbon particle size on electrochemical performance of EDLC. J. Electrochem. Soc. 155 (2008) 531–536.

[19] G. Katagiri, H. Ishida, A. Ishitani, Raman spectra of graphite edge planes. Carbon 26 (1988) 565–571.

[20] A. Eckmann, A. Felten, A. Mishchenko, L. Britnell, R. Krupke, K.S. Novoselov, C. Casiraghi, Probing the nature of defects in graphene by Raman spectroscopy. Nano Lett. 12 (2012) 3925–3930.

[21] C. Guizani, K. Haddad, L. Limousy, M. Jeguirim, New insights on the structural evolution of biomass char upon pyrolysis as revealed by the Raman spectroscopy and elemental analysis. Carbon 119 (2017) 519–521.

[22] A.V. Neimark, Y. Lin, P.I. Ravikovitch, M. Thommes, Quenched solid density functional theory and pore size analysis of micro-mesoporous carbons. Carbon 47 (2009) 1617–1628.

[23] G.Y. Gor, M. Thommes, K.A. Cychosz, A.V. Neimark, Quenched solid density functional theory method for characterization of mesoporous carbons by nitrogen adsorption. Carbon 50 (2012) 1583–1590.

[24] M.L.C. Piedboeuf, A.F. Léonard, K. Traina, N. Job, Influence of the textural parameters of resorcinol–formaldehyde dry polymers and carbon xerogels on particle sizes upon mechanical milling. Colloids Surf. A: Physicochem. Eng. Aspects 471 (2015) 124–132.

[25] B. Sathyaseelan, E. Manikandan, I. Baskaran, K. Senthilnathan, K. Sivakumar, M.K. Moodley, R. Ladchumananandasivam, M. Maaza, Studies on structural and optical properties of ZrO_2 nanopowder for opto-electronic applications. J. Alloys Compd. 694 (2017) 556–559.

[26] M. Thommes, K. Kaneko, A.V. Neimark, J.P. Olivier, F. Rodriguez-Reinoso, J. Rouquerol K.S.W. Sing, Physisorption of gases, with special reference to the evaluation of surface area and pore size distribution (IUPAC technical report). Pure Appl. Chem. 87 (2015) 1051–1069.

[27] X. Jing, W. Zhao, L. Lan, The effect of particle size on electric conducting percolation threshold in polymer/conducting particle composites. J. Mater. Sci. Lett. 19 (2000) 377–379.

Energy density maximization of LIC using highly porous activated carbon cathode and Si anode

4.1 Introduction

To meet the stringent requirements of growing industries such as next-generation vehicles and renewable power storage, high-performance capacitors possessing energy densities higher than those of LIBs (> 300 Wh kg^{-1}) and power densities similar to those of EDLCs (~10 kW kg^{-1}) must be developed. A lower anode lithiation potential permits a wider voltage window, which increases the energy density of LIC cells [1,2]. A high specific capacity for Li-ion storage and a low anode lithiation potential are required from the anode active material. In recent years, silicon (Si) has emerged as a promising anode active material because of the following advantages: its high theoretical specific capacities of 4200 mAh g^{-1} in the $Li_{4.4}Si$ phase and 3590 mAh g^{-1} in the $Li_{3.75}Si$ phase, which remain stable at room temperature, its low discharge plateau (~0.2 V vs. Li/Li^+), and its earth abundance [3-5]. However, the disadvantages of the Si anode include its drastic volumetric expansion (approximately 280%) during the uptake/release of Li ions [6]. The volumetric expansion deteriorates the cycling performance and decreases the energy and power density of LIBs in which Si is used in the anode [4]. The problem of low cycling stability is gradually being resolved through the use of Si composite materials, Si nanoparticles, and Si oxides (SiO_x) as anodes. It has been reported that LICs in which Si is employed as the anode active material can theoretically accomplish higher energy densities than LICs using conventional carbonaceous anode active materials [7]. The specific capacity of an anode fabricated using carbon-coated Si/SiO_x has been reported to be 1081 mAh g^{-1} at 0.2 A g^{-1}; by using the aforementioned anode, an LIC cell having an energy density of 123 Wh kg^{-1} over the cell voltage range of 1.5−3.9 V has been fabricated [8]. Shao et al. fabricated an LIC cell having an energy density of 213 Wh kg^{-1}, using carbon-capsulated Si having an anodic capacity of 3160 mAh g^{-1} at a mass ratio between the cathode and anode active materials of 4.0, which operated over the cell voltage range of 2.0−4.5 V [9]. Li et al. developed a high-energy-density LIC that delivered an energy density of 254 Wh kg^{-1} (867 W kg^{-1}) over the cell voltage range of 2.0–4.5 V [10]. In this LIC cell, egg-white-derived AC

having a specific surface area of 3250 m^2 g^{-1} and carbon-coated nanosized Si powder were used as the cathode and anode active materials, respectively. The literature survey presented so far indicates that manufacturing LIC cells having energy densities exceeding 300 Wh kg^{-1} necessitates the use of pure Si as the anode active material. To overcome the low cycling stability of pure-Si-based anodes resulting from the large volumetric variation of Si during the uptake and release of Li ions, using thermosetting polyimide binders having excellent mechanical strength [11-13] is a favorable choice.

To fabricate a very-high-energy-density LIC cell, the specific capacity of the cathode needs to be much higher than those in conventional LICs. Microporous AC possesses a high specific surface area and facilitates the formation of wide electric double layers, making it the preferred material for EDLC electrodes. YP50F is a commercially available AC that is employed as the benchmark in EDLC studies [14]. It has a specific surface area of ~1700 m^2 g^{-1} and has abundant micropores. The specific capacity of YP50F is 50 mAh g^{-1} in the potential range of 2.0–4.0 V vs. Li/Li^+, evaluated in a half-cell configuration with the counter electrode being Li metal [15]. ACs having specific surface areas in the range of 2000−3000 m^2 g^{-1} have been produced from various precursors through novel chemical activation techniques [16-20]. ACs having specific surface areas of > 3000 m^2 g^{-1} are commercially available and can be applied as the active material in EDLCs and LICs. An EDLC cell delivering a high energy density of 39.3 Wh kg^{-1}-AC in the cell voltage range of 0−2.5 V was previously fabricated by employing coke-based high-specific-surface-area microporous AC (> 3000 m^2 g^{-1}) and a non-aqueous electrolyte [21].

The cathode capacity in LIC cells can be designed to be lower than the anode capacity to alleviate the aging of the anode and thereby to enhance the cell lifetime [22, 23]. However, to maximize the energy density of LIC cells, the surplus anode capacity should be minimized (or the anode and cathode capacities must be equalized) [24]. It is necessary to optimize not only the mass (or capacity) ratio between the cathode and anode active materials but also the cell voltage range, to equalize the anode and cathode capacities. The cell voltage range determines the potential differences allocated to the cathode and anode during the charge/discharge processes; this indicates that at an optimum cell voltage range, the maximum

energy density can be achieved.

We attempted the development of an LIC cell having a very high energy density of > 300 Wh kg^{-1} using industrially realistic cell systems and materials, which can be deemed as a pioneering attempt in the capacitor research community. Coke-based AC having a specific surface area of > 3000 m^2 g^{-1} was used as the cathode active material and Si powder having a particle size in the range of a few micrometers, combined with a polyimide binder, was employed as the anode active material. Half-cells were assembled to evaluate the Li-ion uptake and release properties of the LIC cathode and anode and identify the relationship between electrode potential and specific capacity. The cell voltage and the cathode/anode potential were measured using a three-electrode full-cell (3E cell), during which the cell voltage was varied to find the upper and lower cut-offs of cell voltage at which the maximum energy density can be achieved. Two-electrode full-cells (2E cells) were assembled as well, and the 2E and 3E cells were subjected to rate and cycle tests to verify the repeatability of the performance of the LIC systems developed. To investigate the chemical and morphological events that occurred during the rate and cycle tests, postmortem electrode analyses were performed through X-ray photoelectron (XP) spectroscopy (XPS) and scanning electron microscopy (SEM). To verify the feasibility of the industrial application, a lifespan-oriented LIC cell was assembled using a lower active mass ratio of cathode to anode and tested over a limited cell voltage range.

4.2 Material and methods

4.2.1 AC cathode and Si anode preparation

MAXSORB (Kansai Coke and Chemicals Co., Ltd., Amagasaki, Japan) was chosen as the highly porous AC active material for the LIC cathode. MAXSORB was synthesized from petroleum coke by means of KOH activation [25]. Thereafter, it was pulverized using a planetary ball mill (P-6, Fritch Japan Co., Ltd., Yokohama, Japan) operating at a rotational speed of 400 rpm for 10 min and employing a zirconia bowl having an 80 mL milling-space and zirconia balls of 19.5 mm diameter as the size-reduction agents. Si powder (Silgrain e-Si, Elkem ASA, Norway) was used as-received as the anode active material of the LIC cells. A gas adsorption analyzer (Autosorb-3B, Quantachrome Instruments Inc., USA) was employed to

acquire the nitrogen gas adsorption-desorption isotherms of the AC and Si powders at −196 ℃. Prior to acquiring the isotherms, ~30 mg of the powdered samples was degassed in vacuum at 200 ℃ for > 8 h. The Brunauer–Emmett–Teller (BET) theory was applied to calculate the specific surface area (S_{BET}) of the AC and Si samples using the adsorption isotherms at the relative pressures of 0.05–0.10 and 0.10–0.30, respectively. The volume of nitrogen adsorbed at the relative pressure of 0.99 was considered to be the total pore volume (V_{total}) of the sample. The pore-size distribution of the AC was calculated based on the quenched solid density functional theory (QSDFT) [26, 27] using an accessory software (ASiQwin, version 1.11, Quantachrome Instruments Inc., USA) to obtain the volumes of the micropores (V_{micro}) and mesopores (V_{meso}). The particle sizes of the AC and Si powders were determined using a laser diffraction particle size analyzer (SALD-200V, Shimadzu Corp., Kyoto, Japan). The average particle diameter and the cumulative 25%, 50% (median value), and 75% particle diameters, which were denoted as D_{ave}, D_{25}, D_{50}, and D_{75}, respectively, were measured.

To fabricate the cathode, 80% (w/w) AC, 10% (w/w) acetylene black (AB: Denka Black, Denka Co., Ltd., Japan) as a conductive agent, and 5% (w/w) sodium carboxymethyl cellulose (Cellogen 7A, DKS Co., Ltd., Japan) and 5% (w/w) styrene-butadiene rubber (TRD2001, JSR Corp., Japan), both as binders, were mixed in distilled water using a planetary centrifugal mixer (AR-100, Thinky Corp., Japan). The resulting slurry was coated onto an aluminum foil (t20 μm) using an applicator. To fabricate the anode, 80% (w/w) Si, 5% (w/w) AB, and 15% (w/w) polyimide binder (DREAMBOND 100, I.S.T, Corp., Japan) were thoroughly mixed in *N*-methylpyrrolidone (Tokyo Chemical Industry Co., Ltd., Japan) as a solvent. Using an applicator, the prepared slurry was coated onto Cu foil (t20 μm). Following the drying of the coated Al and Cu foils at 100 ℃ in the air over > 8 h, they were perpendicularly pressed at 2 MPa and punched out into disks of 15 mm diameter. The disk-shaped cathodes and anodes were heated under vacuum for > 5 h at 140 and 200 ℃, respectively. These electrodes were transferred into a glove box (GBJF080R, Glovebox Japan Inc., Japan) without exposing them to air.

4.2.2 Half-cell, 2E cell, and 3E cell assembly and electrochemical measurements

The half- and full-cells used in this study were integrated using 2E cells made of SUS304 stainless steel (HS Flat cell, Hosen Corp., Japan) and 3E cells made of SUS304 stainless steel (HS 3-electrode cell, Hosen Corp., Japan). The 3E cell had a structure in which a reference electrode was incorporated into the 2E cell (**Fig. 4.1**). All cells were assembled inside a glove box filled with Ar gas. The electrolyte used was $LiPF_6$ dispersed in ethylene carbonate/diethyl carbonate 50/50% (v/v) at the concentration of 1 M (Kishida Chemical Co., Ltd., Japan). A porous polypropylene sheet (ϕ23 mm, *t*25 µm, Celgard 2500, Celgard LLC, USA) was used as the separator.

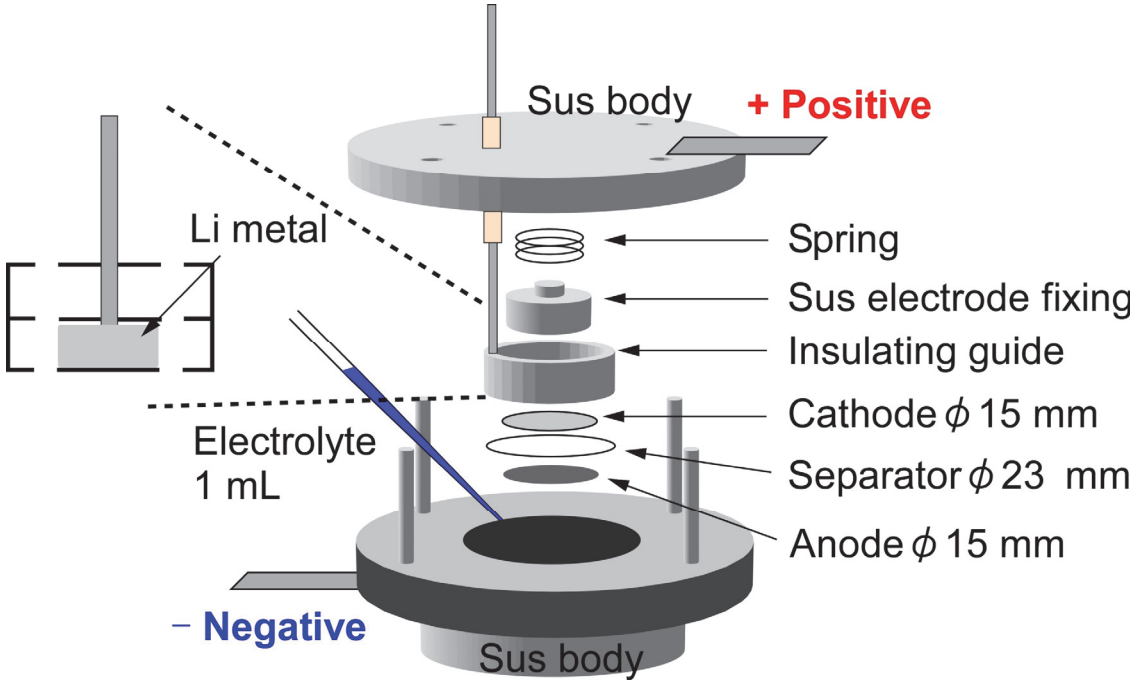

Fig. 4.1. Structure of the 3E cell used.

The half-cells were assembled to evaluate the Li-ion uptake and release properties of the anodes and cathodes used for LIC cells. The electrodes were dipped in the electrolyte for 1 h in the glove box prior to assembling the half-cells. The half-cells were fabricated using AC or Si electrode (hereinafter referred to as the AC half-cell and Si half-cell, respectively), and a counter electrode made of Li foil (ϕ15 mm, *t*200 µm, Honjo Metal Co., Ltd., Japan). To evaluate the individual performance of the AC or Si electrode, a rate test was carried out under galvanostatic current control using a battery charge–discharge system (HJ1005SD8, Hokuto

Denko Corp., Japan). The rate test for the AC electrode was performed over the potential range of 2.0−4.0 V vs. Li/Li^+ at the current densities of 0.05−50 mA cm^{-2}. Using the tested cell, the rate test was performed over the extended potential range of 1.5−4.2 V vs. Li/Li^+. A rate test over the further extended potential range of 1.0−4.4 V vs. Li/Li^+ was performed. The details of the parameters used for the rate tests for the AC electrode are shown in **Table 4.1**. Rate tests for the Si electrode were carried out over the potential range of 0−1.0 V vs. Li/Li^+ at the current densities of 0.1, 1.0, and 10 mA cm^{-2}. The initial Li-ion insertion was carried out over a potential decline from ~3 to 0 V vs. Li/Li^+. The specific capacity of the AC or Si electrode, evaluated in half-cell configuration, was evaluated as the time-integral of the current (charge) divided by the mass of the coated AC or Si.

Table 4.1. Detailed test parameters for the rate-performance evaluation of the AC half-cell.

Sequence	Current density (mA cm^{-2})	Number of cycles	Cycle selected to plot the potential–specific capacity profiles
1	0.05	3	Second
2	0.1	5	Third
3	0.2	5	Third
4	0.5	10	Fifth
5	1.0	10	Fifth
6	2.0	25	Thirteenth
7	5.0	50	Twenty-fifth
8	10	100	Fiftieth
9	20	100	Fiftieth
10	50	100	Fiftieth

Thereafter, the 3E cell was assembled. In the half-cell configuration, the potential of the AC cathode was increased and decreased unidirectionally in the potential range of 2.0−4.0 V vs. Li/Li^+ for five times each at the current densities of 0.1, 1.0, and 10 mA cm^{-2}, to confirm the formation of a stable double layer showing a linear potential variation with the specific capacity. As the final pretreatment, the potential of the AC cathode was increased to 4.0 V vs. Li/Li^+ and decreased to 3.0 V vs. Li/Li^+ at the current density of 0.1 mA cm^{-2}. Anode pre-

lithiation is an essential process in the production of LICs [15, 24]. Pre-lithiation prevents the Li ions in the electrolyte from being consumed to form the SEI layer, thereby improving the initial CE and cycling stability. To pre-lithiate the anode, Li-ion insertion and extraction were performed over 0−1.0 V vs. Li/Li^+ at the current density of 0.1 mA cm^{-2}. Li ions were inserted into the anode until the potential decreased to 0 V vs. Li/Li^+. The half-cells were disassembled in the glove box and the pretreated AC cathode and Si anode were transferred into the 3E cell. The assembled 3E cell was subjected to charge–discharge cycling over the following cell voltage ranges for three cycles each: 2.0−4.0, 1.9−4.1, 1.8−4.2, 1.5−4.3, and 1.0−4.3 V at the current density of 0.1 mA cm^{-2}. Subsequently, the rate test was conducted over the cell voltage ranges of 1.0−4.3 V and 0.7−4.3 V. **Table 4.2** lists the details of the rate test conducted on the 3E cell. The cell voltage–specific capacity profiles were observed during specific selected cycles. In the following step, a cycle test was performed at the current density of 1.0 mA cm^{-2} over the cell voltage range of 1.0−4.3 V. The specific capacity, energy density, and power density of the 3E cell were evaluated as follows. The relation between the specific capacity and the cell performance was calculated based on the total mass of the active materials in the cathode (AC) and the anode (Si). The cathode and anode specific capacities, presented with their potential variations, were calculated from the masses of the cathode and anode active materials, respectively. The energy density (E (Wh kg^{-1})) and power density (P (W kg^{-1})) were calculated using Eq. 4.1 and 4.2.

$$E\,(\mathrm{Wh\,kg^{-1}}) = \frac{1000W}{m_t}, \tag{4.1}$$

$$P\,(\mathrm{Wkg^{-1}}) = \frac{1000V_{ave}I}{m_t}, \tag{4.2}$$

where m_t (g) is the total mass of the cathode and anode active materials, W (Wh) is the energy released during the discharging process, and V_{ave} (V) is the average cell voltage during the discharging process. Ragone plots were drawn from the average values of energy and power density at each current density to derive the relationship between the energy and power densities.

Table 4.2. Detailed test parameters for the rate-performance evaluation of the full-cells.

Sequence	Current density (mA cm^{-2})	Number of cycles	Cycle selected to display the potential–specific capacity profiles
1	0.05	2	Second
2	0.1	2	Second
3	0.2	2	Second
4	0.5	3	Third
5	1.0	3	Third
6	2.0	5	Fifth
7	5.0	5	Fifth
8	10	10	Tenth
9	20	10	Tenth
10	50	10	Tenth

To evaluate the LIC full-cell performance over various cell voltage ranges, rate and cycle tests were conducted using the 2E cells. To pre-lithiate the Si anode used in the 2E cells, the half-cell was assembled and Li ions were inserted into the Si anode until the potential decreased to 0 V vs. Li/Li^+ at 0.1 mA cm^{-2}. Thereafter, Li ions equivalent to a specific capacity of 400 mAh g^{-1} were extracted from the Si anode to produce a capacity margin for accepting Li ions during the charging process. The half-cell used for the pre-lithiation of the Si anode was disassembled in the glove box. The AC cathode used for 2E cells was simply immersed in the electrolyte for 1 h and subjected to no electrochemical pretreatments. Subsequently, the pre-lithiated Si anode and the electrolyte-permeated AC cathode were transferred to the 2E cell in the glove box. Five 2E cells were assembled. Rate and cycle tests were conducted for the 2E cells over the cell voltage ranges of 1.0−4.3, 2.0−4.0, 1.5−4.0, and 1.5−4.2 V.

The effect of equalizing the cathode and anode capacities on LIC performance was investigated for different cell voltage ranges and active material mass ratios. Hereinafter, cells are designated using the style of nomenclature aE-v_1–v_2V, where "a" is the number of electrodes in the full-cell, and "v_1" and "v_2" are the lower and upper cut-offs of the cell voltage range, respectively. The nomenclature can be expanded with -C/A-r, where "r" is the cathode:anode active mass ratio. **Table 4.3** summarizes the active masses of the cathode and the anode as well

as their ratio for each of the assembled cells. The cathode and anode active masses were in the ranges of 3.46−5.56 and 0.87−1.05 mg, respectively. The active mass ratio of the cathode to the anode varied from 3.30 to 6.37. The cycle test was performed at the current density of 1.0 mA cm^{-2}, during which the rate test was intermittently performed using a procedure similar to the one employed for the 3E cells prior to the cycle test and every 1000 cycles. The specific capacity, energy density, and power density of the 2E cells were calculated using criteria similar to those used for the 3E cell. All measurements and analyses were conducted at 25 ℃.

Table 4.3. Cathode and anode active material masses and their ratios as set for the test cells.

Cell ID	Cell voltage range (V)	Mass of cathode active material (mg)	Mass of anode active material (mg)	Cathode:anode active mass ratio
AC half-cell	2.0–4.0, 1.5–4.2, 1.0–4.4	5.52	—	—
Si half-cell	0–1.0	—	0.87	—
3E-1.0–4.3V (three-electrode full-cell)	2.0–4.0, 1.9–4.1, 1.8–4.2, 1.5–4.3, 1.0–4.3, 0.7–4.3	5.54	0.87	6.37
2E-1.0–4.3V (two-electrode full-cell)	1.0–4.3	5.56	0.93	5.98
2E-2.0–4.0V (three-electrode full-cell)	2.0–4.0	5.36	0.94	5.70
2E-1.5–4.0V (two-electrode full-cell)	1.5–4.0	5.26	1.03	5.16
2E-1.5–4.2V (two-electrode full-cell)	1.5–4.2	5.20	1.02	5.10
2E-2.0–4.0V-C/A-3 (two-electrode full-cell)	2.0–4.0	3.46	1.05	3.30

4.2.3 Postmortem electrode analyses

Following the completion of the rate and cycle tests, the 2E-1.5–4.2V cell was completely discharged and disassembled inside the glove box. The extracted electrodes were soaked in a DEC solution (Wako Pure Chemical Corp., Japan) for 1 d to remove residual ions. Following the extraction of the electrodes from the solution, the electrolytic solution adhering to the electrode was removed using a non-woven fabric and vacuum-dried at room temperature for 1 d. These electrodes were designated as the aged cathode and anode. The unused electrodes were designated as the pristine cathode and anode. The surface morphology and composition of these four types of electrodes were analyzed through XPS and SEM. The XP spectra were recorded on an AXIS Ultra DLD spectroscope (Kratos Analytical Ltd., UK) using monochromatic Al Kα radiation (135 W) in wide- and narrow-scan modes. The scan area was 0.3 mm × 0.7 mm. Initially, the wide-scan spectra were obtained at a pass energy of 160 eV in the binding energy range of 1200–0 eV, and the atomic compositions of the electrode surfaces were calculated from the spectra. Thereafter, the narrow scan was performed, and the spectra in the narrow binding energy range were recorded at the pass energy of 20 eV. The electrode surface was sputtered by an ion gun using argon gas. The etching rate of sputtering for a 20 nm-thick deposit of SiO_2 on Si wafer (Geller MicroAnalytical Laboratory Inc., USA) was 0.2 nm s^{-1}. During the transfer of the sample from the glove box to the XPS system, it was exposed to the atmosphere for 50 s. Therefore, the electrode surface was sputtered for 10 s to remove the layer that was exposed to air. Finally, the surface morphology of the electrodes was observed using an SEM (VE-8800, Keyence Corp., Japan) system without depositing a conduction layer. During the transfer of the samples from the XPS to the SEM system, they were exposed to the atmosphere for 3 min.

4.3 Results and discussion

4.3.1 Performances of cathode- and anode-active materials

The morphological properties of AC and Si used in the LIC cells were evaluated and are listed in **Table 4.4**, wherein their S_{BET} values were calculated from the measured adsorption isotherms shown in **Fig. 4.2**. The S_{BET} of AC was measured to be 3041 $m^2\ g^{-1}$, and the sample was confirmed to include abundant micropores by referring to its pore distribution shown in

Fig. 4.3. The V_{micro} of AC accounted for 71% of its V_{total}. The sizes of the AC particles were mainly distributed in the range of 6.8–19.7 µm. The D_{ave} and D_{50} indicated that the particle size of AC was ~12 µm. The S_{BET} and V_{total} of Si were 5 m^2 g^{-1} and 0.03 cm^3 g^{-1}, respectively, indicating that Si did not undergo a significant increase in its porosity. The particle size of Si was distributed in the range of 1–3 µm, and the D_{ave} and D_{50} of Si were 1.8 and 2.0 µm, respectively.

Table 4.4. Morphological properties of the AC and Si used.

Sample	D_{ave} (µm)	D_{25} (µm)	D_{50} (µm)	D_{75} (µm)	S_{BET} (m^2 g^{-1})	V_{total} (cm^3 g^{-1})	V_{micro} (cm^3 g^{-1})	V_{meso} (cm^3 g^{-1})
AC	11.6	6.8	11.7	19.7	3041	1.72	1.22	0.37
Si	1.8	1.2	2.0	2.9	5	0.03	—	—

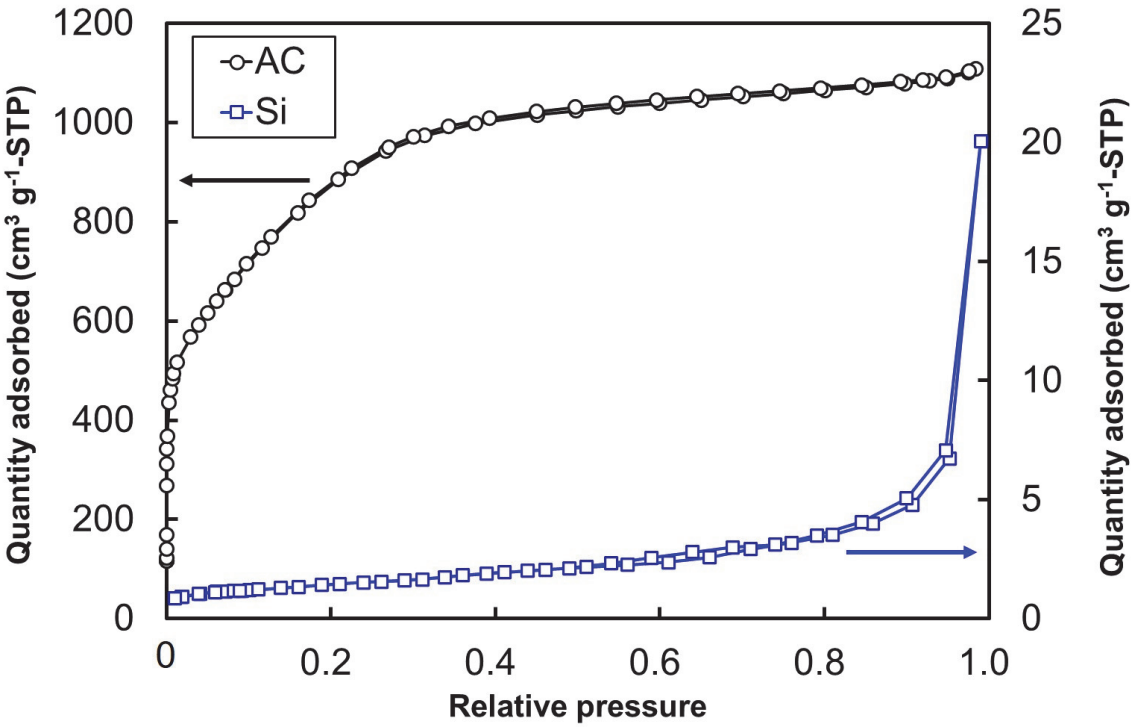

Fig. 4.2. Nitrogen adsorption/desorption isotherms of AC and Si at −196 °C.

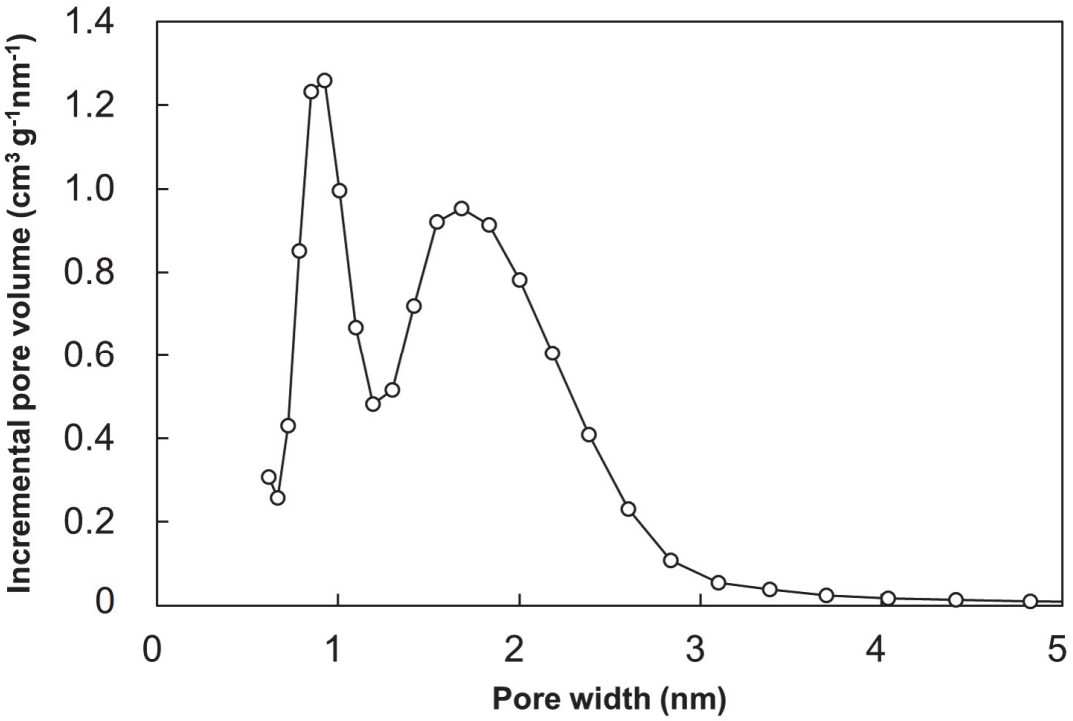

Fig. 4.3. QSDFT pore-size distribution of AC.

The Li-ion uptake and release properties of the AC electrode were evaluated by increasing the current density stepwise. The potential–specific capacity profiles of the AC electrode at different potential ranges were evaluated using a half-cell (**Fig. 4.4**), and its discharge specific capacity is shown in **Fig. 4.5** as a function of the number of cycles. The AC electrode permitted cycles of potential elevation (charge) and descent (discharge) at different current densities. At low current densities (< 5 mA cm^{-2}), the discharge specific capacity increased with the extension of the potential range. At high current densities (> 10 mA cm^{-2}), the change in the discharge specific capacity caused by the extension of the potential range was smaller than that at low current densities. The highest discharge specific capacities in the potential rages of 2.0–4.0, 1.5–4.2, and 1.0–4.4 V vs. Li/Li^+ were 116, 200, and 333 mAh g^{-1}, respectively, measured at the lowest current density of 50 μA cm^{-2} (equal to 16 mA g^{-1}-AC). The extension of the potential range increased the discharge specific capacity and induced a change in the charge/discharge profile from an ideal triangle to a distorted shape. At current densities of > 5 mA cm^{-2}, potential range extension had a marginal effect on the discharge specific capacity. A potential drop caused by the internal resistance of the cell (IR drop) was clearly observed on all charge/discharge profiles upon switching from the charging to

discharging processes. Furthermore, intermittent potential drops were observed on the profiles, likely caused by the lower current-response (dendrite formation) of the Li metal counter electrode. The IR drop hinders the increase in specific capacity at higher current rates. The distorted curve obtained in the potential range of 1.0–4.4 V vs. Li/Li^+ suggests that a Faradaic reaction occurred at < 1.5 V and > 4.2 V vs. Li/Li^+. Faradaic reactions can induce the irreversible decomposition of the electrolyte or chemical reactions on and within the AC particles, which must be avoided in LIC cathodes. Therefore, the maximum usable potential range of the AC electrode was determined to be 1.5–4.2 V vs. Li/Li^+. **Table 4.5** shows a comparison between the reported specific capacities of ACs used in LIC cathodes and the discharge specific capacity of the present AC, suggesting that the present AC possesses a very high specific capacity as an LIC cathode.

Table 4.5. Specific capacities of cathode active materials in half-cell configuration reported in the literature.

Active material	Cathode specific capacity ($mAh\ g^{-1}$)	Potential range (V vs. Li/Li^+)	Current density ($mA\ g^{-1}$)	Ref.
AC (YP-50F, Kuraray Chemical Corp.)	40	3.0–4.5	50	[48]
Porous spherical carbon ($S_{BET} = 1014\ m^2\ g^{-1}$)	65	2.0–4.5	800	[49]
Biomass-derived AC ($S_{BET} = 3011\ m^2\ g^{-1}$)	124	2.0–4.5	300	[50]
Biomass-derived AC ($S_{BET} = 3250\ m^2\ g^{-1}$)	128	2.0–4.5	400	[10]
Coke-based AC	200	1.5–4.2	16	This study

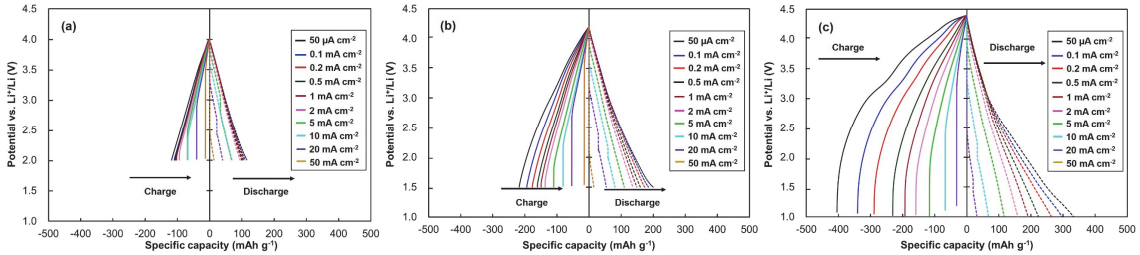

Fig. 4.4. Potential–specific capacity profiles of the AC electrode at different potential ranges during the rate test. The potential ranges were (a) 2.0−4.0, (b) 1.5−4.2, and (c) 1.0−4.4 V vs. Li/Li^+.

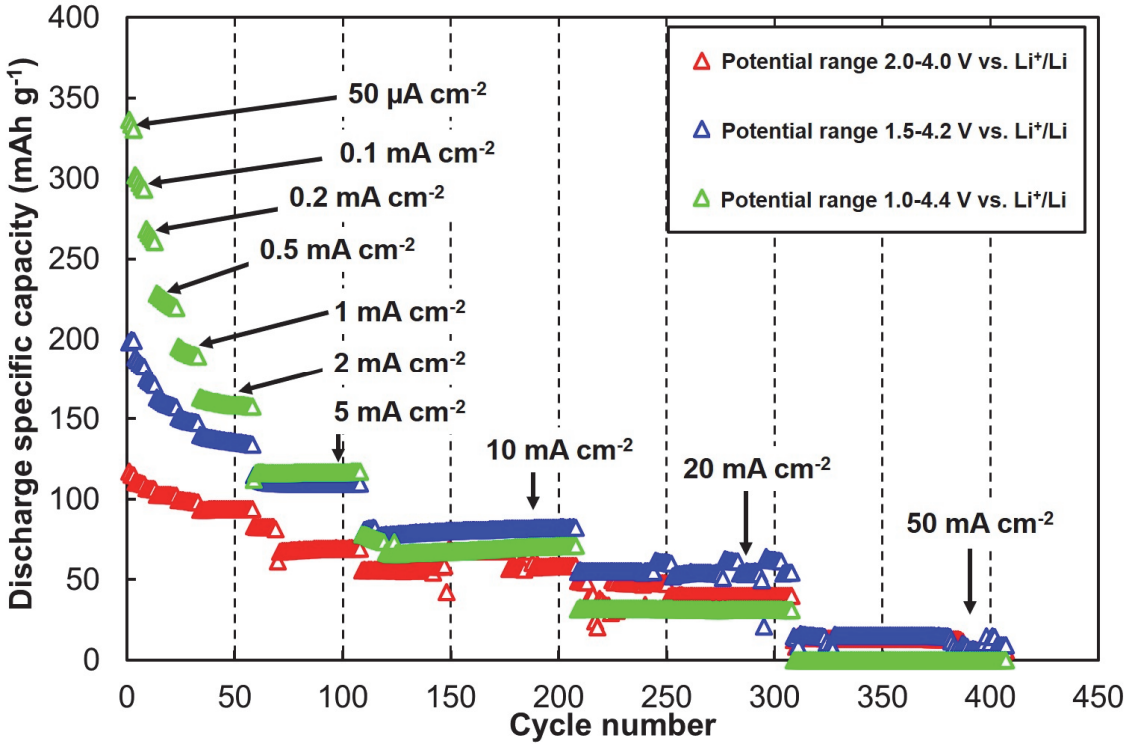

Fig. 4.5. Discharge specific capacity of the AC electrode at different potential ranges, tested in half-cell configuration.

Li-ion insertion (potential descent) and extraction (potential elevation) profiles of the Si electrode at different current densities are plotted in **Fig. 4.6**. The Coulombic efficiency (CE) was measured to be 73.6% over the first cycle at the current density of 0.1 mA cm^{-2}, and it increased following the second cycle up to 96.8% over the fourth cycle. The low CE in the first cycle is due to the irreversible capacity associated with the formation of a solid electrolyte interphase (SEI) film. The high CE exhibited in the later cycles indicates that a reversible Li-

ion insertion/extraction process was established. The average specific capacity for Li-ion extraction in the range of 0–1.0 V vs. Li/Li^+ at 0.1, 1.0, and 10 mA cm^{-2} over four cycles were 2225, 1620, and 107 mAh g^{-1}, respectively. In the steady process at the lowest current density (0.1 mA cm^{-1}), the Si electrode potential during the Li-ion extraction increased to 0.3 V vs. Li/Li^+ immediately and displayed a plateau at 0.44 V vs. Li/Li^+. The plateau was maintained throughout the specific capacity range of 300–1500 mAh g^{-1}. At the moderate current density of 1 mA cm^{-2}, the potential during Li-ion extraction exhibited a gentle gradient and underwent a sharp increase at > 0.65 V vs. Li/Li^+. At the highest current density of 10 mA cm^{-2}, the discharge specific capacity of the Si electrode was considerably reduced.

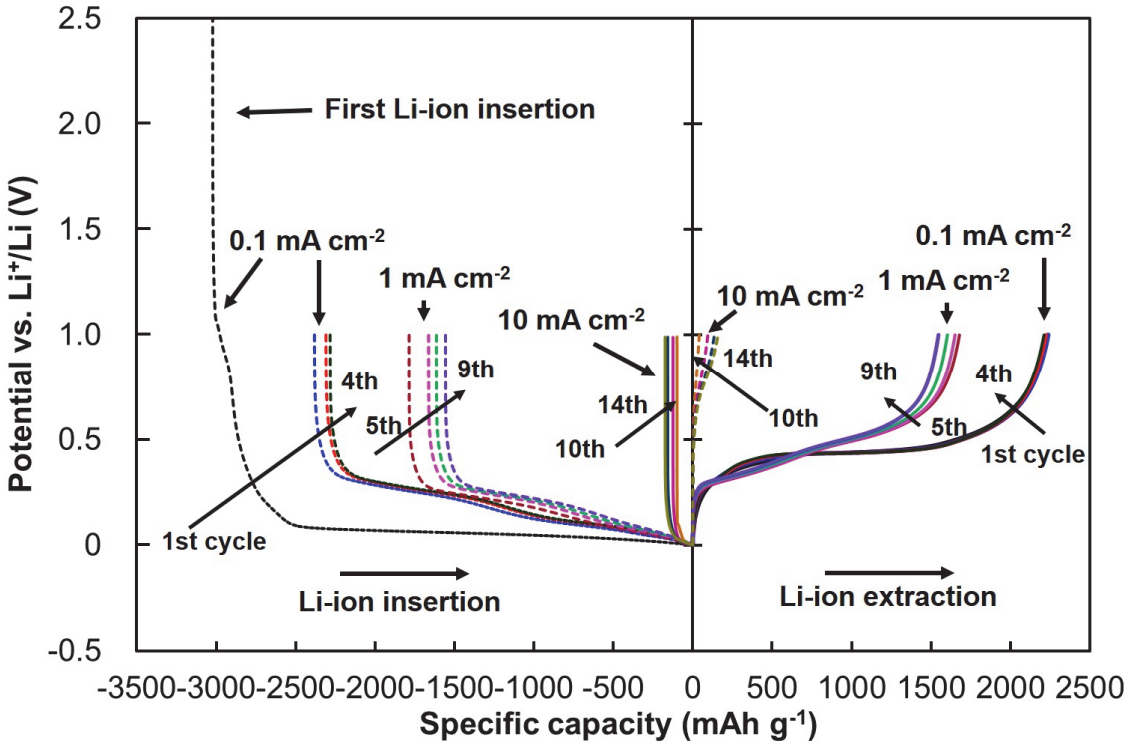

Fig. 4.6. Potential–specific capacity profiles of the Si electrode during the Li-ion insertion and extraction cycles.

4.3.2 Performance evaluation of LIC 3E cells and comparison with 2E cells

The LIC 3E cells fabricated using the AC and Si active materials were charged and discharged over different cell voltage ranges for three cycles. During the second charge/discharge cycle, the cell voltage and each electrode potential were measured as a

function of the specific capacity. **Figure 4.7**a shows the relationship between the cell voltage and the specific capacity for the 3E cell when operated in different cell voltage ranges. The specific capacities of the 3E and 2E cells were calculated by dividing the cell capacity by the total mass of the cathode and anode active materials. All charge/discharge profiles exhibited nearly triangular shapes. However, the shapes were somewhat distorted at the commencement of charging. The discharge specific capacity of the 3E cell was 170 mAh g^{-1} over the largest cell voltage range of 1.0–4.3 V. **Figure 4.7**b shows the variations in the cathode and anode potentials over the different cell voltage ranges. Upon extending the cell voltage range, the maximum cathode and anode specific capacities for the charge as well as discharge processes increased. When the cell voltage was extended from 2.0–4.0 V to 1.0–4.3 V, the cathode and anode specific capacities spent for discharging increased from 84 to 197 mAh g^{-1} and from 523 to 1253 mAh g^{-1}, respectively. The cathode potential profile over the cell voltage range of 1.0–4.3 V was similar to that of the AC electrode over the potential range of 1.5–4.2 V vs. Li/Li^+ (**Fig. 4.4**b), implying that the AC cathode functioned consistently in the LIC cell. The specific capacity required to maintain the discharge plateau of the Si electrode was revealed to be < 1500 mAh g^{-1} (**Fig. 4.6**). Therefore, the cell voltage profiles over all the cell voltage ranges displayed linearity during the discharge process. It was further demonstrated that the distortion of the cell voltage profile observed at the commencement of charging was attributable to the potential descent of the Si cathode upon switching from the Li-ion release process to the uptake process. When the cell was fully charged (upon the completion of charging), the anode potentials were approximately 0 vs. Li/Li^+, indicating that the anode could incorporate the majority of the Li ions. This is favorable for LIC cells because the cathode performance is limited at higher potentials, where irreversible Faradaic reactions are induced. The relationships between the energy density and power density (Ragone plot) of the 3E cell over different cell voltage ranges are depicted in **Fig. 4.7**c. The energy density increased with the cell voltage range, with the maximum energy density of 390 Wh kg^{-1} (at the power density of 63 W kg^{-1}) being attained over the widest cell voltage range of 1.0–4.3 V. This was an increase of 190 Wh kg^{-1} over that observed over the cell voltage range of 2.0–4.0 V. Extending the cell voltage range was effective in increasing the energy density, owing to the decrease in the surplus anode

capacity resulting from the increase in the cathode capacity and the complete utilization of the anode discharge plateau region.

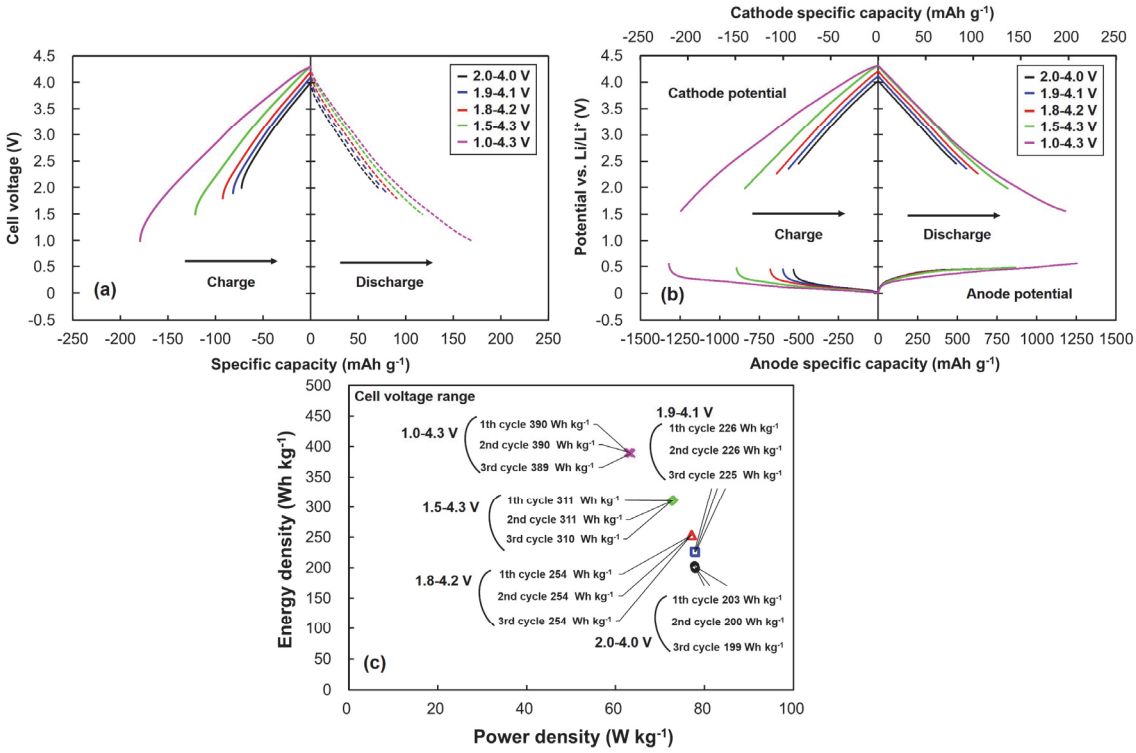

Fig. 4.7. Charge/discharge performance of the three-electrode LIC cell at the current density of 0.1 mA cm^{-2} over different cell voltage ranges. (a) Cell voltage–specific capacity profiles. (b) Potential variations of the cathode and anode, and (c) the relationship between energy density and power density (Ragone plot).

Following the aforementioned rate tests, the 3E cell was evaluated through a rate test over the cell voltage range of 1.0–4.3 V. Subsequently, it was subjected to an additional rate test over the further extended cell voltage range of 0.7–4.3 V. In addition to this, the 2E cell which had not been subjected to any tests so far was subjected to the rate test in the cell voltage range of 1.0–4.3 V. The discharge specific capacities of the 3E and 2E cells under stepwise increases of current density are shown in **Fig. 4.8**a. All cells underwent a decrease in their discharge specific capacities with increasing current density. The specific capacity of 3E-0.7–4.3V was not higher than that of 3E-1.0–4.3V at any current density, proving that extending the

cell voltage range by decreasing the lower cut-off cell voltage below 1.0 V does not increase the specific capacity of the LIC cell. A comparison between the 3E and 2E cells indicated that although marginally higher specific capacities were attained by 2E-1.0–4.3V at higher rates, repeatable test results were obtained. The maximum discharge specific capacities of 3E-1.0–4.3V, 3E-0.7–4.3V, and 2E-1.0–4.3V were 201, 191, and 205 mAh g^{-1}, respectively, at the lowest current density of 50 μA cm^{-2}. Li ions are more abundant in the electrolyte of the 3E cell than in that of the 2E cell because of the presence of Li metal as the reference electrode, which was probably connected to the lower performance of the 2E cell. **Figure 4.8**b shows the Ragone plots based on the aforementioned rate tests. The maximum energy densities for 3E-1.0–4.3V, 3E-0.7–4.3V, and 2E-1.0–4.3V were 400 Wh kg^{-1} at the power density of 32 W kg^{-1}, 372 Wh kg^{-1} at 31 W kg^{-1}, and 386 Wh kg^{-1} at 30 W kg^{-1}, respectively, which were all measured at the lowest current density. The 3E cell operating in the cell voltage range of 1.0–4.3 V possessed the maximum energy density of 400 Wh kg^{-1} and excellent rate stability, delivering 200 Wh kg^{-1} at 6 kW kg^{-1}. The extension of the cell voltage range did not necessarily increase the energy density of the LIC cells. **Figures 4.8**c, d, and e show the relationships between the cell voltage and the cell specific capacity for the 3E and 2E cells. The charge and discharge profiles for 3E-1.0–4.3V and 2E-1.0–4.3V possessed similar shapes at all current densities. The IR drops observed upon switching from discharging to charging or vice versa increased as the current density increased. The charge/discharge profile of 3E-0.7–4.3V indicated that the cell voltage at < 1.0 V increased immediately with the specific capacity. Lowering the cut-off cell voltage to 0.7 V did not increase the specific capacity. At current densities of < 5 mA cm^{-2}, lower CEs for the charge and discharge capacities were observed across all the cells. **Figures 4.8**f and g show the variations in the cathode and anode potentials of 3E-1.0–4.3V and 3E-0.7–4.3V, respectively. They displayed similar cathode potential profiles. The IR drops of the cell voltages were chiefly attributed to the steep elevation and descent of the Si anode potential. At the lowest current density of 50 μA cm^{-2}, the highest potentials of the anodes for 3E-1.0–4.3V and 3E-0.7–4.3V following Li-ion extraction were 0.57 V vs. Li/Li^+ at 1256 mAh g^{-1} and 0.93 V vs. Li/Li^+ at 1191 mAh g^{-1}, respectively. The extension of the cell voltage range was responsible for enhancing the potential difference

allocated to the Si anode. However, the allocated potential difference did not enhance the uptake or release of Li ions.

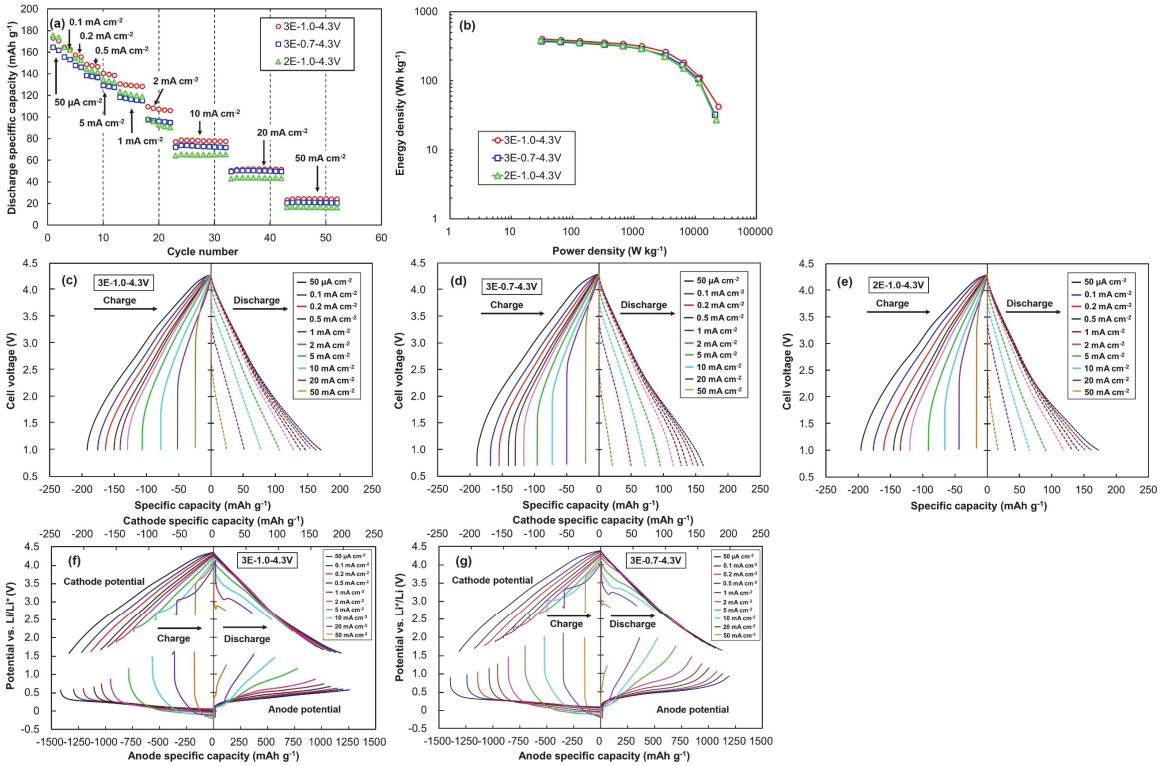

Fig. 4.8. Charge/discharge performance of the three- and two-electrode full-cells during the rate test. (a) Discharge specific capacities of the cells at different current densities; (b) Ragone plots; cell voltage–specific capacity profiles of the (c) three-electrode cell over the cell voltage range of 1.0–4.3 V, (d) three-electrode cell over the cell voltage range of 0.7–4.3 V, and (e) two-electrode full-cell over the cell voltage range of 1.0–4.3 V. Potential variations of the anode and cathode for the three-electrode cell over the cell voltage range of (f) 1.0–4.3 V and (g) 0.7–4.3 V.

The specific capacities and CEs of the 3E and 2E cells measured during the cycle test are shown in **Figs. 4.9**a and d. The cell voltage range was 1.0–4.3 V and the current density was 1 mA cm^{-2}. The 3E-1.0–4.3V cell was initially subjected to rate tests over the cell voltage range of 1.0–4.3 V and subsequently over the range of 0.7–4.3 V. 2E-1.0–4.3V was initially subjected to rate tests over the cell voltage range of 1.0–4.3 V. Repeatable results for the cycle test were

obtained from the 3E and 2E cells. The charge and discharge specific capacities of the 3E and 2E cells decreased as the cycle number increased, while the CE was maintained at approximately 100%. The energy densities of both the cells through the initial cycles were approximately 300 Wh kg^{-1}. However, the 3E and 2E cells retained only 20.1% and 14.8% of their energy densities, respectively, following 1000 cycles. **Figures 4.9**b, c, and e show the relationship between the cell voltage, electrode potential, and specific capacity for these cells during the cycle test. The IR drops for both the cells observed at the commencement of charging and discharging increased with the cycle number, implying that the decrease in the specific capacity was caused by the evolution of internal resistance. The cathode and anode potentials for the 3E cell suggested that the increased IR drop was largely attributable to the abrupt potential variations of the Si cathode. The nearly linear variations of the AC cathode potential indicated that aging-induced on or within the Si anode was the cause of the low cycling performance of the 3E and 2E cells.

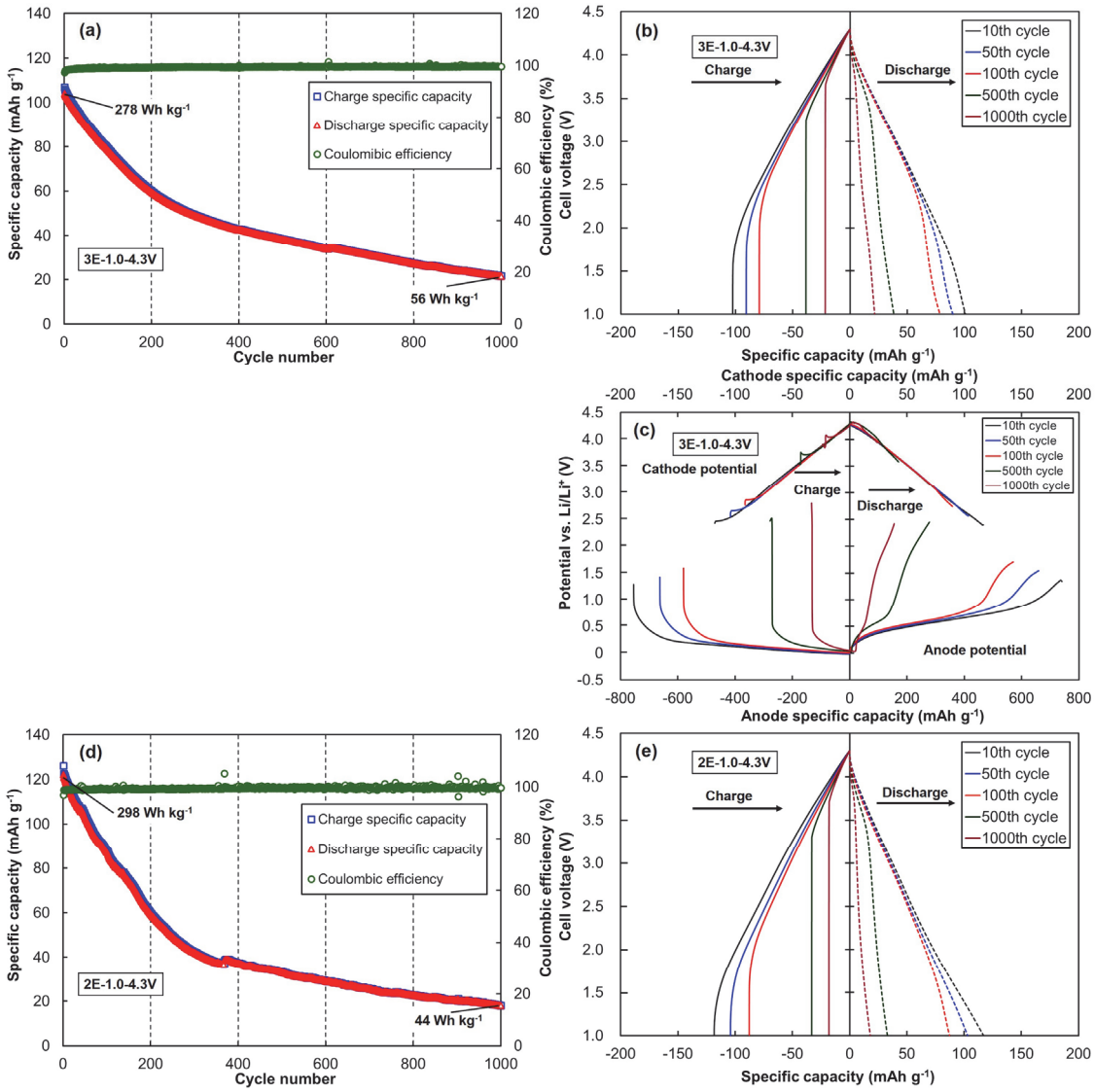

Fig. 4.9. Cycling performances of the 3E and 2E LIC full-cells at the current density of 1.0 mA cm^{-2}. (a) Charge and discharge specific capacities and the Coulombic efficiency, (b) cell voltage–specific capacity profiles, and (c) potential variations of the cathode and anode of the three-electrode cell during the cycle test in the cell voltage range of 1.0–4.3 V; (d) charge and discharge specific capacities and Coulombic efficiencies, and (e) cell voltage–specific capacity profiles of the two-electrode cell during the cycle test in the cell voltage range of 1.0–4.3 V.

4.3.3 Cycling performance of 2E cells

Cycle tests were performed for the 2E cells over different cell voltage ranges. A 2E cell having an active mass ratio of (cathode to anode active mass ratio) of ~5.3 and another

having a lower ratio of 3.30 (2E-2.0–4.0V-C/A-3) were evaluated to investigate the effects of the cell voltage range and the active mass ratio on the cycle lives of LIC cells. The rate tests were intermittently performed during the cycle test. The charge and discharge specific capacities and CEs of the 2E cells during the cycle test at the current density of 1 mA cm^{-2} are shown in **Figs. 4.10**a, c, e, and g. The initial specific capacity and energy density of the cells increased with the extension of the cell voltage range. The discharge specific capacities of 2E-2.0–4.0V, 2E-1.5–4.0V, and 2E-1.5–4.2V decreased significantly, with all the retentions following 2000 cycles being < 20%, whereas the CEs were maintained at approximately 100%. Decreasing the lower cut-off cell voltage from 2.0 to 1.5 V shortened the initial stable stage from ~650 cycles to ~400 cycles. Furthermore, increasing the upper cut-off cell voltage from 4.0 to 4.2 V removed the initial stable stage and expedited the decline of the discharge specific capacity. The initial energy density of 2E-2.0–4.0V-C/A-3 was the lowest among the 2E cells. However, it retained the greatest fraction of its cycle life. 88.6% of its initial energy density was retained at the end of 2000 cycles of charge/discharge. A comparison between 2E-2.0–4.0V and 2E-2.0–4.0V-C/A-3 indicated that, although their initial energy densities were comparable (195 and 176 Wh kg^{-1}, respectively), the active mass ratio (of cathode to anode) had a decisive influence on their cycling performance. The higher mass ratio increased the utilized capacity of the anode. The lower mass ratio restricted the specific capacity of the Si anode dedicated to the uptake and release of Li ions, implying that the potential swings during the charge/discharge processes proceeded in the sufficiently lithiated Si anode. The specific capacity of the AC electrode in the potential range of 2.0–4.0 V vs. Li/Li^+ at the current density of 1 mA cm^{-2} was ~100 mAh g^{-1} (**Fig. 4.4**a). The active mass ratio of 3.30 indicates that the specific capacity of the Si anode used for the potential swings is ~330 mAh g^{-1}. This value is approximately 22% of the Li-ion extraction specific capacity of the Si electrode at 0–1.0 V vs. Li/Li^+ and 1 mA cm^{-2} (~1500 mAh g^{-1}, as shown in Fig. **4.6**). The active mass ratio of ~5.3 further enhanced the specific capacity of the Si anode used for the potential swings to ~530 mAh g^{-1}, suggesting that ~400 mAh g^{-1} may be a threshold for retaining the cycling performance. **Figures 4.10**b, d, f, and h show the relationships between the cell voltage and the specific capacity during the cycle test for the 2E cells. The charge/discharge profiles of 2E-2.0–4.0V, 2E-1.5–4.0V, and 2E-1.5–

4.2V exhibited a tendency similar to that observed in the results of the cycle test for the 3E cell. The linear increase in the cell voltage and the IR drops that were observed upon switching between charging and discharging increased with the cycle number. In contrast to the AC cathode, the Si anode underwent a significant performance deterioration through the cycles of Li-ion uptake and release. The charge/discharge profiles of 2E-2.0–4.0V-C/A-3 did not vary significantly.

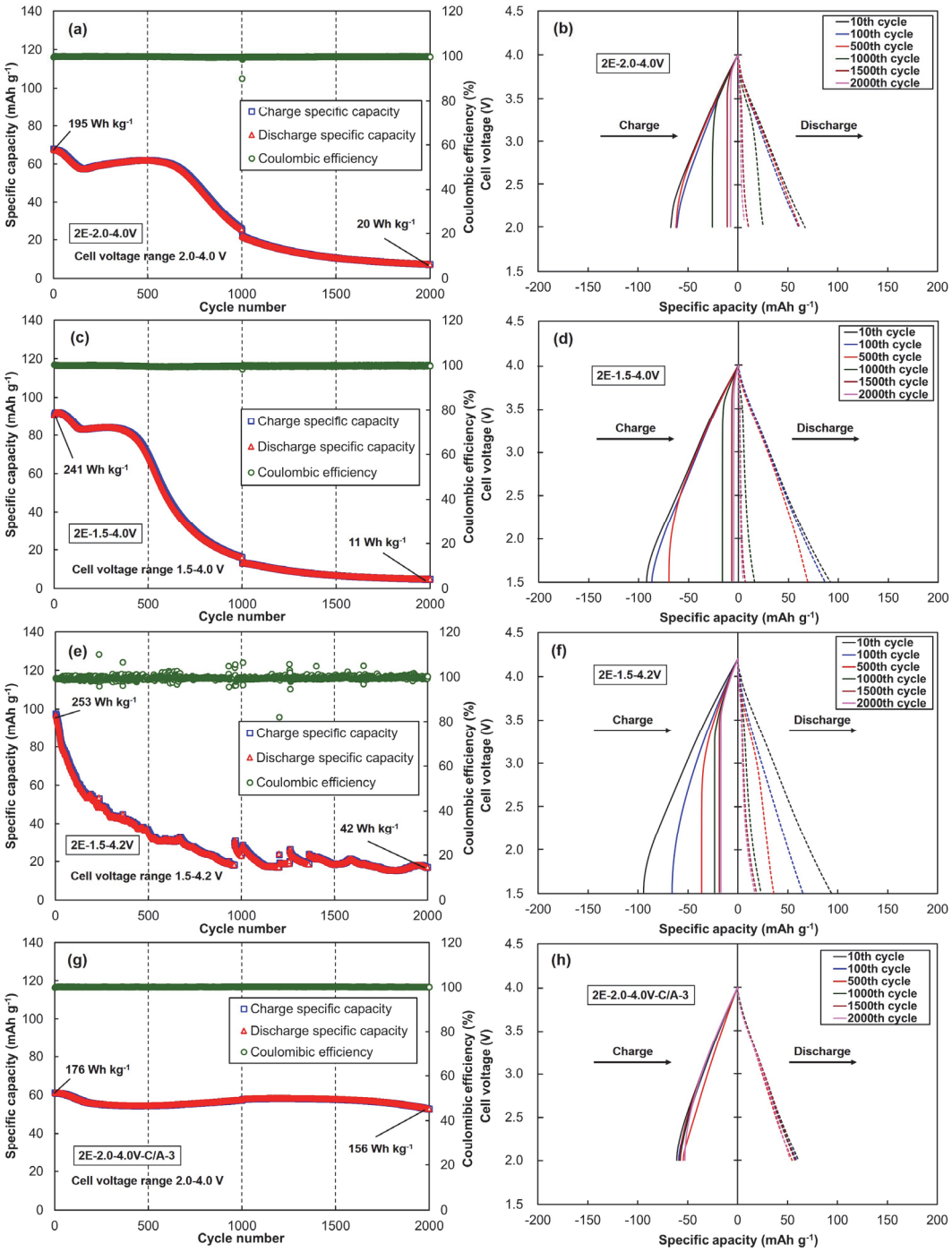

Fig. 4.10. Cycling performance of the 2E LIC full-cells over different cell voltage ranges at the current density of 1 mA cm^{-2}. (a) Charge and discharge specific capacities and Coulombic efficiency, and (b) cell voltage–specific capacity profiles over the cell voltage range of 2.0–4.0 V. (c) Charge and discharge specific capacities and Coulombic efficiencies, and (d) cell voltage–specific capacity profiles over the cell voltage range of 1.5–4.0 V. (e) Charge and discharge specific capacities and CE, and (f) cell voltage–specific capacity profiles over the cell voltage range of 1.5–4.2 V. (g) Charge and discharge specific capacities and CE, and (h) cell voltage–specific capacity profiles at the low cathode:anode active mass ratio of 3.30 over the cell voltage range of 2.0–4.0 V.

The rate performances of the four aforementioned types of 2E cells were evaluated by increasing the current density stepwise. **Figure 4.11** shows their Ragone plots during the cycle tests, which were obtained from the results of the intermittent rate tests. The discharge specific capacities and the cell-voltage–specific-capacity profiles of the 2E cells at the different current densities are shown in **Figs. 4.12** and **4.13**, respectively. Prior to cycling, the maximum energy densities of 2E-2.0–4.0V, 2E-1.5–4.0V, and 2E-1.5–4.2 V were 239 Wh kg^{-1} at 42 W kg^{-1}, 270 Wh kg^{-1} at 35 W kg^{-1}, and 306 Wh kg^{-1} at 37 W kg^{-1}, respectively, measured at the lowest current density (50 μA cm^{-2}). Their energy densities were sustained at higher power densities as well. Prior to cycling, 2E-1.5–4.0V and 2E-1.5–4.2V exhibited the energy density of 100 Wh kg^{-1} even at power densities higher than 10 kW kg^{-1}. Following repeated charge/discharge cycling, they underwent a decrease in their energy density and available power density. Their maximum energy densities decreased to ~100 Wh kg^{-1} and their power density could not be maintained at above 1 kW kg^{-1}, which was clearly due to the aging of the Si anode resulting in the loss of capacity spent for the Li-ion insertion/extraction and the increased internal resistance causing larger IR drops. In contrast, the maximum energy density of the uncycled 2E-2.0–4.0V-C/A-3 was 183 Wh kg^{-1} at 57 W kg^{-1}. It maintained an energy density of 100 Wh kg^{-1} at power densities exceeding 10 kW kg^{-1} regardless of the cycle number.

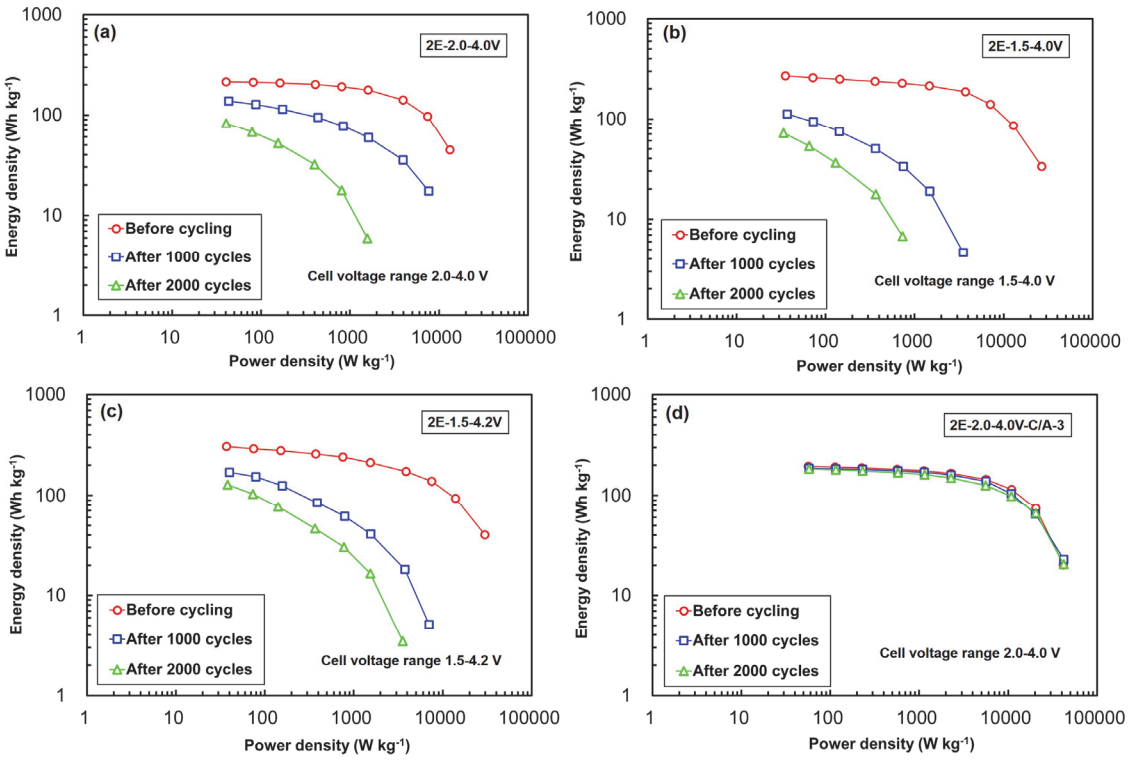

Fig. 4.11. Ragone plots for the 2E full-cells cycled in different cell voltage ranges, plotted during the cycle test at the current density of 1 mA cm^{-2}. The 2E full-cell cycled over the cell voltage ranges of (a) 2.0–4.0 V, (b) 1.5–4.0 V, and (c) 1.5–4.2 V. (d) The 2E full-cell having a low cathode:anode active mass ratio of 3.30 cycled over the cell voltage range of 2.0–4.0 V.

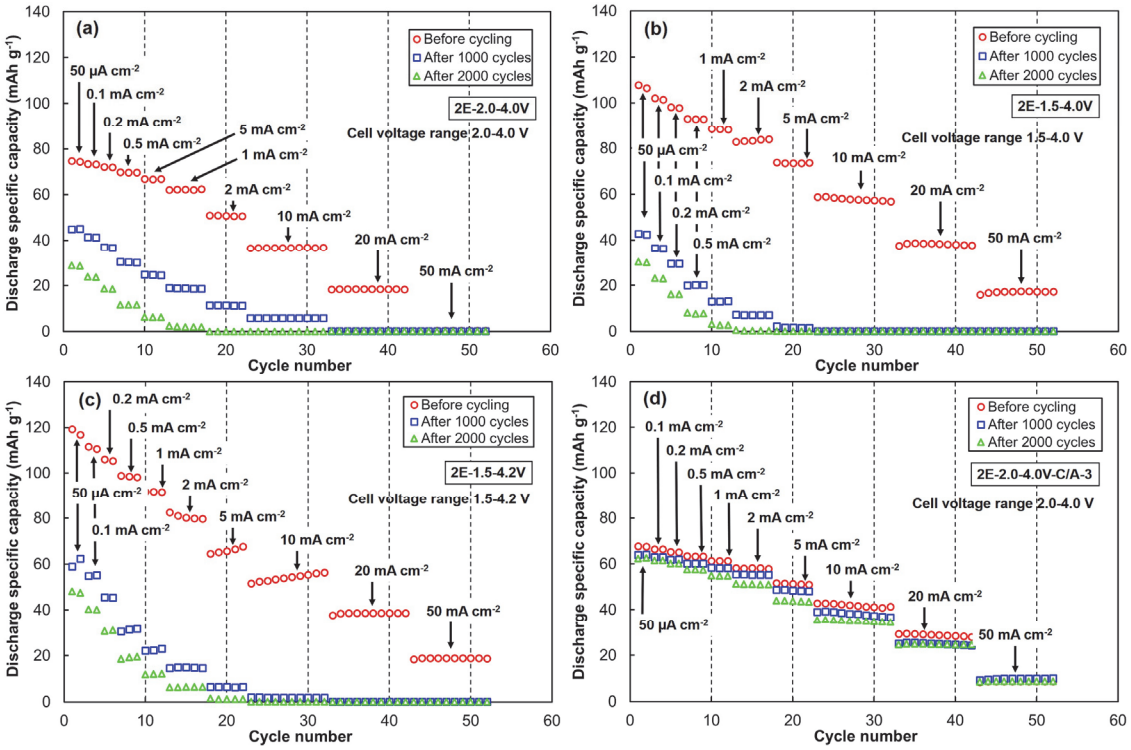

Fig. 4.12. Discharge specific capacity of the 2E full-cells over different cell voltage ranges, plotted during the cycle test at the current density of 1 mA cm^{-2}. The discharge specific capacities of the 2E full-cell over the cell voltage range of (a) 2.0–4.0 V, (b) 1.5–4.0 V, and (c) 1.5–4.2 V, (d) the discharge specific capacities of the 2E full-cell having a low cathode:anode active mass ratio of 3.30 when cycled over the cell voltage range of 2.0–4.0 V.

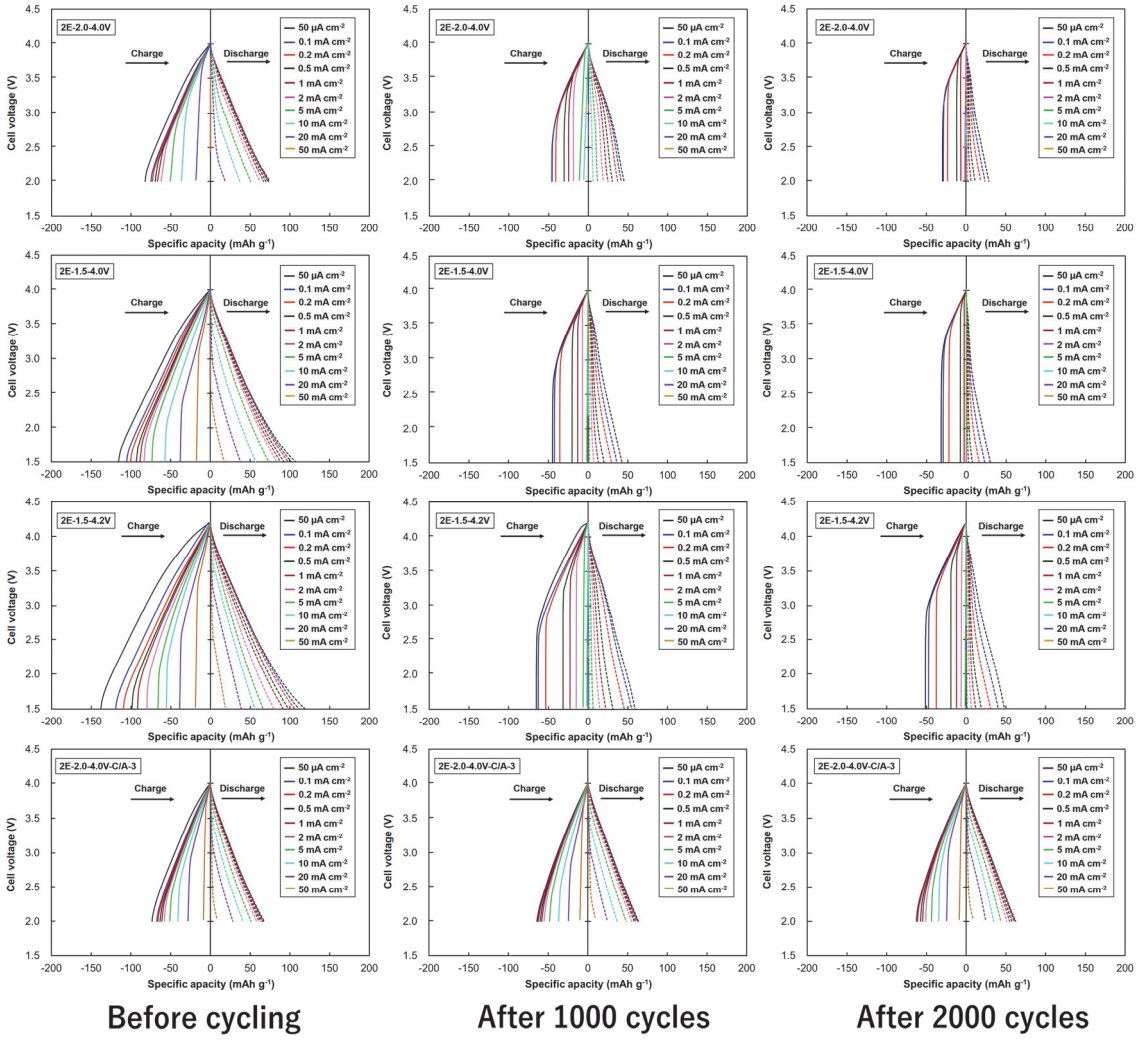

Fig. 4.13. Cell voltage–specific capacity profiles of the 2E full-cells over different cell voltage ranges and at different cathode:anode active mass ratios, plotted during the cycle tests conducted at the current density of 1 mA cm^{-2}.

4.3.4 Postmortem electrode analyses

Postmortem electrode analyses were performed on the representative 2E cell (2E-1.5–4.2V), which was evaluated through the severe cycle test performed over the largest cell voltage range. Composition depth profiles of the pristine electrodes and those aged in 2E-1.5–4.2V were obtained from the wide-scan XP spectra achieved from the topmost thin layer (~5 nm) of the electrodes [28], which were subsequently etched using an ion gun. The etching rate when SiO_2 on Si wafer was employed as the target was 0.2 nm s^{-1}. The composition of the electrode in the depth direction is shown in **Fig. 4.14**. For the pristine cathode, only C and O were detected on the surface, and O disappeared with increasing depth. The C was derived from the AC particles, acetylene black (used as the conductive agent), and the binders (sodium carboxymethyl cellulose and styrene-butadiene rubber). In the shallow layer of the aged cathode, F and Li originating from the $LiPF_6$ electrolyte were detected, although C remained the principal constituent. A low fraction of O was also observed, which decreased with the depth. As the etching time increased, the fractions of F and Li decreased, while that of C increased. At the top layer of the pristine anode, the principal constituents were C, O, and Si, with traces of N. N originated from the polyimide binder. C and O may have been derived from acetylene black or the polyimide binder. The top layer of Si particles was covered with oxide films, providing Si and O elements at the lower etching times. As the etching time increased, the fraction of Si increased significantly, whereas those of the others decreased. Particularly, the fraction of O decreased significantly. The moderate decrease in the fraction of N indicated that the Si particles and acetylene black that were covered with oxide layers and adhering to the polyimide binder were stripped by etching, and pure Si and C were exposed. The aged anode included significant amounts of F and Li (30% by atom). The formation of the SEI on the surface of the anode to prevent the electrolyte from decomposing further was completed within several cycles of Li-ion insertion and extraction [28]. The fractions of F and Li remained high till the etching time of 500 s, and subsequently, those of Si and C started to increase, implying that a thick SEI layer composed of F and Li was deposited on the anode. Since N was not detected, the increase in the fraction of C at etching times in excess of 500 s was attributed to the exposure of acetylene black. A moderate fraction of P was observed in the superficial layers

of the cathode; however, it disappeared at higher etching times.

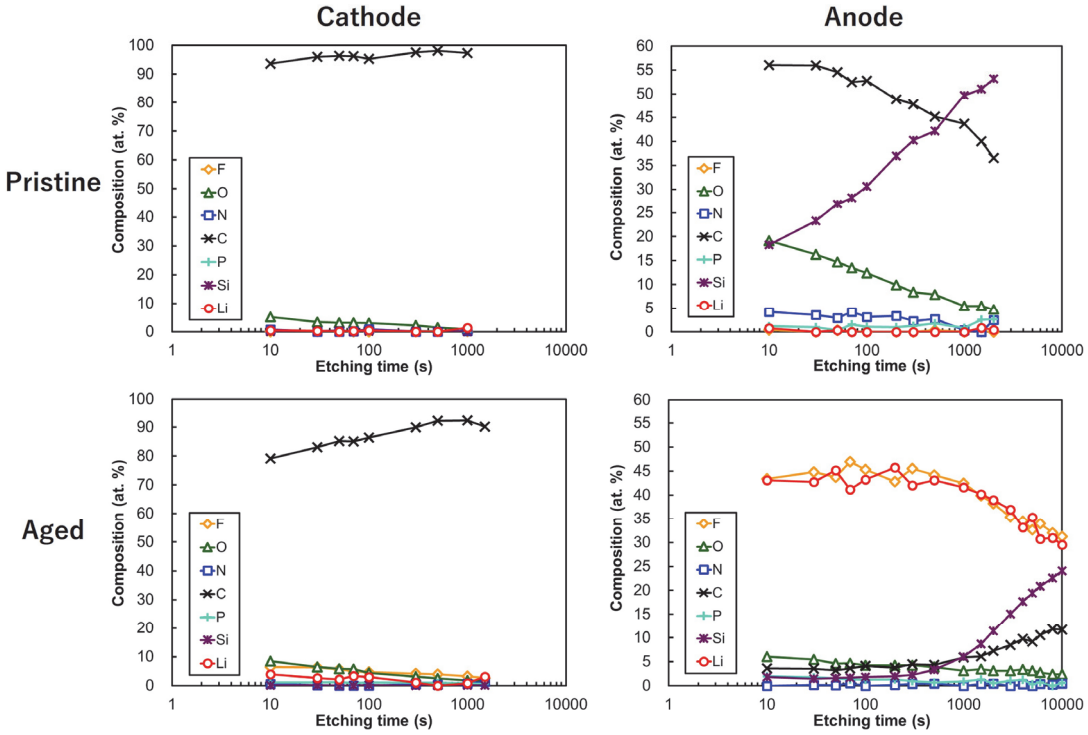

Fig. 4.14. Composition depth profiles of the pristine and aged electrodes of the 2E-1.5–4.2V cell. The etching rate (SiO_2-based) was 0.2 nm s^{-1}.

The narrow-scan XP spectra of the pristine and aged cathodes are shown in **Fig. 4.15**. Small bumps assigned to C–O (533.4 eV) [29] and C=O (531.8 eV) [29] were confirmed on the O 1s spectra and corresponded to 287.7 eV [30] and 286.3 eV [30] in the binding energy of C 1s. The broad peak that appeared in the C 1s spectra was a band derived from C–C (284.4 eV), [31] carbon black (283.8 eV), [32] and C–H (285.0 eV) [30], all of which may have originated from the AC particles, acetylene black, and the binders. The cathode exhibited no significant variations in its narrow-scan spectra due to the charge/discharge cycling in the LIC cells. Only $LiPF_6$-derived bumps were observed on the F 1s and P 2p spectra of the aged cathode at the lower etching times. The identification of $Li_xPO_yF_z$ at 687.5 eV [33] and Li_xPF_y at 686.0 eV [33] on the F 1s spectra, and $LiPO_yF_z$ at 134.2 eV [33] and Li_xPF_y at 135.7 eV [33] on the P 2p spectra indicated the residual deposition of PF_6^- adsorbed onto the surfaces of the AC particles.

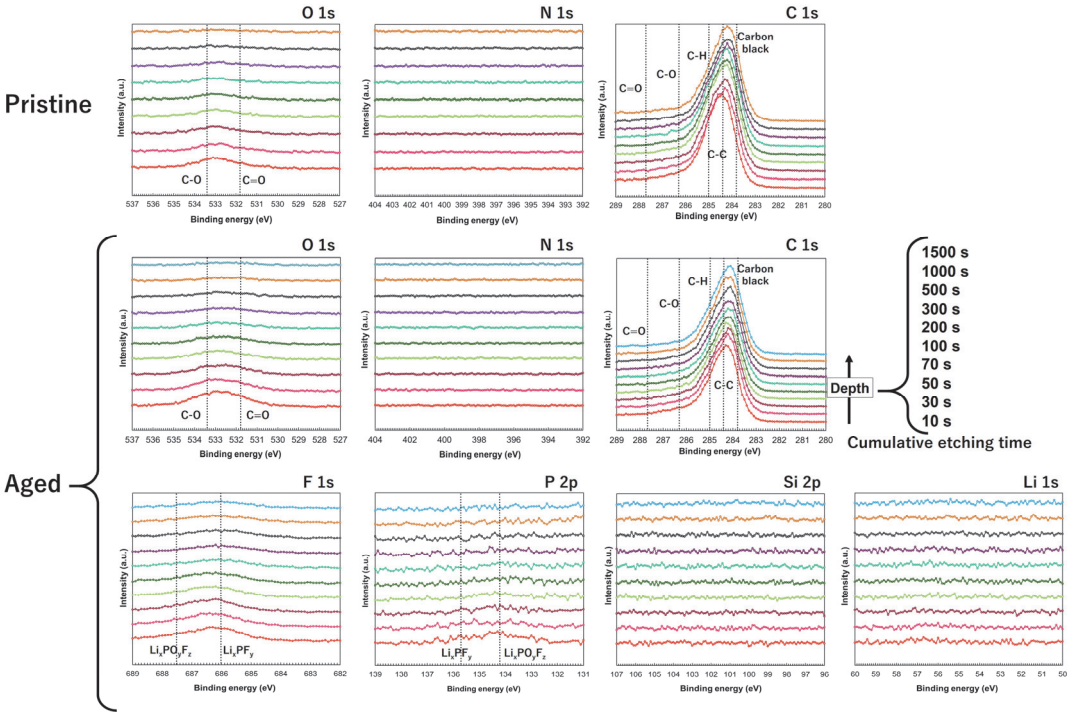

Fig. 4.15. Narrow-scan XP spectral profiles of the pristine and aged AC cathodes of the 2E-1.5–4.2V cell. The etching rate (SiO_2-based) was 0.2 nm s^{-1}.

Figure 4.16 shows the narrow-scan XP spectra of the pristine and aged anodes as a function of the etching time. The raw narrow-scan XP spectra displayed peak shifts owing to the charge-up phenomenon, which was related to the formation of a thick and low-conductivity SEI layer. Therefore, calibrations were made for the spectra of the aged anode based on the C–C bonds, which appeared at 284.4 eV, and the Si–Si bonds which should appear at 99.1 eV [34]. For the pristine anode, a sharp peak that appeared on the Si 2p spectra was assigned to the Si bulk (Si–Si bond at 99.1 eV) [34]. At etching times shorter than 100 s, bumps resulting from SiO_x ($1 < x < 2$) appeared at 101–104 eV [35]. The O 1s spectra exhibited bumps at 532 eV caused by Si–O at the shorter etching times [36]. Weak bumps resulting from imide groups and N-graphite in the polyimide binder were observed in the N 1s spectra at 399.4 eV and 400.1 eV, respectively [37]. For the aged anode, at etching times longer than 200 s, the peak centered at 99 eV broadened to lower binding energy than that in the pristine anode owing to the formation of the Li–Si bond. The Li–Si bond can be commonly identified at 98.0–98.4 eV [38]. The

existence of the Li–Si bond suggested the delamination of Si particles that had accepted Li ions and alloyed with Li. Furthermore, it was demonstrated that Si particles were deposited in the SEI layer, whose thickness was 60 nm (300 s × 0.2 nm s^{-1}). The strong peaks attributed to LiF at 685 eV [39] on the F 1s spectra and 55 eV [39] on the Li 1s spectra indicate that LiF produced by the reduction of $LiPF_6$ was a principal constituent of the SEI layer. The peaks that appeared on the F 1s spectra at etching times longer than 200 s were identified as Si–F (686.6 eV) [40]. Si–F is produced by the reaction between Si and $LiPF_6$ [41]. Si–F peaks on the Si 2p spectra would be masked by the very intense peaks of Si–Si and Si–Li. No significant peaks or bumps were detected on the N 1s spectra, meaning that the polyimide binder was stripped during the cycle test. At the lower etching time, the C 1s spectra exhibited bands attributed to C–H, C–C, and C–Li, whereas the O 1s spectra exhibited bumps attributed to C=O. This indicates that the SEI layer included byproducts produced from the electrolyte solvent (ethylene carbonate/diethyl carbonate). When the SEI layer was removed (etching time > 200 s), broad peaks resulting from C–Li (284.7 eV) [42], acetylene black, and Li_xC (282–283.2 eV) [43] appeared on the C1s spectra, and Li–C was identified from the peaks at 57 eV [42] on the Li 1s spectra, implying that acetylene black accepted Li ions as well [42]. The bumps on the F 1s spectra were identified as covalent C–F (687.4 eV) and semi-ionic CF (685.8 eV), respectively [44]. The bands in the C1s spectra corresponding to covalent C–F and semi-ionic CF appeared in the ranges of 288–291 and 287.0–287.4 eV, respectively [45]. Fluorocarbons can be produced by the reaction of the alkaline carbonate radicals with $LiPF_6$. A bump resulting from $LiPO_yF_z$ and Li_xPF_y on the P 2p spectra at shorter etching times was attributed to the residual deposition of the electrolyte at the anode surface.

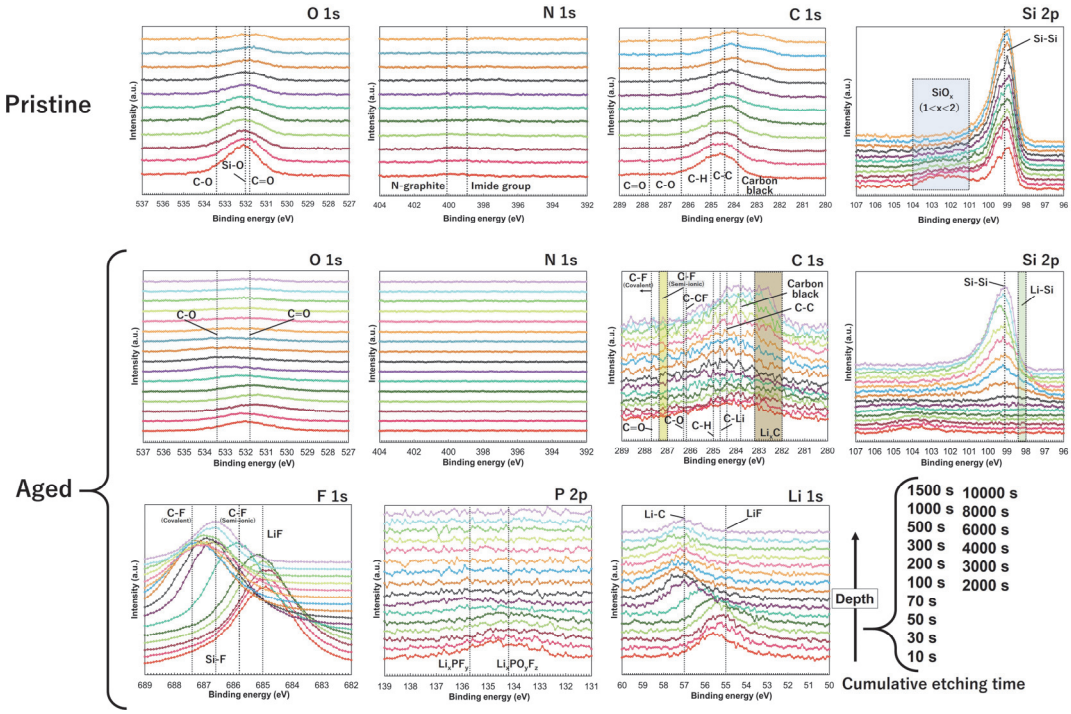

Fig. 4.16. Narrow-scan XP spectral profiles of the pristine and aged Si anodes of the 2E-1.5–4.2V cell. The etching rate (SiO_2-based) was 0.2 nm s^{-1}.

Figure 4.17 shows the superficial and cross-sectional views of the pristine and aged electrodes obtained by SEM. The superficial and cross-sectional morphologies of the aged cathode exhibited no significant variations following the cycle test. No depositions were observed on the AC particles. The Si particles on the aged anode surface were covered with thick SEI deposition (60 nm-SiO_2) mainly composed of inorganic LiF. The SEI film abounded with cracks and was formed unevenly over the entire aged anode. A soft rime-like growth of SEI on the Si particles and the delaminations between the particles and between the current-collector and the particles were confirmed from the cross-sectional view of the aged anode.

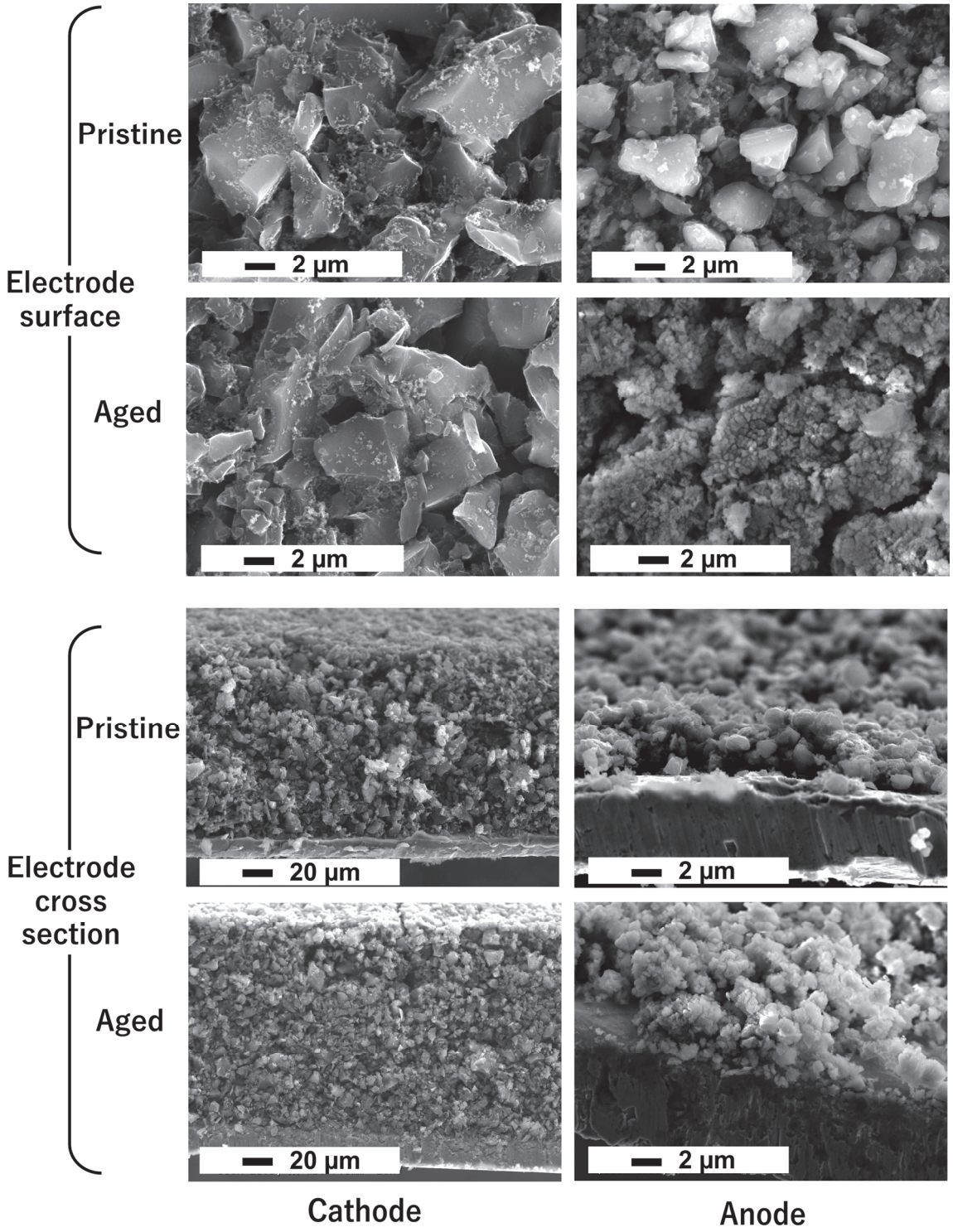

Fig. 4.17. Superficial and cross-sectional SEM images of the pristine and aged electrodes of 2E-1.5–4.2V.

4.3.5 Aging and electrochemical performance of LIC cells using AC cathode and Si anode

The volumetric expansion of Si causes the peeling of the electrode material and exposes newly created surfaces to the electrolytic solution. Therefore, the SEI layer on the Si anodes employed in LIBs repeatedly collapses and reforms during the charge/discharge cycles [4]. In the present study, the SEI layer formed on the LIC anode consumed or exfoliated the organic components derived from the decomposition of the solvent and was mainly constituted of LiF. This was similarly confirmed at the end of the charge/discharge cycling of the LIBs [46]. The aging of the present Si anode causes not only the peeling of Si particles due to volume expansion but also the generation of Li_xSi that did not return to Si even when the cell was fully discharged. Si may bind to F in $LiPF_6$ and LiF to form Si-F, which might be related to the loss of capacity and the hindrance to the diffusion of Li ions into the Si bulk. Therefore, a nearly identical aging phenomenon occurs in the Si anode of LICs as in that of LIBs.

AC exhibiting a specific capacity of 200 mAh g^{-1} (over the potential range of 1.5–4.2 V vs. Li/Li^+) and Si having a Li-ion storage capacity of 2225 mAh g^{-1} (0–1.0 V vs. Li/Li^+) were used as the cathode and anode of the LIC cells, respectively. This contributed to a very high energy density of 400 Wh kg^{-1} by minimizing the unutilized capacity of the anode, although the cycling performance was sacrificed. The energy densities of the past LIC cells published in the literature, as well as their respective cathode and anode active materials, are shown in **Table 4.6**. The maximum energy density of the LIC assembled in the present study is significantly higher than those of LICs reported in the literature, revealing that LICs using highly porous AC cathodes and pure Si anodes represent a promising combination for increasing the energy density. The coke-based AC having a specific surface area exceeding 3000 m^2 g^{-1} that has been used in this work and Si powder having a particle size in the range of a few micrometers can be purchased at reasonable prices. Even though thermosetting polyimide binders require high-temperature curing (> 200 °C), the use of ordinary micrometer-sized Si particles can offer some manufactural and economical merits compared to using specially prepared Si, such as nanosized Si and carbon-capsulated Si.

Table 4.6. Energy densities of the LIC cells reported in the literature, based on the total mass of the cathode and anode active materials.

Active material		Energy density (Wh kg^{-1})	Ref.
Cathode	Anode		
Carbide-derived carbon (S_{BET} = 1460 m^2 g^{-1})	$Li_4Ti_5O_{12}$	30	[51]
AC (RP-20, Kuraray Chemical Corp.)	$Li_4Ti_5O_{12}$/carbon nanofibers	55 at <70 W kg^{-1}	[52]
AC (YP-50F, Kuraray Chemical Corp.)	Hard carbon	74 at <70 W kg^{-1}	[53]
AC (S_{BET} = 1400 m^2 g^{-1})	Petroleum coke-derived soft carbon	100 at 200 W kg^{-1}	[54]
N-doped carbon nanopipes	Partially reduced graphene oxide	262 at 450 W kg^{-1}	[55]
AC (YP-50F, Kuraray Chemical Corp.)	SiO_x/graphite	162 at 250 W kg^{-1}	[56]
AC	Si/SiO_x	123 at <30 W kg^{-1}	[8]
Porous spherical carbon (S_{BET} = 1014 m^2 g^{-1})	Carbon coating B-Si/SiO_2	128 at 1229 W kg^{-1}	[49]
Biomass-derived AC	SiOC	200 at <30 W kg^{-1}	[57]
AC	Si nanowires/ Cu nanowires	210 at 193 W kg^{-1}	[47]
Nitrogen-doped hierarchically porous carbon	Carbon coating capsulated Si	213 at 418 W kg^{-1}	[9]
Biomass-derived AC (S_{BET} = 3011 m^2 g^{-1})	Si/flake graphite/carbon composite	159 at 945 W kg^{-1}	[50]
Biomass-derived AC (S_{BET} = 3250 m^2 g^{-1})	Carbon-coated porous Si	257 at 867 W kg^{-1}	[10]
Coke-based AC (S_{BET} = 3041 m^2 g^{-1})	Si	400 at 32 W kg^{-1}	This study

Increasing the cathode capacity by extending the cell voltage range can decrease the unutilized capacity of the anode, facilitating the maximization of the energy density of LIC cells. The specific capacity of the Si anode is lower than that of Si nanowires/Cu nanowires (2800 mAh g^{-1}) [47] or carbon-capsulated Si-composited anodes (3160 mAh g^{-1}) [9], but the energy density at similar power densities is much higher for the present LIC cells. It is convenient to decrease the unutilized capacity of the anode to enhance the energy density of LIC cells. However, a larger cell voltage range did not necessarily enhance the energy density. In this study, the optimum cell voltage range that maximized the usable discharge plateau region for the anode was 1.0–4.3 V for the cell in which the active mass ratio of AC to Si was 6.37. Finally, we succeeded in fabricating LIC cells having a maximum energy density of 400 Wh kg^{-1} (which is comparable to those of conventional LIB cells) while ensuring high sustainability (200 Wh kg^{-1} at 6 kW kg^{-1}), using commercially available cell systems. LICs using ordinary micrometer-sized Si particles as the anode active materials delivered power densities in excess of 10 kW kg^{-1} at energy densities in excess of 100 Wh kg^{-1}. The time-response of the alloying and dealloying processes of micrometer-sized Si particles with Li ions was shown to be acceptable for the LIC anode applications. However, decreasing the unutilized capacity of the anode beyond a limit accelerated the deterioration of cycling performance. The aging of the anode induced by the morphological changes (deposition of thick passive SEI layer and delamination of Si particles) deteriorated its capacity and accelerated the increase in its internal resistance. The increased internal resistance was responsible for the severe deterioration of rate performance. In order to avoid the aging of the anode, the volume expansion of Si particles should be minimized so as to prevent the propagation of the SEI and the loss of current. There existed a trade-off between the utilized capacity of the anode and the energy density of the LIC cell. In the present study, the active mass ratio and the cell voltage range were reduced to restrict the usable capacity range of the Si anode, thereby maintaining the cycling performance of the present LIC system. Reducing the cell energy density to ~180 Wh kg^{-1} enabled the cell to sustain its cycling performance at power densities exceeding 10 kW kg^{-1} at 100 Wh kg^{-1}. Stabilizing the Si anode against structural decay (e.g., by modifying the binder and electrolyte systems) will be an important task to enhance the cycling performance of high-energy-density

Si-based LICs.

4.4 Conclusion

Commercially available coke-based high-specific-surface-area AC (S_{BET}: 3041 m^2 g^{-1}) and low-cost 2-μm-sized Si particles combined with a polyimide binder were employed as the active materials for the cathode and anode, respectively, in order to fabricate very-high-energy-density LIC cells. A three-electrode LIC cell having an AC:Si mass ratio of 6.37 was assembled using AC and Si having specific capacities of 200 mAh g^{-1} over 1.5−4.2 V and 2225 mAh g^{-1} over 0−1.0 V vs. Li/Li^+, respectively. The unutilized capacity was minimized to maximize the energy density of the cell by optimizing the cell voltage range and increasing the cathode:anode active mass ratio. LICs fabricated using the AC cathodes and Si anodes facilitated the increase in energy density and showed great potential as high-density energy storage devices. An energy density of 400 Wh kg^{-1} was obtained at a power density of 32 W kg^{-1} over the cell voltage range of 1.0–4.3 V. Power densities exceeding 10 kW kg^{-1} were achieved at energy densities of > 100 Wh kg^{-1}. However, only 20.1% of the energy density was retained following 1000 cycles at the power density of ~650 W kg^{-1}. The cycling performance was improved by suppressing the usable capacity of the anode, which was done by reducing the cell voltage range and the mass ratio between the active materials. When a low energy density (~180 Wh kg^{-1}) was accepted, 88.6% of the energy and power densities of > 10 kW kg^{-1} and 100 Wh kg^{-1}, respectively, were retained following 2000 cycles at a high power density of ~1 kW kg^{-1}. The time-response of alloying and dealloying of micrometer-sized pure Si particles with Li ions proved to be sufficient for LIC anode applications. The postmortem electrode analyses indicated that at the anode, the delamination of Si particles and the formation of a thick passive SEI layer (60 nm) constituted mainly of LiF occurred, which were the main causes of the deterioration of cycling performance. To sustainably maintain energy densities (> 300 Wh kg^{-1}) in Si-based LIC cells, the Si anode needs to be structurally stabilized against repetitive Li-ion insertion/extraction.

References

[1] K. Zou, P. Cai, X. Cao, G. Zou, H. Hou, X. Ji, Carbon materials for high-performance lithium-ion capacitor, Curr. Opin. Electrochem. 21 (2020) 31–39.

[2] Y. Ma, H. Chang, M. Zhang, Y. Chen, Graphene-based materials for lithium-ion hybrid supercapacitors, Adv. Mater. 27 (2015) 5296–5308.

[3] F. Dou, L. Shi, G. Chen, D. Zhang, Silicon/carbon composite anode materials for lithium-ion batteries, Electrochem. Energy Rev. 2 (2019) 149–198.

[4] X. Su, Q. Wu, J. Li, X. Xiao, A. Lott, W. Lu, B.W. Sheldon, J. Wu, Silicon-based nanomaterials for lithium-ion batteries: A review, Adv. Energy Mater. 4 (2014) 1300882.

[5] P.C. Chen, J. Xu, H. Chen, C. Zhou, Hybrid silicon-carbon nanostructured composites as superior anodes for lithium ion batteries, Nano Res. 4 (2011) 290–296.

[6] M.T. McDowell, S.W. Lee, W.D. Nix, Y. Cui, Understanding the lithiation of silicon and other alloying anodes for lithium-ion batteries, Adv. Mater. 25 (2013) 4966–4985.

[7] M. Saito, K. Takahashi, K. Ueno, and S. Seki, Electrochemical charge/discharge properties of Li pre-doped Si nanoparticles for use in hybrid capacitor systems, J. Electrochem. Soc. 163 (2016) A3140–A3145.

[8] E. Park, D.J. Chung, M.S. Park, H. Kim, Pre-lithiated carbon-coated Si/SiO_x nanospheres as a negative electrode material for advanced lithium ion capacitors, J. Power Sources 440 (2019) 227094.

[9] R. Shao, J. Niu, F. Zhu, M. Dou, Z. Zhang, F. Wang, A facile and versatile strategy towards high-performance Si anodes for Li-ion capacitors: Concomitant conductive network construction and dual-interfacial engineering, Nano Energy, 63 (2019) 103824.

[10] B. Li, F. Dai, Q. Xiao, L. Yang, J. Shen, C. Zhang, M. Cai, Activated carbon from biomass transfer for high-energy density lithium-ion supercapacitors, Adv. Energy Mater. 6 (2016) 1600802.

[11] N.S. Choi, K.H. Yew, W.U. Choi, S.S. Kim, Enhanced electrochemical properties of a Si-based anode using an electrochemically active polyamide imide binder, J. Power Sources 177 (2008) 590–594.

[12] J.S. Kim, W. Choi, K.Y. Cho, D. Byun, J.C. Lim, J.K. Lee, Effect of polyimide binder on

electrochemical characteristics of surface-modified silicon anode for lithium ion batteries, J. Power Sources 244 (2013) 521–526.

[13] S. Uchida, M. Mihashi, M. Yamagata, M. Ishikawa, Electrochemical properties of non-nano-silicon negative electrodes prepared with a polyimide binder, J. Power Sources 273 (2015) 118–122.

[14] M. Shrestha, I. Amatya, K. Wang, B. Zheng, Z. Gu, Q.H. Fan, Electrophoretic deposition of activated carbon YP-50 with ethyl cellulose binders for supercapacitor electrodes, J. Energy Storage 13 (2017) 206–210.

[15] L. Jin, X. Guo, C. Shen, N. Qin, J. Zheng, Q. Wu, C. Zhang, J.P. Zheng, A universal matching approach for high power-density and high cycling-stability lithium ion capacitor, J. Power Sources 441 (2019) 227211.

[16] G. Huang, Y. Wang, T. Zhang, X. Wu, J. Cai, High-performance hierarchical N-doped porous carbons from hydrothermally carbonized bamboo shoot shells for symmetric supercapacitors, J. Taiwan Inst. Chem. Eng. 96 (2019) 672–680.

[17] D. Kim, J.M. Kim, Y. Jeon, J. Lee, J. Oh, W.H. Antink, D. Kim, Y. Piao, Novel two-step activation of biomass-derived carbon for highlysensitive electrochemical determination of acetaminophen, Sens. Actuators B Chem. 259 (2018) 50–58.

[18] T. Eguchi, D. Tashima, M. Fukuma, S. Kumagai, Activated carbon derived from Japanese distilled liquor waste: Application as the electrode active material of electric double-layer capacitors, J. Clean. Prod. 259 (2020) 120822.

[19] B. Liu, X. Zhou, H. Chen, Y. Liu, H. Li, Promising porous carbons derived from lotus seedpods with outstanding supercapacitance performance, Electrochim. Acta 208 (2016) 55–63.

[20] Y. Gao, L. Li, Y. Jin, Y. Wang, C. Yuan, Y. Wei, G. Chen, J. Ge, H. Lu, Porous carbon made from rice husk as electrode material for electrochemical double layer capacitor, Appl. Energy 153 (2015) 41–47.

[21] T. Eguchi, Y. Kanamoto, M. Tomioka, D. Tashima, S. Kumagai, Effect of ball milling on the electrochemical performance of activated carbon with a very high specific surface area, Batteries 6 (2020) 22.

[22] S. Dsoke, B. Fuchs, E. Gucciardi, M. Wohlfahrt-Mehrens, The importance of the electrode mass ratio in a Li-ion capacitor based on activated carbon and $Li_4Ti_5O_{12}$, J. Power Sources 282 (2015) 385–393.

[23] Z. Shi, J. Zhang, J. Wang, J. Shi, C. Wang, Effect of the capacity design of activated carbon cathode on the electrochemical performance of lithium-ion capacitors, Electrochim. Acta 153 (2015) 476–483.

[24] X. Guo, R. Gong, N. Qin, L. Jin, J. Zheng, Q. Wu, J.P. Zheng, The influence of electrode matching on capacity decaying of hybrid lithium ion capacitor, J. Electroanal. Chem. 845 (2019) 84–91.

[25] T. Otowa, R. Tanibata, M. Itoh, Production and adsorption characteristics of MAXSORB: High-surface-area active carbon, Gas Sep. Purif. 7 (1993) 241–245.

[26] A.V Neimark, Y. Lin, P.I. Ravikovitch, M. Thommes, Quenched solid density functional theory and pore size analysis of micro-mesoporous carbons, Carbon 47 (2009) 1617–1628.

[27] G.Y. Gor, M. Thommes, K.A. Cychosz, A.V. Neimark, Quenched solid density functional theory method for characterization of mesoporous carbons by nitrogen Adsorption, Carbon 50 (2012) 1583–1590.

[28] H. Bryngelsson, M. Stjerndahl, T. Gustafsson, K. Edström, How dynamic is the SEI?, J. Power Sources 174 (2007) 970–975.

[29] S.J. Rezvani, M. Pasqualini, A. Witkowska, R. Gunnella, A. Birrozzi, M. Minicucci, H. Rajantie, M. Copley, F. Nobili, A. Di Cicco, Binder-induced surface structure evolution effects on Li-ion battery performance, Appl. Surf. Sci. 435 (2018) 1029–1036.

[30] A. Rezqita, M. Sauer, A. Foelske, H. Kronberger, A. Trifonova**,** The effect of electrolyte additives on electrochemical performance of silicon/mesoporous carbon (Si/MC) for anode materials for lithium-ion batteries, Electrochim. Acta 247 (2017) 600–609.

[31] H. Hori, M. Shikano, H. Kobayashi, S. Koike, H. Sakaebe, Y. Saito, K. Tatsumi, H. Yoshikawa, E. Ikenaga, Analysis of hard carbon for lithium-ion batteries by hard X-ray photoelectron spectroscopy, J. Power Sources 242 (2013) 844–847.

[32] F. Lindgren, C. Xu, J. Maibach, A.M. Andersson, M. Marcinek, L. Niedzicki, T. Gustafsson, F. Björefors, K. Edström, A hard X-ray photoelectron spectroscopy study on the solid

electrolyte interphase of a lithium 4,5-dicyano-2-(trifluoromethyl)imidazolide based electrolyte for Si-electrodes, J. Power Sources 301 (2016) 105–112.

[33] M. Cheng, W. Tang, Y. Li, K. Zhu, Study on compositions and changes of SEI film of Li_2MnO_3 positive material during the cycles, Catal. Today 274 (2016) 116–122.

[34] U.S. Vogl, S.F. Lux, E.J. Crumlin, Z. Liu, L. Terborg, M. Winter, R. Kostecki, The mechanism of SEI formation on a single crystal Si(100) electrode, J. Electrochem. Soc. 162 (2015) A603–A607.

[35] M.R. Alexander, R.D. Short, F.R. Jones, W. Michaeli, C.J. Blomfield, A study of HMDSO/O_2 plasma deposits using a high-sensitivity and -energy resolution XPS instrument: curve fitting of the Si 2p core level, Appl. Surf. Sci. 137 (1999) 179–183.

[36] S. Yang, Q. Wang, J. Miao, J. Zhang, D. Zhang, Y. Chen, H. Yang, Synthesis of graphene supported Li_2SiO_3 as a high performance anode material for lithium-ion batteries, Appl. Surf. Sci. 444 (2018) 522–529.

[37] P. Chen, W. Huang, H. Liu, Z. Cao, Y. Yu, Y. Liu, Z. Shan, Enhanced cyclability of silicon anode via synergy effect of polyimide binder and conductive polyacrylonitrile, J. Mater. Sci.54 (2019) 8941–8954.

[38] F. Strauß, E. Hüger, P. Heitjans, V. Trouillet, M. Bruns, H. Schmidt, Li–Si thin films for battery applications produced by ion-beam co-sputtering, RSC Adv. 5 (2015) 7192–7195.

[39] D.V. Novikov, E. Yu. Evschik, V.I. Berestenko, T.V. Yaroslavtseva, A.V. Levchenko, M.V. Kuznetsov, N.G. Bukun, O.V. Bushkova, Yu. A. Dobrovolsky, Electrochemical performance and surface chemistry of nanoparticle Si@SiO_2 Li-ion battery anode in $LiPF_6$-based electrolyte, Electrochim. Acta 208 (2016) 109–119.

[40] Y.C. Yen, S.C. Chao, H.C. Wu, N.L. Wu, Study on solid-electrolyte-interphase of Si and C-coated Si electrodes in lithium cells, J. Electrochem. Soc. 156 (2009) A95–A102.

[41] G.M. Veith, L. Baggetto, R.L. Sacci, R.R. Unocic, W.E. Tenhaeff, J.F. Browning, Direct measurement of the chemical reactivity of silicon electrodes with $LiPF_6$-based battery electrolytes, Chem. Commun. 50 (2014) 3081–3084.

[42] S. Oswald, M. Hoffmann, M. Zier, Peak position differences observed during XPS sputter depth profiling of the SEI on lithiated and delithiated carbon-based anode material for Li-

ion batteries, Appl. Surf. Sci. 401 (2017) 408–413.

[43] K.C. Högström, S. Malmgren, M. Hahlin, M. Gorgoi, L. Nyholm, H. Rensmo, K. Edström, The buried carbon/solid electrolyte interphase in Li-ion batteries studied by hard X-ray photoelectron spectroscopy, Electrochim. Acta 138 (2014) 430–436.

[44] C. Struzzi, M. Scardamaglia, A. Hemberg, L. Petaccia, J.F. Colomer, R. Snyders, C. Bittencourt, Plasma fluorination of vertically aligned carbon nanotubes: functionalization and thermal stability, Beilstein J. Nanotechnol. 6 (2015) 2263–2271.

[45] W. Feng, P. Long, Y. Feng, Y. Li, Two-dimensional fluorinated graphene: Synthesis, structures, properties and applications, Adv. Sci. 3 (2016) 1500413.

[46] E. Peled, S. Menkin, Review – SEI: Past, present and future, J. Electrochem. Soc. 164 (2017) A1703–A1719.

[47] C.M. Lai, T.L. Kao, H.Y. Tuan, Si nanowires/Cu nanowires bilayer fabric as a lithium ion capacitor anode with excellent performance, J. Power Sources 379 (2018) 261–269.

[48] C. Lu, X. Wang, X. Zhang, H. Peng, Y. Zhang, G. Wang, Z. Wang, G. Cao, N. Umirov, Z. Bakenov, Effect of graphene nanosheets on electrochemical performance of $Li_4Ti_5O_{12}$ in lithium-ion capacitors, Ceram. Int. 43 (2017) 6554–6562.

[49] R. Yi, S. Chen, J. Song, M.L. Gordin, A. Manivannan, D. Wang, High-performance hybrid supercapacitor enabled by a high-rate Si-based anode, Adv. Funct. Mater. 24 (2014) 7433–7439.

[50] Q. Lu, B. Lu, M. Chen, X. Wang, T. Xing, M. Liu, X. Wang, Porous activated carbon derived from Chinese-chive for high energy hybrid lithium-ion capacitor, J. Power Source 398 (2018) 128–136.

[51] T. Rauhala, J. Leis, T. Kallio, K. Vuorilehto, Lithium-ion capacitors using carbide-derived carbon as the positive electrode – A comparison of cells with graphite and $Li_4Ti_5O_{12}$ as the negative electrode, J. Power Sources 331 (2016) 156–166.

[52] K. Naoi, S. Ishimoto, Y. Isobe, S. Aoyagi, High-rate nano-crystalline $Li_4Ti_5O_{12}$ attached on carbon nano-fibers for hybrid supercapacitors, J. Power Sources 195 (2010) 6250–6254.

[53] X. Sun, X. Zhang, W. Liu, K. Wang, C. Li, Z. Li, Y. Ma, Electrochemical performances and capacity fading behaviors of activated carbon/hard carbon lithium ion capacitor,

Electrochim. Acta 235 (2017) 158–166.

[54] M. Schroeder, M. Winter, S. Passerini, A. Balducci, On the cycling stability of lithium-ion capacitors containing soft carbon as anodic material, J. Power Sources 238 (2013) 388–394.

[55] D.P. Dubal, P. Gomez-Romero, All nanocarbon Li-ion capacitor with high energy and high power density, Mater. Today Energy 8 (2018) 109–117.

[56] C. Li, X. Zhang, K. Wang, X. Sun, Y. Ma, A 29.3 Wh kg^{-1} and 6 kW kg^{-1} pouch-type lithium-ion capacitor based on SiO_x/graphite composite anode, J. Power Sources 414 (2019) 293–301.

[57] M. Halim, G. Liu, R.E.A. Ardhi, C. Hudaya, O. Wijaya, S.H. Lee, A.Y. Kim, J.K. Lee, Pseudocapacitive characteristics of low-carbon silicon oxycarbide for lithium-ion capacitors, ACS Appl. Mater. Interfaces 9 (2017) 20566–20576.

Conclusion

5 Conclusions

EDLCs are superior to other energy storage devices in terms of power density and lifetime. LICs combine the anode of LIBs with the cathode of EDLCs, which are promising energy storage devices. LICs can achieve higher energy density than do EDLCs, although their cycle performance is lower than that of EDLCs. There is a need to increase the energy density of those electrochemical capacitors because it has been one-order lower than that of LIBs. This thesis targets on the enhancement of energy density of electrochemical capacitors using porous carbons, as well as new anodic active material. The conclusions for each chapter are given below.

Chapter 2: The material properties and electrochemical performance of SWAC were investigated to verify its potential use as the electrode active material of EDLCs, in comparison with two types of commercially available benchmark ACs. The precarbonization temperature had a significant influence on not only the development of pores but also the energy and power densities of the SWACs. Among all the samples, the SWAC precarbonized at 700 ℃, with a specific surface area of 2434 $m^2\ g^{-1}$, exhibited the highest gravimetric specific capacitance of 152 F g^{-1} and the highest gravimetric energy density of 44 Wh kg^{-1}. The SWAC precarbonized at 600 ℃ achieved the highest volumetric specific capacitance of 75 F cm^{-3} and a volumetric energy density of 18 Wh L^{-1}, but displayed low power performance. The performance of EDLC electrodes using this distilled liquor-originated biowaste was highly promising.

Chapter 3: The variations in textural properties and particle morphology of the AC during the ball milling were investigated. The electrochemical performance (specific capacitance, rate and cyclic stabilities, and Ragone plot, both from gravimetric and volumetric viewpoints) was also evaluated for the ACs milled with different particle size distributions. A trade-off relation between the pulverization and the porosity maintenance of the AC was observed within the limited milling time. However, prolonged milling led to a degeneration of pores within the AC and a saturation of pulverization degree. The appropriate milling time provided the AC a high volumetric specific capacitance, as well as the greatest maintenance of

both the gravimetric and volumetric specific capacitance. A high volumetric energy density of 6.6 Wh L^{-1} was attained at the high-power density of 1 kW L^{-1}, which was a 35% increment compared with the nonmilled AC. The electrode densification (decreased interparticle gap) and the enhanced ion-transportation within the AC pores, which were attributed to the pulverization, were responsible for those excellent performances. It was also shown that excessive milling could degrade the EDLC performances because of the lowered micro- and meso-porosity and the excessive electrode densification to restrict the ion-transportation within the pores.

Chapter 4: Finally, a very high energy density LIC was developed using commercially available AC having a high surface area of 3041 m^2 g^{-1} and conventional 2 μm-sized Si as the cathode and anode material, respectively, at an AC:Si mass ratio of 6.37. The LIC delivered a maximum energy density of 400 Wh kg^{-1} at a power density of 32 W kg^{-1} and exhibited excellent rate stability (200 Wh kg^{-1} at 6 kW kg^{-1}) over the cell voltage range of 1.0 −4.3 V; these values were based on the total mass of the active materials in the cathode (AC) and anode (Si). However, its low cycling stability induced a 79.9% decrease in its energy density (278 to 56 Wh kg−1) following 1000 cycles at ~650 W kg^{-1}. The potential variations of the cathode and anode were investigated during charge/discharge cycling. Postmortem electrode analyses indicated that the anode permitted the delamination of Si particles and the formation of a thick passive solid electrolyte interphase layer (60 nm) mainly constituted of LiF. Reducing the cell voltage range to 2.0−4.0 V and the mass ratio to 3.30 reduced the energy density to 183 Wh kg^{-1} but improved the sustainability (176 to 156 Wh kg−1, 88.6% retention) and maintained the power density (>10 kW kg−1 at 100 Wh kg−1) following 2000 cycles at ~1 kW kg^{-1}.

This research outcome will not only contribute to the effective use of unused resources, but also encourage the development of ecological energy storage devices. Furthermore, this present study will contribute to the improvement of the performance of energy storage devices, which will provide a wider choice of energy storage devices in the future. As a future prospect, I will clarify the performance degradation mechanism of Si used in the anode of LICs. By improving the binder used in the anode and adjusting the composition of the electrolyte, the durability of the LIC may be improved while maintaining high energy density.

Publication with This Thesis

Papers

[1] T. Eguchi, Y. Kanamoto, M. Tomioka, D. Tashima, S. Kumagai,"Effect of ball milling on the electrochemical performance of activated carbon with a very high specific surface area", Batteries, Vol. 6(2), 22 (16 pages), June, 2020.

[2] T. Eguchi, D. Tashima, M. Fukuma, S. Kumagai, "Activated carbon derived from Japanese distilled liquor waste: Application as the electrode active material of electric double-layer capacitors" Journal of Cleaner Production, Vol. 259, 120822 (11 pages), June, 2020.

[3] T. Eguchi, K. Sawada, M. Tomioka, S. Kumagai, "Energy density maximization of Li-ion capacitor using highly porous activated carbon cathode and micrometer-sized Si anode", Electrochimica Acta, Vol. 392, 139115 (16 pages), October, 2021.

International Conferences

[1] T. Eguchi, D. Tashima, M. Fukuma, S. Kumagai, "Electric double-layer capacitance of Shōchū waste-derived activated carbons in non-aqueous electrolyte", 6th International Conference on Advanced Capacitors (ICAC2019), Shinshu University, Ueda, 2O-12, September, 2019.

[2] T. Eguchi, K. Sawada, M. Tomioka, S. Kumagai, Effect of surface area of activated carbon with positive electrode on rate performance of lithium-ion capacitor using Si negative electrode, 9th International Conference on Materials Engineering for Resources (ICMR2021 AKITA), CP-17, (Online) October, 2021.

Domestic Conferences

[1] 江口卓弥,田島大輔,福間眞澄,熊谷誠治「焼酎粕由来活性炭の有機系電解液中での電気二重層特性」日本素材物性学会令和元年度（第 29 回）年会，日本素材物性学会 (2019.6)

[2] 江口卓弥，田島大輔，福間眞澄，熊谷誠治「Charge-discharge performances of shochu waste-derived activated carbons as the electrodes of electric double-layer capacitors」2019 年度電

気関係学会東北支部連合大会，電気関係学会東北支部連合 (2019.8)

[3] 江口卓弥，田島大輔，福間眞澄，熊谷誠治「予備炭化温度が異なる焼酎粕活性炭電極の電気二重層キャパシタ特性」第 60 回電池討論会 (2019.11)

[4] 江口卓弥，沢田圭一郎，富岡雅弘，熊谷誠治「高比表面積活性炭正極と Si 負極の採用による Li イオンキャパシタの高エネルギー密度化」第 61 回電池討論会，オンライン開催 (2020.11)

[5] 江口卓弥，沢田圭一郎，富岡雅弘，熊谷誠治「Si 系リチウムイオンキャパシタの劣化後の電極状態の分析」日本素材物性学会令和 3 年度（第 31 回）年会，日本素材物性学会 (2021.6)

Acknowledgement

I would like to express my deepest gratitude to Professor Seiji Kumagai for his guidance as my supervisor in conducting this research. Professor Kumagai generously taught me the aspects of being a researcher. I would like to express my sincere gratitude to Professor Katsubumi Tajima, Professor Hitoshi Saito, and Associate Professor Mahmudul Kabir for their advices in completing this thesis.

I would like to express my sincere gratitude to Professor Daisuke Tashima, Fukuoka Institute of Technology, and Professor Masumi Fukuma, National Institute of Technology, Matsue College, for their support of the research in Chapter 2. In Chapur 3, I would like to thank Associate Professor Makoto Yamaguchi for his cooperation with the Raman spectroscopy.

I would like to thank Lecturer Yukihiro Yoshida, Assistant Professor Masahiro Tomioka, Specially-appointed Assistant Professor Yusuke Abe, and Technical Staff Mr. Akihiro Nakajima for their help and support. I would like to express my gratitude to the graduates and students of our laboratory, Mr. Toshiaki Ishikawa, Mr. Keiichiro Sawada, Mr. Yugo Kanamoto, Mr. Koki Horikawa, Mr. Ryoichi Sugawara, and Mr. Yuta Yamakawa, who have been involved in this research.

Lastly, I would like to thank my family and parents for their support over the past 27 years.